Development of Organic Molecules for Aqueous Redox Flow Battery

Development of Organic Molecules for Aqueous Redox Flow Battery

A dissertation presented

by

Liuchuan Tong

to

The Department of Chemistry and Chemical Biology

in partial fulfillment of the requirements

for the degree of

Doctor of Philosophy

in the subject of

Chemistry

Harvard University

Cambridge, Massachusetts

February 2018

Advisor: Professor Roy G. Gordon Liuchuan Tong

Development of Organic Molecules for Aqueous Redox Flow Battery

Abstract

The cost of renewable energy sources such as solar and wind has dropped significantly such that the main barrier for a wider adoption is intermittency. The unsynchronized power supply from renewables and the power demand from human activity limit the reliance on renewables. Energy storage is the key enabler in accelerating the integration of renewables.

Aqueous organic redox flow battery (AORFB) offers a potential cost-effective solution to the energy storage. AORFB works by storing liquid electrolyte outside out the electrochemical conversion stack, decoupling battery power and capacity. Redox-active organic molecules are used as electrolyte in the battery. Properties of organic molecules such as solubility, reduction potential, and stability are tunable through structural modification.

Chapter 2 examines the optical properties of anthraquinone-disulfonic acid (AQDS) flow battery system, and correlates its molecular complexation with electrochemical performance. UV-Vis spectroscopy is demonstrated as a powerful tool to study the quinone

chemistry in redox flow battery systems. By incorporating AQDS complexation, a more accurate modelling of battery voltage is achieved.

In addition, the mechanistic investigation of the degradation of anthraquinone-based flow battery is presented by using 2,6-dihydroxyanthraquinone (DHAQ) in alkaline solution as a model system. Through high-resolution LC-MS, NMR, and synthesis validation, the DHAQ degradation mechanism and the proposed remedy are discussed. This chapter demonstrates that how anthraquinones degrade in alkaline solution during electrochemical cycling, and paves the path for the rational design of next generation redox-active organic molecules.

Chapter 3 introduces 2,5-dihydroxybenzoquinone (DHBQ) as a new candidate negolyte molecule for alkaline redox flow battery. The stability, kinetics, cycling performance, and capacity retention are all characterized. Various synthetic strategies to improve the stability of DHBQ are also discussed. The structural modification demonstrates that organic molecules can be tuned with different functional groups to improve the battery performance.

Chapter 4 explores the idea of using a fused quinone as both the posolyte and negolyte material. The electrochemical behavior of fused quinones will be presented and the degradation mechanism will be discussed. Adsorbed and solid batteries with fused quinone are demonstrated.

Chapter 5 presents the synthesis of volatile, thermally stable, and reactive coinage metal 5,5-bicyclic amidinates for chemical vapor deposition (CVD). X-ray structures of the gold, silver and copper amidinates will be presented together with thermalgravimetric analysis. Metallic films with low to none carbon content are obtained through CVD of the silver and gold amidinates. This chapter demonstrates the development of these CVD precursors and offers the opportunity for synthesizing other stable metal precursors which are previously inaccessible with other ligands.

Table of Contents

Acknowledgement

First and foremost, I would like to thank my Ph.D. advisor Prof. Roy Gordon for taking me as a graduate student and guiding me in research in his lab over the past 4 years. I feel very fortunate to be able to work on such an exciting project at Harvard. I have the freedom to explore new research ideas, and Roy is very encouraging with ups and downs in research. As Roy once said, there is no failed experiment - you only fail if you fail to learn. Roy is also very supportive in my professional development when I attended conferences, participated in internships, and applied for the Harvard Horizons program. I cannot be more thankful to have the opportunity to work with Roy in the past 5 years and obtain my Ph.D. degree under Roy's guidance.

I would also like to thank Prof. Michael Aziz for guiding me in research and providing insights and ideas in electrochemistry and science in general. Mike is like a second advisor to me, and I can always rely on him to discuss about research ideas and progress. I want to especially thank Mike for helping me with my career and professional development.

I would also like to thank Dr. Zhengjing Yang, Dr. Yunlong Ji, and Dr. Yan Jing. Although they joined the Gordon lab in my last year of Ph.D. study, we have built very good professional and personal relationships. I have learned tremendously from each of them in their area of expertise, and it was always a quite enjoyable experience running

experiments side by side with them.

I would also like to thank my undergraduate research advisor Prof. Regan Thomson. It was only after the start of the graduate school did I truly appreciate the training on synthetic chemistry I received in Regan's lab. The rigorous synthetic techniques and characterization that I learned in Regan's lab and the year-long undergraduate lab course Chem-350 proved to be pivotal to the success of my graduate study as I synthesized and characterized new compounds and elucidated degradation mechanisms for flow battery and metal deposition projects.

Past 6 years were not only about research, but also about enjoying the stay at Harvard. I want to especially thank my best buddies Dr. Jun Feng, Dr. Xiabing Lou, and Xian Gong. We shared many similar interests and passions. We have hiked and biked numerous parks and trails around Boston, explored new technological ideas such as 3D printing, cryptocurrency and Arduino, played games such as Red Alert 2, DOTA 2, and PUBG, and started the first Harvard Drone Club at Harvard.

I would like to thank Chi Gao, James Tam, Li Zha, Ge Zhang, Ximei Sun, Xizhu Zhao, Guannan Qu, Yin Chen, Yuxi Qin, Robert Gustafson, Dr. Luke Davis, Dr. Marc-Antoni Goulet and all my friends at Harvard for their support along the Ph.D. time. My time at Harvard is much more memorable with them.

Mostly importantly, I want to thank my fiancée Jing Zhang. We have been together

since year 2013, from the very early time of my Ph.D. study. Jingjing has provided tremendous emotional support and made my Ph.D. time a much more enjoyable and memorable experience. She cheered with me for my achievement and gave me comfort when I had tough days. She encouraged me to explore new career opportunities and step out of my comfort zone. I cannot be more grateful for her company in my life.

I want to thank my mom and dad for their support in the past 10 years of my stay in US. It was a huge decision back in 2007 when I decided to pursue higher education in the US, and they have shown their full support. They pushed me to work when I am slacking, and they provided career and life advices when I need. It is comforting to know that they are always there when I need them, and home is always there.

Ph.D. is a long and tough journey. Even now as I am sitting in the lab writing up this paragraph, I still cannot believe that I will have successfully graduated from Harvard, and be referred as Dr. Tong, a title usually addressed to my father. Reflecting on my 6 years at Harvard, indeed I realize that I have grown tremendously in how to think analytically, how to approach a scientific problem, how to formulate a working hypothesis, how to design the right experiment, and how to use each of the instruments with the correct technique. I can confidently say that I am a much better-trained scientist now than I was when I first started graduate school. In addition to the intellectual advancement, I have become a more mature person, ready to start the next phase of my career and life. I want to thank Harvard

for providing the platform for me to grow in the past 6 years. Finally, I want to thank myself for being resilient through the obstacles in the graduate school, for the accomplishment that I am proud of, and for growing to be a better man of myself.

Liuchuan Tong

May 2018

Chapter 1 Introduction

1.1 Energy production and storage

2015 United Nations Climate Change Conference (COP21) was held in Paris from November 30 to December 12, 2015, where representatives from 196 countries and regions participated and agreed on a global reduction of climate change, summarized in the Paris agreement. Within the framework of United Nations Framework Convention on Climate Change (UNFCCC), Paris agreement focused on the carbon dioxide and other greenhouse gas reduction. One concrete goal was to limit the global warming to less than 2 degrees Celsius as compared to pre-industrial levels. As the two biggest greenhouse gas emission countries, US and China both agreed to take concrete measures and collaborations to limit their domestic greenhouse gas emissions. Like most other countries, electricity generation accounts for most emissions in both countries, resulting from inevitable carbon dioxide generation from burning fossil fuels. A 2015 report (Figure 1.1)[1] from US Energy information Administration (EIA) showed that 80% of electricity in US was generated by fossil fuels, and carbon free renewable energy sources only constitute 10% of all electricity produced in US.

Despite being a small player in energy production, the renewable energy market is developing in a tremendously fast pace. Partially due to a strong solar PV market, renewables accounted for almost two-thirds of net new power capacity installed around the

world in 2016, with almost 165 gigawatts (GW) coming online. This was largely due to the booming solar PV deployment in China and around the world, driven by sharp cost reductions from technological and engineering advancement and policy support. This was for the first time that solar PV additions rose faster than any other fuels, including the net growth in coal.[2]

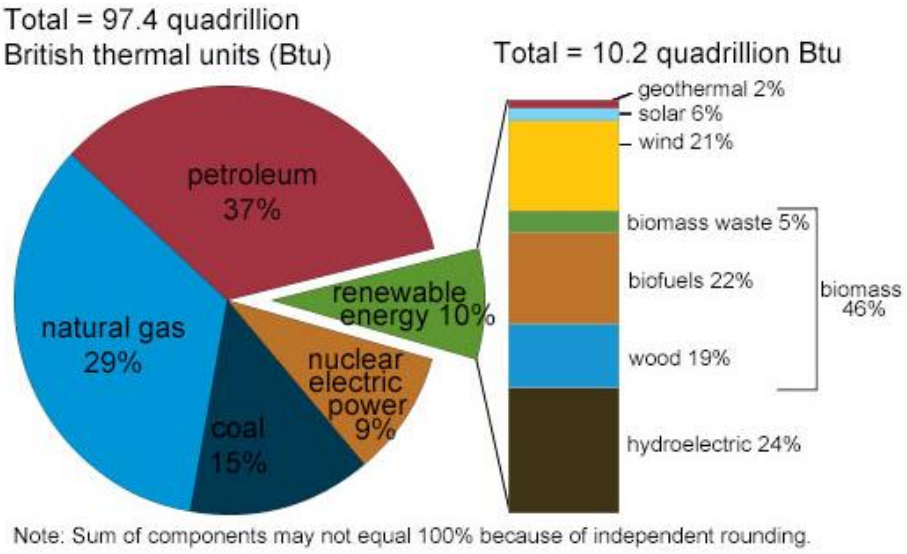

Figure 1.1. Electricity generation by sources (from Ref 1)

With the decreasing cost of solar panels and better design of wind turbans, system integration is becoming increasingly important. It is expected that wind and solar together will represent over 80 % of global renewable capacity growth in the next 5 years. In some developed countries such as Ireland and Germany, the total share of wind and solar will exceed 25 %. Meanwhile in developing countries like China and India, the variable renewable energy share will double to exceed 10 % of total electricity generation.[2] This

increasing heavy reliance on variable renewable energy emphasizes the importance of simultaneous system flexibility upgrade, most importantly including energy storage. According to a recent study by the U.S. National Renewable Energy Lab, widespread grid energy storage is necessary to ensure a stable electric grid powered by 20% or more renewables.[3] Without an effective integrated and flexible electricity grid, the renewables are rapidly losing system value and cost advantages, causing a slower than expected adoption rate.

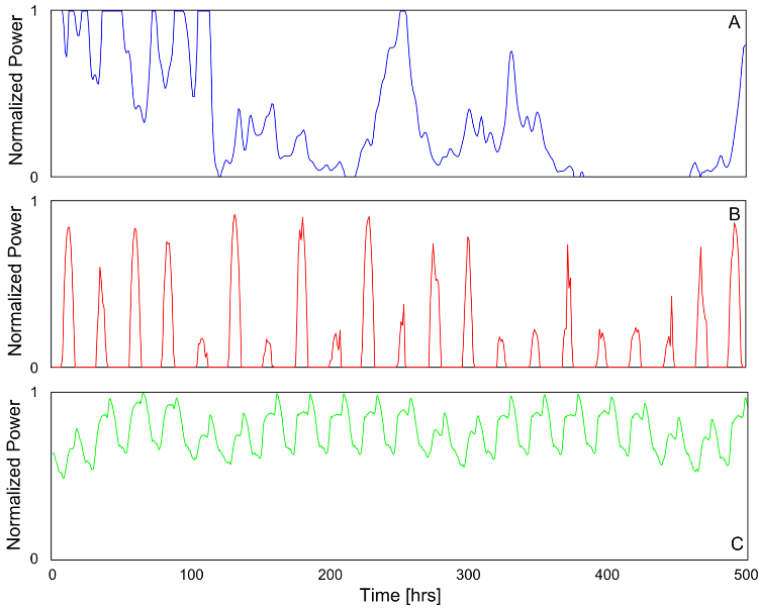

Figure 1.2. Discrepancy in power supply and demand (from Ref 4)

An intermittent energy source, or variable energy source, is usually a renewable energy source that is non-dispatchable due to its fluctuating nature. For example, solar energy is available only in sunny day time, whereas wind energy is available only when there is wind, of which the availability can change even within a day. As humans have little control over

the intermittency of renewable energy, the supply and demand discrepancy causes difficulties in planning and integrating more renewable energy into the electric grid (Figure 1.2).[4] Figure 1.2 showed a three week normalized wind powder in Netherland (Figure 1.2a), normalized solar PV power output in Boston (Figure 1.2b), and normalized electricity demand in UK (Figure 1.2c). It is obvious that these renewable energies were delivered to humans when the Nature chooses to, but not when humans demand. One sarcastic consequence of this unsynchronized supply and demand was reported in an issue of Economist magazine in 2013: The price of whole sale electricity in Germany fell to minus €100 per megawatt hour (MWh).[5] This happened because solar and wind were generating more electricity than needed, and would harm the electricity grid if not consumed. However, since large power plants were designed to run full power and cannot easily reduce production, the electricity price went negative to encourage the consumption of extra electricity in order to maintain a stable grid. Such phenomenon was also observed in some parts of Midwest U.S. at some time when power output exceeds demand. Therefore, this fluctuating market due to intermittent energy generation creates a major barrier for the wider deployment of renewable energy plants.

One important way of equalizing supply and demand is to have some forms of dispatchable balancing capacity, which nowadays is usually in the form of natural gas plants.[6] This creates a paradox as one key reason for integrating more renewable sources is to lower the carbon emission and to have a more sustainable power supply. Deploying natural gas spinning reserve plants as balancing capacity contradicts the idea of reducing

carbon emission.

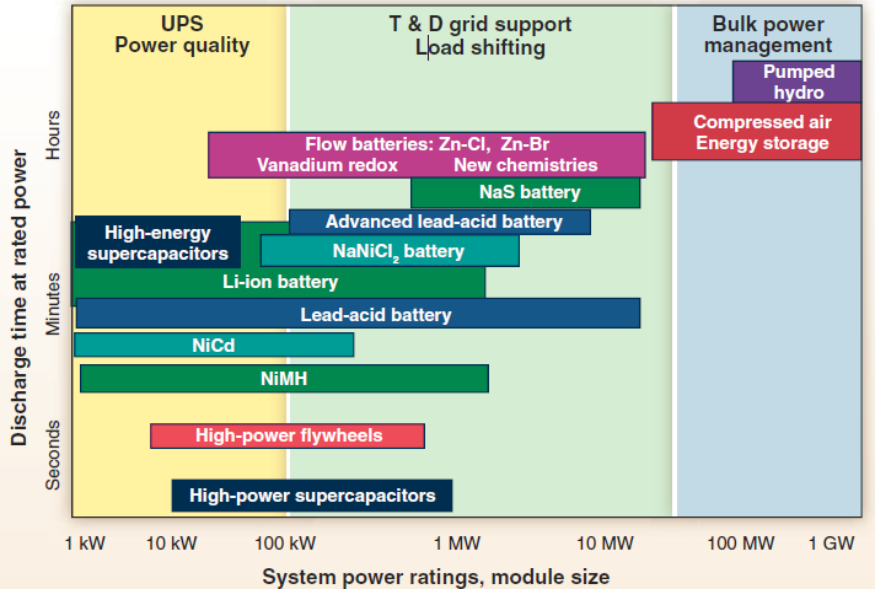

Figure 1.3. Technologies available for energy storage (from Ref 7)

Reliable energy storage system offers a large collection of technologies that can potentially solve the intermittency of renewable energy. Depending on the time-scale and power output of electricity stored, three different types of electricity storage exist, namely Uninterruptable Power Supply (UPS), Grid Support Load Shifting, and Bulk Power Management. Out of all current technologies, pumped hydro stands as the most established and largest-capacity means of storing bulk electricity. Pumped hydroelectric systems account for more than 99% of current worldwide electricity storage capability of 127,000 MW, while compressed air energy storage accounts for only 440 MW in the second place.[7] However, pumped-hydro electricity storage system is unfortunately not suitable as a form of dispatchable balancing power due to its enormous electricity output/input power, high

difficulty and high cost to construct, and too large the charge/discharge time scale to balance the renewable energy intermittency.

As shown in Figure 1.3, electrochemical batteries represent a large collection of technologies available for grid support load shifting. The advantage of electrochemical batteries for electricity storage includes high round-trip energy efficiency, relatively low cost, high dispatchability, and flexible sizes. Several electrochemical battery technologies for grid scale application have been developed over the year as a natural extension of current car or household batteries. However, these solid battery technologies suffer from high unit cost, potential safety concern, and difficult cell to cell management. Due to the nature of solid phase chemical reactions, the storage capacity of an electrochemical cell is limited, and coupled to its power. In order to achieve high energy storage capability, thousands of individual cells need to be assembled together, which inevitably lead to difficult cell-to-cell management. In addition, the high unit cost of solid metal batteries is unreasonable at large scale.

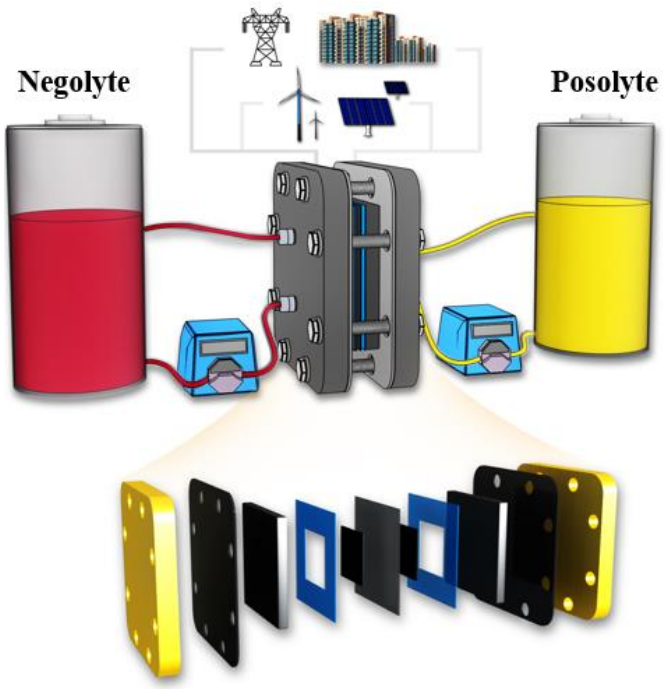

Figure 1.4. Schematics of a redox flow battery

To address the above-mentioned problems by traditional metal based solid batteries, flow battery technology is under active research that represents a very promising way of cheap energy storage for grid support load shifting. Flow battery is a form of rechargeable battery, in which the redox active material was stored in solution form in two different storage tanks (negolyte for negative electrolyte and posolyte for positive electrolyte, Figure 1.4) and separated by an ion selective membrane. In order for all the electrochemically active materials from each storage tank to react with each other, a mechanical pump is needed to circulate the liquid inside the tank for redox active materials to react on the electrode at each side and to exchange ions across the selective membrane. The design of a liquid redox active material bypasses the inherent reaction rate limit of a solid battery,

resulting in essentially unlimited storage capacity which is only determined by the volume of the electrochemically active material. Since the diffusion is an inherent property of liquid, the bulk part of the storage tank will be at the same state of charge, eliminating the need for cell-to-cell management. In other words, a flow battery tank is itself one giant electrochemical cell. In addition, the separation of reaction center (membrane and electrode) and tank means that power of the battery and the capacity of the battery are decoupled. The power of the battery can be scaled proportionally to the area of separating membrane, and by pumping redox active electrolyte into many parallel membranes. The decoupling of power and capacity means that a flow battery can be designed to fit the local supply and demand situation, and can easily be integrated with various photovoltaic and wind turbine systems. The easiness of the setup and the unique advantages encouraged enthusiastic innovations and research in flow battery technology in the past twenty years. The key to the successful development of a flow battery system is to select the right redox active material. Therefore, numerous types of flow battery systems have been studied and reached demonstration level, which include all-vanadium system, iron-chromium system, bromine-polysulfide system, and more. As the most developed flow battery technology, vanadium flow battery has been installed in many places worldwide, and several different MW/MWh scale all-vanadium flow battery systems have been demonstrated for over 10 years in Japan, precisely for the application of soothing renewable energy sources like solar and wind.

1.2 Redox flow battery electrolyte

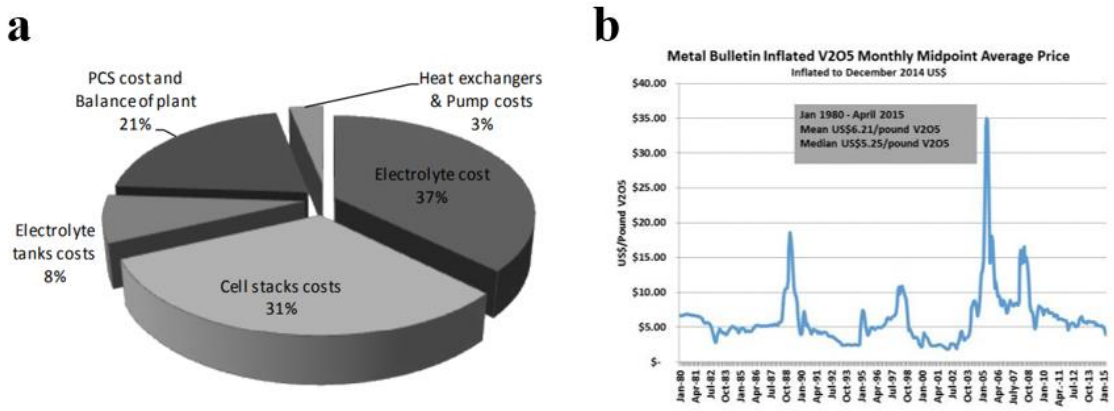

Figure 1.5. a) The capital costs of a vanadium flow battery. **b)** Average cost for V_2O_5 raw material. (from Ref 9, 10)

In order for grid scale energy storage to be widely integrated into the electric grid in a healthy unsubsidized market, the capital cost must be reasonably low such that the deployment of storage is also economically logical. The Department of Energy and Advanced Research Projects Agency-Energy (ARPA-e) has determined an overall capital cost ceiling of $100/kWh for energy storage system for affordability reasons.[8]

Figure 1.5a[9] showed the capital cost of each component in a base case vanadium flow battery. Redox active electrolyte and cell stacks (with membrane) each account for 1/3 of the total capital cost. Therefore, current research has been focused on developing alternative electrolyte material and better and cheaper membranes. Vanadium sets a floor for the cost of all-vanadium redox flow battery, and on average, vanadium costs about

$81.28 /kWh (USGS 2011). Since more than 90% of the vanadium produced was used as alloying agent for iron and steel, the price fluctuates according to ups and downs of steel industry (Figure 1.5b). In addition, demonstrated world resources of vanadium (>63 million tons) are simply not enough to store 2% of world's electricity for 2 days.[10]

The past ten years have seen a burgeoning number of research focus on using aqueous-soluble organic molecules as electrolyte for flow battery applications. The use of organic molecules offers the opportunity of reducing the overall cost in the long-term, since they are low-cost and abundant. More importantly, the properties of organic molecules, such as solubility, reduction potential, and stability can be tuned by modifying their chemical structure. Recent researches have introduced organic molecules with different redox center, high solubility, and wide reduction potential range, and are capable of delivering a flow battery system with comparable capacity and battery voltage, but with much less cost (Table 1.1).

Table 1.1. Overview of reported high performing negolytes for aqueous organic flow battery.

Negative electrolyte	FW (g/mol)	Potential (V vs.SHE)	Solubility (mol/L)	No. of electrons
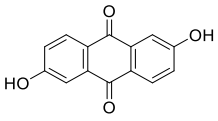 2,6-dihydroxyanthraquinone (DHAQ)[11]	240.2	-0.68 (pH 14)	0.6 M	2

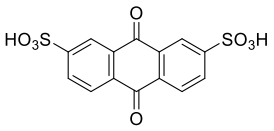 9,10-anthraquinone-2,7-disulphonic acid (AQDS)[12]	368.3	0.22 (pH 0)	1.5 M	2
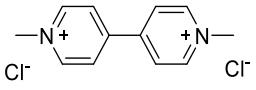 Methyl viologen (MV)[13-14]	257.2	-0.45 (pH 7)	3.0 M	1
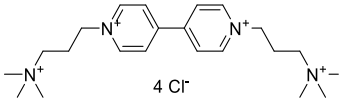 (3-trimethylammonio)propyl viologen tetrachloride (BTMAP-Vi)[15]	500.4	-0.34 (pH 7)	2.0 M	1
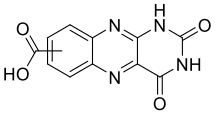 Alloxazine 7/8-carboxylic acid (ACA)[16]	258.2	-0.62 (pH 14)	0.5 M	2
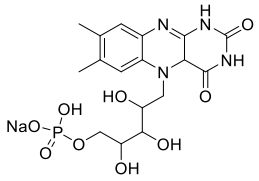 Riboflavin-5'-monophosphate sodium salt (FMN-Na)[17]	480.4	-0.52 (pH 14)	0.24 M	2
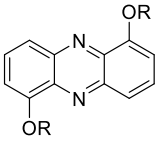 (R is PEGylated TEMPO) Phenazine[18]	785.0	-0.39 (pH 7)	10 mM	2

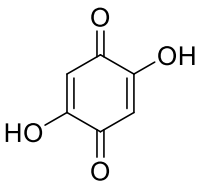 DHBQ[19]	140.1	-0.72	4.31 M	2

1.3 Quinone electrochemistry and design

Among all reported organic molecules for redox flow battery, quinone stands out as the most promising class of molecules that exhibit high cell voltage, high solubility, and high stability.[11-12, 19-20] Quinones are a class of molecules that are ubiquitous in nature. They exist as plastoquinone that is part of the photosystem II,[21] or as Co-Enzyme Q10 that participates in aerobic respiration in mitochondria. They are one of the Nature's choice for electron shuttling. Inspired by the Nature, scientists have been developing quinone based flow battery systems.

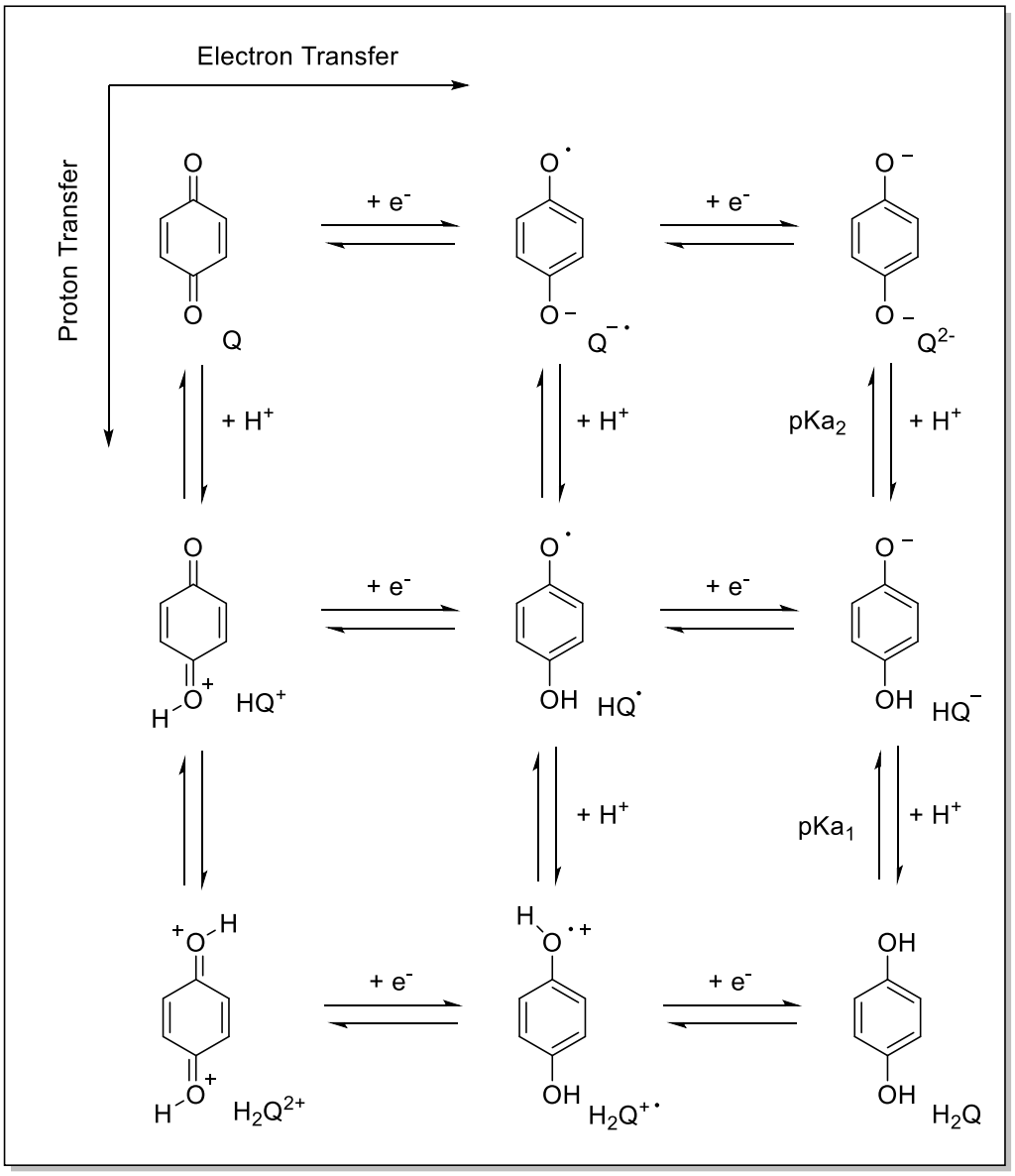

Figure 1.6. Nine-Membered Square Scheme for benzoquinones. Horizontal direction indicates electron transfer (acid/base reaction). Vertical direction indicates electron transfer (redox reaction).

Quinone redox process is usually pH-dependent and characterized in a nine-membered square scheme (Figure 1.6). The reduction of quinone to hydroquinone is a 2-electron process. In aprotic solvents such as MeCN or DMF, the reduction is usually characterized by a two step-wise single electron transfer process $E_1°$ of $Q/Q^{-\bullet}$ and $E_2°$ of $Q^{-\bullet}/Q^{2-}$, the

phenomenon is expected because it is usually harder to add an electron to a species that is already negatively charged. However, in aqueous solution, a concerted single step 2-electron process is usually observed. $E_2°$ in aqueous solution is usually so close to $E_1°$ or even at a more positive potential than $E_1°$, making the overall process a nominally concerted 2-electron process. The reason for this positively shifted $E_2°$ was due to the strong hydrogen bonding from water to the six lone pairs of electrons in Q^{2-} (or protonation in acidic solution). This dramatic hydrogen bonding stabilization and non-specific solvation effect from water bring $E_2°$ to a more positive potential, overlapping with $E_1°$.[22]

In a broad range of pH where proton transfer is involved in the reduction of quinone, a process called proton-coupled electron transfer (PCET), the effect of pH of nominal reduction potential needs to be considered. This is critical because quinones can exhibit dramatically different kinetics and reduction potential in different pH solution, and it is important to choose the right pH for the battery. Fortunately, the effect of pH can be derived from Nernst equation. Consider a quinone reduction reaction:

$$Q + aH^+ + 2e^- \rightarrow H_aQ^{(2-a)-}$$

The Nernst equation for this reaction would be would be:

$$E = E^0 - \frac{RT}{nF} ln \frac{[H_aQ^{(2-a)-}]}{[Q][H^+]^a}$$

At standard condition when $[H_aQ] = [Q]$, use R = 8.314 J/Kmol, F = 96485 C/mol, n = 2 for 2-electron transfer, the above equation is rewritten as:

$$E = E^0 - a * 29.5\, mV * pH$$

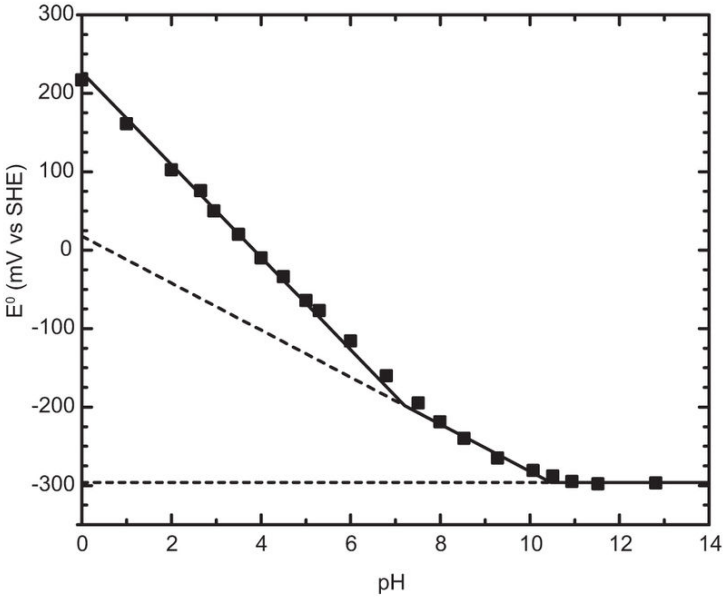

Figure 1.7. Pourbaix diagram of 2,7-anthraquinone-disulfonic acid (from Ref 12).[12]

Such behavior was illustrated in the reduction of 2,7-anthraquinone-disulfonic acid, and was plotted in a Pourbaix diagram (Figure 1.7). The experimental reduction potential obtained were fitted to three solid lines indicating slopes of −59 mV/pH, −30 mV/pH and 0 mV/pH, corresponding to two-, one- and zero-proton process, respectively. The inflection points in the graph correspond to pKa_1 and pKa_2 of hydroanthraquinone. At pH above 11, the reduction of AQDS became pH-independent.

One may take advantage of this pH-dependent reduction potential and design a flow battery system with high voltage. For example, 2,6-dihydroxyanthraquinone (DHAQ) was paired with potassium ferrocyanide to complete a cell with 1.2 V open circuit voltage (OCV) at 50 % state-of-charge.[11] The reduction of posolyte potassium ferrocyanide was pH-independent, meaning that the overall cell voltage was determined by the potential of

DHAQ. Therefore, in addition to solubilizing the quinone, 1 M KOH solution was used such that the DHAQ was at the lowest possible reduction potential.

The three key factors considered when designing a water soluble organic molecule for flow batteries are solubility, reduction potential, and stability. The advantage of using organic molecules as electrolyte offers the opportunity to fine tune each property with a plethora of organic reactions and substituent groups. Apart from some obvious structural red flags, the prediction of molecular stability during cycling is difficult and often revealed only during experimentation. Solubility and reduction potential were much easier to predict and integrated into the initial design of organic molecules.

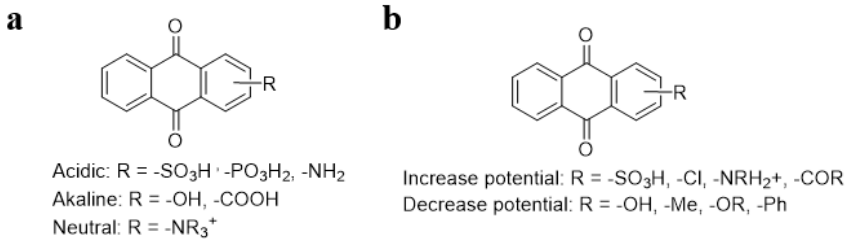

Figure 1.8. **a)** solubilizing groups at different solution. **b)** functional groups that increase or decrease reduction potential

The current strategies for increasing the solubility of organic molecules are to append solubilizing groups onto the molecule. In acidic solution, functional groups such as sulfonate, phosphonate, amine were introduced to increase the hydrophilicity of the overall molecule. In alkaline solution, functional groups that can be deprotonated were chosen, such as hydroxyl and carboxyl groups. In neutral solution, usually organic salts from

ammonium groups were chosen (Figure 1.8a). The solubilizing groups can be directly attached to the quinone core,[11-12] or be attached with some linker groups such as methylene groups.[15] Sometimes it may be advantageous to shift the solubilizing groups away from the redox center such that they do not interfere with reduction potential or induce unwanted reactions.[23]

Figure 1.8b showed some of the functional groups that were added to the quinone core to fine tune the reduction potential. These potential-affecting functional groups are usually attached directly onto the redox center such that their tuning abilities are maximized. Electron withdrawing groups such as sulfonate, halide, ammonium, and ketones lower the HOMO of the molecule, increase the reduction potential of the molecule. On the other side, electron donating groups such as hydroxy, alkyl, alkoxyl groups that increase the HOMO of quinone molecules will decrease the reduction potential. In additional, extending the quinone rings from benzoquinone to naphthoquinone and to anthraquinone gradually lower the reduction potential owning to the delocalization of electrons.

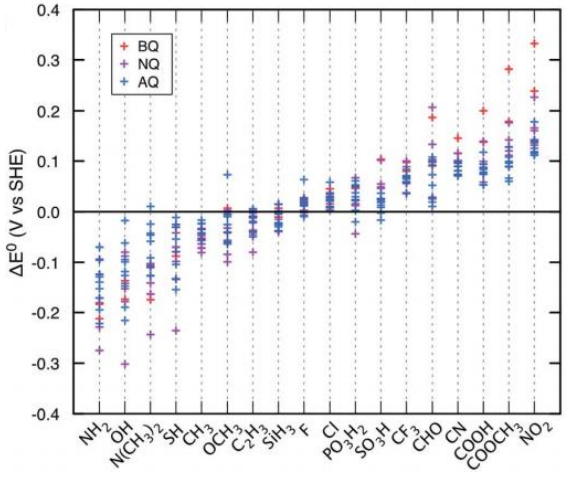

Figure 1.9. Predictied effects of individual R-groups on tuning the reduction potential.[24]

(from Ref 24)

Aspuru-Guzik group has used high-throughput computational screening to simulate the effect of each substituent on the reduction potential of different quinones (Figure 1.9). It was clear from the graph that electron donating groups lower the reduction potential, and electron withdrawing groups increase the reduction potential. Such high-throughput computation screening served as a guidance for designing organic molecules with the expected reduction potential.

A final consideration in designing redox-active organic molecules is its synthetic feasibility. Despite that common stock organic molecules are cheap, and the structures of new molecules are only limited by imagination, one should also take into consideration of how easily the molecules can be synthesized. With the past 100 years of gold age for organic synthesis, scientists often say "given enough manpower and money, synthetic chemists can make any molecules". However, the cost of the organic synthesis quickly builds up through multi-step synthesis and purification. This is especially important when designing molecules that will potentially be produced in tonnes for grid scale energy storage.

The use of organic molecules for grid scale energy storage is still a very new topic, and many of the questions remain to be answered. Chapter 2 examines the optical properties of quinones and their implication in quinone electrochemistry. Degradation mechanisms of the model molecule DHAQ was also studied. Chapter 3 introduces a new molecule

dihydroxybenzoquinone as negolyte for redox flow batteries. Chapter 4 examines the idea of symmetrical quinones, their limits and potential applications.

Chapter 2 Quinone Optical Properties and Degradation Mechanism

Part of this chapter was published as my co-first author paper.[25] Some details that were published were omitted in this chapter.

2.1 Introduction

Quinones are widely involved in many processes involving electron transfer, such as plastoquinone in photosynthesis and coenzyme Q10 in aerobic respiration in mitochondria.[26] Their unique electrochemical properties attract much attention from electrochemists who often study quinones as model systems for spontaneous proton-coupled electron transfer processes.[27] In addition, because of their commercial availability, fast charge-transfer kinetics and the capability of multi-electron transfer in addition to being composed of earth abundant elements, quinones have been the subject of increased attention in the field of electrical energy storage. Quinones in their crystalline or polymeric solid forms find use as reactive electrodes,[28-29] and solvated quinone molecules are employed in aqueous and non-aqueous redox flow batteries.[12, 30-32]

Recent works explore low-cost electrolytes containing redox-active quinone molecules for aqueous flow batteries. Anthraquinones have been rendered highly soluble in acidic and

basic solutions through sulfonation[12] and hydroxylation[11] respectively, and the low redox potentials of certain anthraquinones yield a considerable cell voltage when paired with a high potential redox couple.[11] Quinone-based flow batteries have attracted a great deal of attention for their potential to regulate fluctuations in energy demand and the address the intermittency challenge of renewable wind and photovoltaic supply through cost-effective grid-scale storage.[11-12]

To further improve quinone-based flow battery performance, the behavior of the quinone/hydroquinone redox couple must be understood, especially at the high concentration required for practical operation. Quinone molecules are known to form quinhydrone complexes between the oxidized and the reduced forms.[33-35] This dimer arises from hydrogen bonding between phenolic hydrogen and quinone oxygen , charge-transfer between oxidized quinone and reduced hydroquinone, and from a combination of dispersion interactions between the extended aromatic systems when they coexist in the solution. Such a dimer structure was used in the invention of quinhydrone pH electrodes almost a century ago.[36] This quinhydrone has its own unique optical absorbance signature due to allowed intermolecular electron transfer. The interaction of dissolved monomers results in a change in the electrolyte activity, shifting the reduction potential. When the speciation is greatly driven toward quinhydrone formation, the cell voltage can significantly deviate from that of an ideal solution, in large part due to changes in the unbound monomer species concentrations; this is similar to the behavior of the positive

side of the QBFB where the tribromide complex dominates the speciation.

UV-VIS spectroscopy is a fast and non-invasive technique in quantifying the amount of a certain substance in a solution. It takes advantage of the difference in wavelength of the light that each substance absorbs. By measuring the absorbance spectrum of a solution at different fingerprint wavelength, one can calculate the absolute amount of a substance base on standard curve.

The benzene/anthracene backbone in AQDS absorbed in the UV region of the spectrum and offered the unique opportunity for using UV-VIS spectroscopy to determine the concentration of the reduced and oxidized form of AQDS, therefore determining the real-time state of charge in an AQDS vs. bromine flow battery.

As discussed in Chapter 1, the solubility and reduction potential of quinones can be predicted, but chemical and electrochemical stability of quinones are hard to predict, and often need to be tested experimentally. Organic reactions give scientists tools to make molecules, but also gave nature to break molecules. Numerous side reactions such as nucleophilic substitution, Michael attack, gem-diol formation, radical polymerization have all been reported. This creates a barrier for rationally designing a quinone molecule with exceptional stability suitable for long term grid scale energy storage. The cost considerations are meaningless if the lifetime of the molecules is unknown or there are not good ways to improve the stability. By using the model molecule 2,6-dihydroxybenzoquinone (DHAQ), we studied the degradation mechanism of quinones in

alkaline solution. Through elucidating the degradation mechanism, we would be able to design a molecule with better stability, and effectively cheaper cost in a long run, which may enable massive penetration of intermittent renewable electricity.

2.2 Optical properties of AQDS

Since we are studying the cycling of AQDS, it is of ultimate importance to access both the pure oxidized AQDS and pure reduced $AQDSH_2$, so that we can study their solubility, optical behavior, and other properties individually or at any state of charge (SOC) as needed. However, despite that AQDS can be easily accessed electrochemically in a cycling battery setup, it is very difficult to obtain pure reduced AQDS ($AQDSH_2$) free from water and acid, or to maintain the battery at a certain SOC for a prolonged period because of the inaccuracy in cycling and that $AQDSH_2$ is very sensitive to environmental oxygen. Therefore, chemical reduction was employed to obtain the pure $AQDSH_2$ (Scheme 2.1).

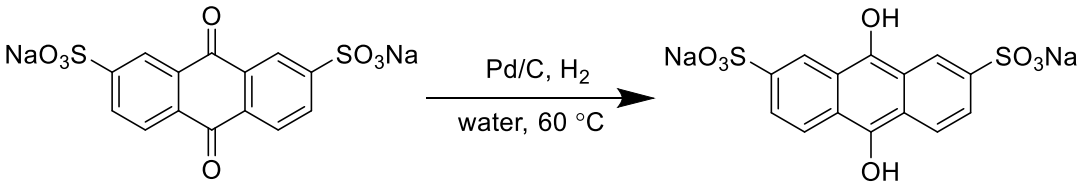

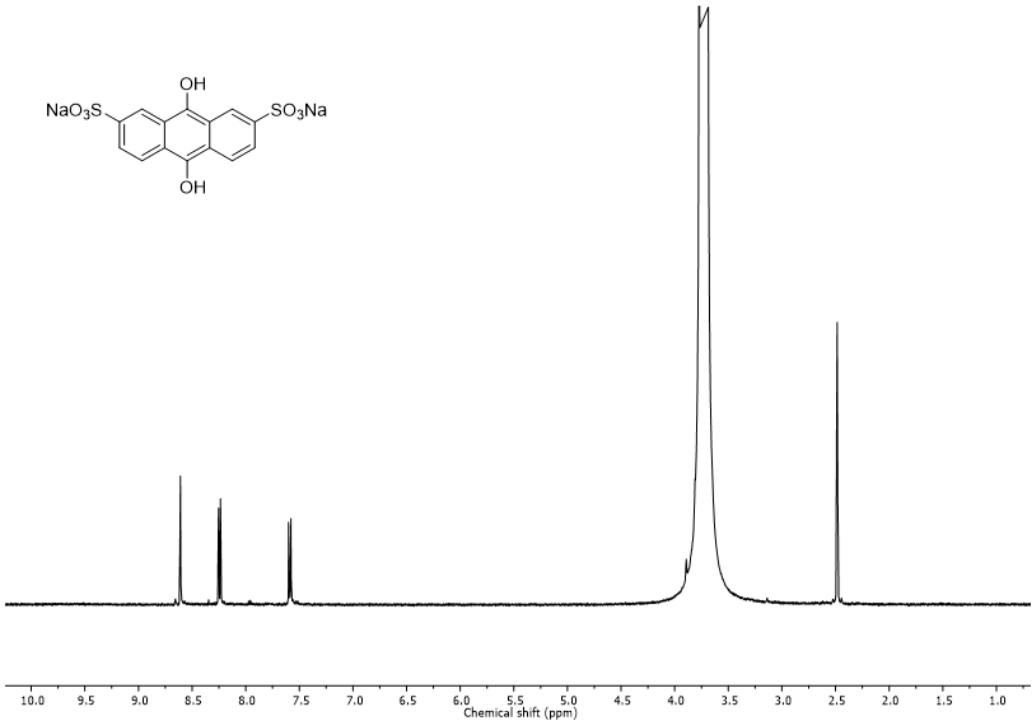

Scheme 2.1. Chemical synthesis of reduced $AQDSH_2$ disodium salt.

To a stirring solution of AQDS disodium salt (5.00 g, 12.1 mmol) in deionized water (10 ml) in Schlenk tube was added Pd/C (10% dispersion, 1.28 g, 0.1 eq). The Schlenk tube was sealed and purged with a flow of hydrogen gas for 30 seconds, and then filled with a balloon of hydrogen gas. The reaction mixture was placed in an oil bath at 60 ºC. After 18 hours, the reaction mixture was filtered under nitrogen using standard Schlenk techniques. The filtrate was evacuated to dryness to afford the reduced form $AQDSH_2$ disodium salt as a brown solid (4.95 g, 11.9 mmol) in 99% yield. ^{1}H NMR (500 MHz, DMSO-d_6) δ: 8.61 (s, 2H, 2 x ArC**H**), 8.23 (d, 2H, J = 8.5 Hz, 2 x ArC**H**), 7.56 (d, 2H, J = 8.5 Hz, 2 x ArC**H**).

In the quinone-bromide flow battery (QBFB), 9,10-anthraquinone-2,7-disulfonic acid (AQDS) is converted to its hydroquinone form in the negative electrolyte (negolyte)

during a battery charging process,

$$\mathrm{AQDS} + 2H^+ + 2e^- \rightarrow H_2\mathrm{AQDS}$$

and the reaction is reversed during discharging. When excessive electrochemically active material (bromide and bromine) is used in the positive electrolyte (posolyte), we define the battery state of charge (SOC) as the state of charge in the negolyte, that is

$$\mathrm{SOC} = \frac{[H_2\mathrm{AQDS}]}{[AQDS] + [H_2\mathrm{AQDS}]} = \frac{[H_2\mathrm{AQDS}]}{[AQDS]_0}$$

where $[\mathrm{AQDS}]_0$ is the starting quinone concentration at the fully discharged state.

The reduced AQDS disodium salt is a brown to pale green powder, and infinitely stable in the absence of air. Immediately after synthesis, one could tell that the reduced $AQDSH_2$ displayed strong fluorescence when dissolved in DMSO, and but most of the fluorescence was quenched when mixed with water (Figure 2.1). In order to quantify the emission and excitation profile, we performed fluorescence spectroscopy. DMSO solutions of different anthraquinone state of charge was prepared by mixing different ratio of $AQDSH_2$ disodium salt and AQDS disodium salt. The solutions were transferred in an oxygen-free glovebox to a 96-well plate, and the plate was subsequently sealed to prevent any oxidation during fluorescent analysis on a Spectramax i3 plate reader.

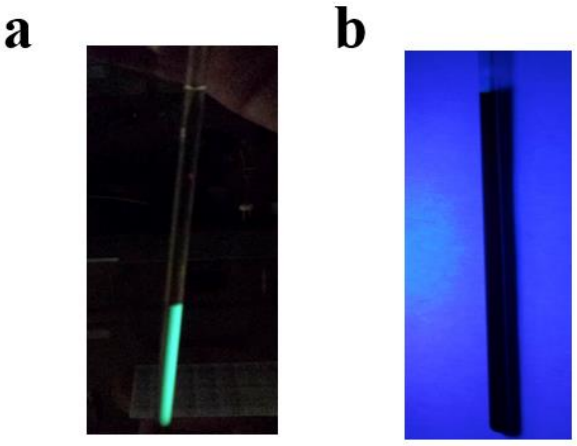

Figure 2.1. (a) $AQDSH_2$ dissolved in DMSO in a NMR tube, top layered with water before mixing. **(b)** After mixing of water and DMSO, fluorescence was quenched.

After scanning for maximum excitation, a 360 nm UV light was selected, and we then subsequently evaluated the emission profile of AQDS with a 360 nm excitation with increasing state of charge. It was clear from Figure 2.2 that fluorescence is the property of the reduced $AQDSH_2$ rather than the property of the quinhydrone complex that is present in mid state-of-charge, as the fluorescence increases with increasing proportion of reduced form. However, the maximum emission wavelength at 510 nm does not seem to follow a simple linear relationship with the state-of-charge, and the emission is present by much weaker when water was used as the solvent.

Nevertheless, the positive correlation of fluorescence to the AQDS state-of-charge offered a great opportunity to directly visualize the changes in flow battery state-of-charge. One may use this property to track the fluid flow property in a flow battery, and study the mass flow in different flow channels and carbon electrodes.[37]

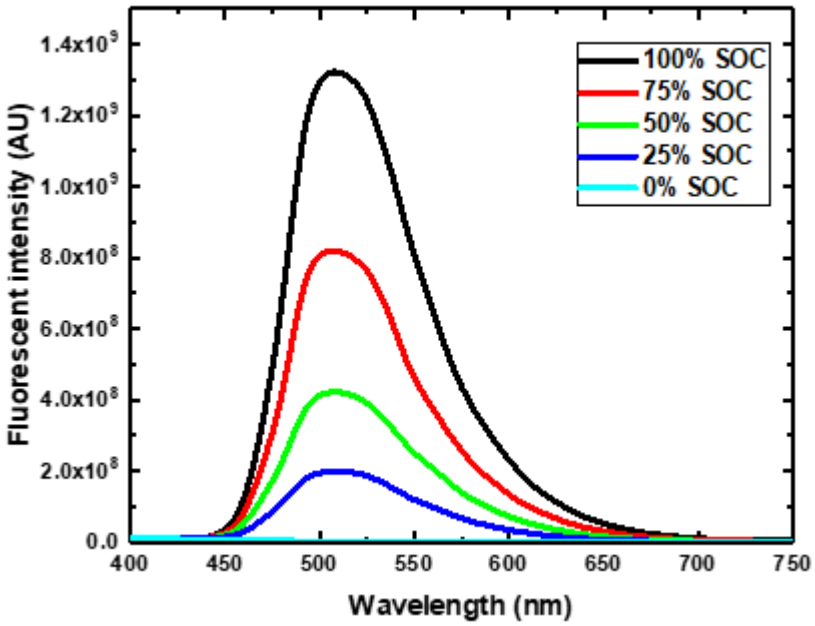

Figure 2.2. Fluorescent spectroscopy of AQDS in DMSO

We then turned to evaluate the UV/VIS properties of AQDS. Oxidized AQDS disodium salt and reduced $AQDSH_2$ disodium salt was each dissolved in 1M sulfuric acid, which has been degassed before to prevent any *in situ* oxidation, both resulting in a clear pale-yellow solution. The spectroscopic assay for pure oxidized AQDS solution, pure reduced $AQDSH_2$ solution, and the mixture of two were conducted at 20 ºC in a 96-well quartz plate at various total concentrations using a PowerWave HT Microplate Spectrophotometer (BioTek) in a nitrogen filled glove box to prevent oxidation during analysis. The absorbance of each well was monitored from 200 nm to 700 nm at the step size of 1 nm. Path length correction with near-red region of water absorption was employed

such that absorbance values were reported for a path length of 1 cm.

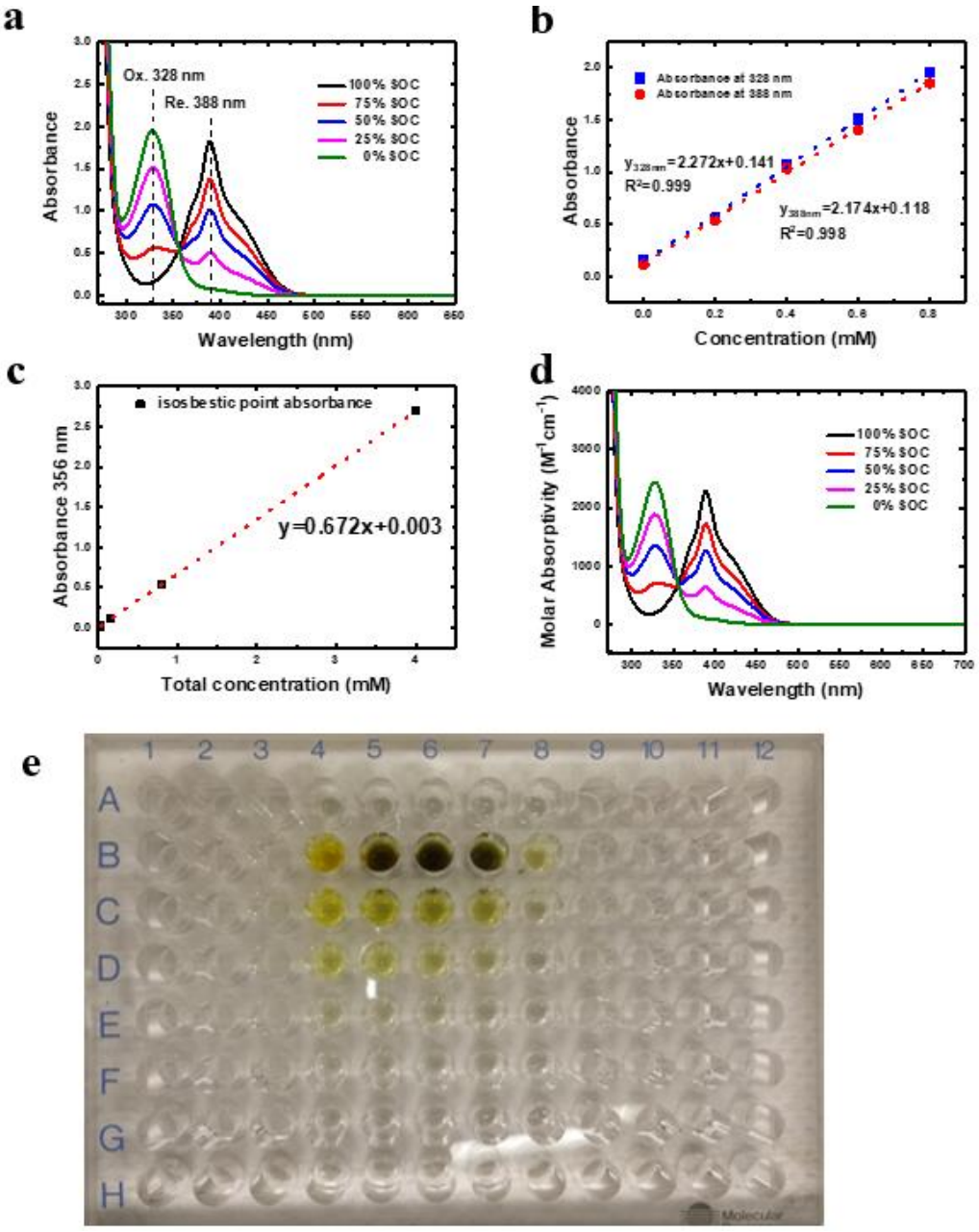

Figure 2.3. UV-VIS Characterization of AQDS. **(a)** UV-VIS measurement of different ratios of AQDS and $AQDSH_2$ at a fix total concentration of 0.8 mM. **(b)** Standard curve derived from (**a)** at five different ratios. (**c)** Isosbestic point calibration for total concentration measurement. **(d)** Figure 2.3(a) plotted in molar absorptivity. **(e)** plate setup: from top to bottom row at a total concentration of 20 mM, 4 mM, 0.8 mM, 0.16 mM; from left to right column at SOC of 100%, 75%, 50%, 25%, 0%.

Figure 2.3a showed the UV-VIS spectrum of AQDS and $AQDSH_2$ in various ratios at a total concentration of 0.8 mM in degassed 1M sulfuric acid. The oxidized form AQDS showed a λ_{max} at 328 nm whereas the reduced form $AQDSH_2$ showed a λ_{max} at 388 nm. Two species do not interfere with each other, as can be seen in Figure 2.3b each species followed a linear response with respect to its concentration. The λ_{max} for both species are separated far enough (60 nm) to ensure an unbiased and accurate measurement of the absorbance for each one. The extinction coefficient for oxidized AQDS at 328 nm was determined to be 2.272 $mM^{-1}cm^{-1}$ at 20 ^{o}C. The extinction coefficient for reduced $AQDSH_2$ at 388 nm was determined to be 2.174 $mM^{-1}cm^{-1}$ at 20 ^{o}C. Base on the standard curve, the real-time state of charge in an AQDS vs. Bromine flow cell could be back calculated. The isosbestic point, the point at which the total absorbance of a sample does not change, at 356 nm (Figure 2.3c) could be used for determining the total concentrations of the organics in negolyte or to monitor any degradation of organics over long term storage and cycling.

2.3 Quinhydrone characterization

It has been known for a long time that quinones can form quinhydrone complex, a dimer arising from π-π stacking, hydrogen-bonding and/or charge-transfer between quinone and hydroquinone.[34-36] In the QBFB, we expect it to impact the performance through changes in viscosity, electrochemical kinetics and other liquid phase or interface

properties. In this work, we'll focus the discussion on its effect on the cell voltage of the QBFB. We will show that by considering the quinhydrone formation as well as the chemical equilibria in the bromide side, full-cell and half-cell voltage predictions using the Nernst equation will be greatly improved when compared to measured values. We will also discuss the deviation of our predictions due to electrolytes' non-ideal solution behavior, and approaches to further elevate the cell potential.

Quinhydrone formation was experimentally observed in AQDS cycling with bromine. Pure reduced or oxidized form of AQDS dissolved in 1 M sulfuric acid are pale yellow-colored. However, during the cycling of a real AQDS vs. bromine flow battery, the negolyte would turn black in mid state-of-charge. This broad absorption of visible range light was attributed to the formation for AQDS-$AQDSH_2$ quinhydrone complex. This phenomenon was also reproduced in a UV-VIS assay. At 20 mM total concentration (Figure 2.4), pure AQDS or pure $AQDSH_2$ showed almost no absorbance in visible region. As AQDS and $AQDSH_2$ were mixed, a broad absorbance over the whole visible region was observed. 1:1 ratio of AQDS and $AQDSH_2$ showed the highest absorbance over the visible region, and 25% and 75% SOC showed similar absorbance level over visible region. This broad absorption over visible region was consistent with literature precedence of quinhydrone absorption, and it was consistent with the observation that the AQDS negolyte will turn dark during cycling.

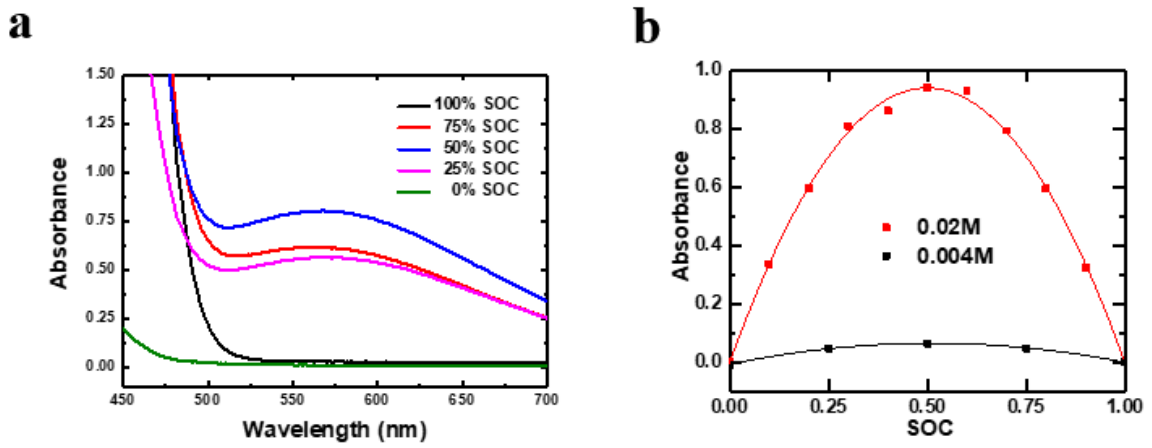

Figure 2.4. (a) UV-VIS Characterization of quinhydrone at 20 mM. **(b)** fittings of quinhydrone over concentration of 20 mM and 4 mM

To understand the impact from quinhydrone formation on the cell voltage, we first need to measure the equilibrium constant of this reaction. In the following discussion, Q, HQ and QHQ will stand for AQDS, H_2AQDS, and their quinhydrone dimer respectively, for conciseness. The equilibrium can be written as

$$\mathrm{Q} + \mathrm{HQ} \rightarrow \mathrm{QHQ},\ K_{\mathrm{QHQ}} \qquad \text{(Equation 1)}$$

$$K_{\mathrm{QHQ}} = \frac{[\mathrm{QHQ}]}{[Q][\mathrm{HQ}]} \qquad \text{(Equation 2)}$$

One distinct property quinhydrone possesses is its strong absorption of visible light, which is absent when only quinone or hydroquinone exists in the solution. As a result, during the QBFB charging process, the initially golden brown negative electrolyte quickly turns dark blue, and later changed back brown color when it reaches 100% SOC (Figure 2.3e). This property can also be used to estimate the concentration of QHQ. Figure 2.4a shows the UV-Vis absorption curve of 0.02 M Q+HQ solution at various SOC. If we zoom in at ~550 nm,

there is a broad peak that reaches its maximum absorption at 50% SOC, indicating its association with QHQ, that is

$$\mathrm{A} = \epsilon[\mathrm{QHQ}]l \qquad \text{(Equation 3)}$$

The absorbance is a function of the SOC and K_{QHQ}, the latter of which can be numerical derived. But at the low $[Q]_0$ concentrations we tested, we can assume the [QHQ] value is much lower than [Q] or [HQ] without impairing the accuracy of the K_{QHQ} calculation. Eqn. 2 can be rewritten as

$$K_{\mathrm{QHQ}} = \frac{[\mathrm{QHQ}]}{([Q]-[\mathrm{QHQ}])([\mathrm{HQ}]-[\mathrm{QHQ}])} = \frac{[\mathrm{QHQ}]}{[Q_0]^2\mathrm{SOC}(1-\mathrm{SOC})-[Q_0][\mathrm{QHQ}]} \qquad \text{(Equation 4)}$$

And the absorbance will be related to K_{QHQ} via

$$\mathrm{A} = \epsilon * l\frac{[Q_0]^2}{[Q_0]+1/K_{\mathrm{QHQ}}}\mathrm{SOC}(1-\mathrm{SOC}) \qquad \text{(Equation 5)}$$

Combining Equations (3), (4) and (5) gives

$$[Q]_0^2 SOC(1-SOC) = \left(\frac{1}{K'_{QHQ}} + [Q]_0\right)\frac{A_{QHQ}(\lambda)}{\epsilon_{QHQ}(\lambda)l} - \left(\frac{A_{QHQ}(\lambda)}{\epsilon_{QHQ}(\lambda)l}\right)^2 \qquad \text{(Equation 6)}$$

From the experimental setup, $[Q]_0$, SOC and l are known and $A_{QHQ}(\lambda)$ is measured. Figure 2.4a shows a representative absorbance vs. SOC curves at a total concentration of 0.02 M. Fitting of the parabola curves obtained at 0.02 M and 0.004 M (Figure 2.4b) yields a K_{QHQ} value about 66 M^{-1}.

It is worth noting that there was a difference between this experimental setup and a real AQDS vs bromide battery setup. Disodium salt of AQDS were used instead of ion exchanged proton form usually used in a real battery for solubility reason. We assumed no optical contribution from sodium ion, and no interaction with quinhydrone formation. By

using 1M sulfuric acid as solvent, we kept the pH the same between the plate reader experiments and real battery setup.

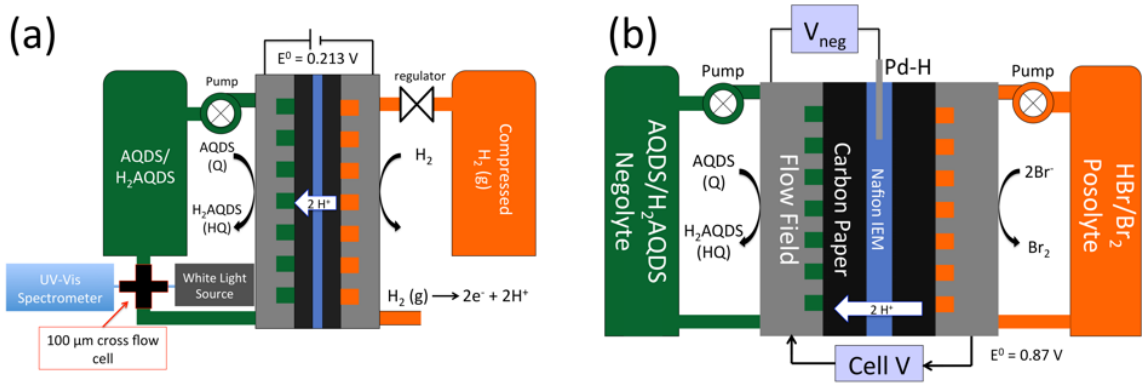

Figure 2.5. (a) in-line UV-Vis spectroscopy configuration for quinone-hydrogen flow cell (QHFC). **(b)** quinone-bromine flow battery (QBFB) with reference Pd-H inserted.

Drew Wong, a graduate student from Michael Aziz lab recreated the UV/VIS measurement using an in-line UV/VIS spectrophotometer with proton-exchanged formed of AQDS (Figure 2.5a). Instead of using bromine as posolyte, hydrogen gas was used to prevent crossover contamination. A 100-µm optical path-length flow cell (Ocean Optics FIA-USP-100) is plumbed to the outlet of the QHFC. A deuterium-tungsten light source (Ocean Optics DH-2000-BAL) is connected to the optical flow cell using 25 cm optical fibers (Ocean Optics QP400-025-SR-BX) with a mirroring optical fiber and UV-VIS spectrophotometer (Ocean Optics Flame-S-UV-VIS). Detailed setup and experimental results can be obtained from our co-authored work and will not be explained in detail in this chapter.[25] Nevertheless, the data obtained from in-line spectroscopy for a real AQDS

vs bromine cell with proton-exchanged AQDS are consistent with the data obtained from plate reader using sodium form of AQDS. The UV spectrum of electrochemically reduced H_2-AQDSH_2 matched that of synthesized Na_2-AQDSH_2 (Figure 2.6), validating the calibration curve constructed in both scenario. The equilibrium constant for quinhydrone formation K_{QHQ} obtained from in-line spectroscopy was 88 M^{-1}, within the error range of the 66 M^{-1} value obtained from plate reader.

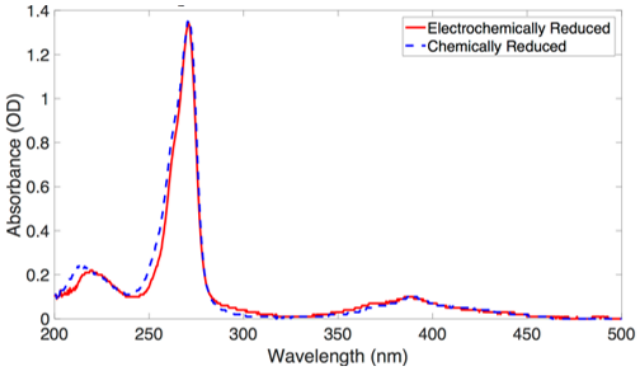

Figure 2.6. absorbance of H_2AQDS (100% SOC) by chemical and electrochemical reduction

To gain further insight into the quinhydrone packing. Dr. Rafa Gómez-Bombarelli conducted theoretical modelling on AQDS-AQDSH_2 interactions. Detailed modelling method, predicted UV-VIS spectrum, absorption energy and discussions can be obtained from our co-authored paper,[25] and will not be discussed in detail in this chapter.

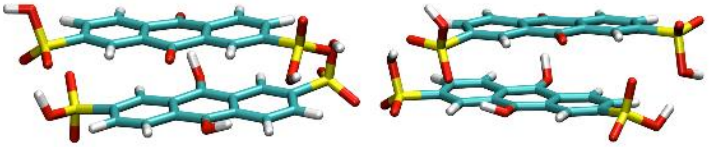

Figure 2.7. Stacked and oblique quinhydrone dimer geometries configurations corresponding to the lowest energy calculations

The modeling results show that quinhydrone dimers converged to two types of arrangements — stacked or oblique, as shown in Figure 2.7. In the stacked dimer, the major axes of the two anthraquinone rings are aligned and the sulfonic acid groups point in opposite directions. In the oblique one, the axes of the two anthraquinone rings form an angle of 25-45 degrees and the sulfonic acid groups point in the same direction and are interlocked. The distances between the centers of mass of AQDS (Q) and H2AQDS (HQ) in the stacked and oblique anhydrous configurations are 3.35 Å and 3.63 Å respectively, which is around twice the van der Waals' radius for carbon (1.7Å). Both anhydrous configurations show significant hydrogen bonding between quinone and hydroquinone, despite the large distance between groups and the unfavorable orientation. There are also appreciable interactions between sulfonic groups and the quinone hydroxyls. In the explicitly-solvated molecules these hydrogen bonds within the dimer tend to be disrupted, but the relative orientations and the stacking distances do not change significantly.

2.4 Quinone electrochemistry

Because the negolyte, posolyte and overall cell voltages (E_{neg}, E_{pos}, and E_{cell} respectively) will change based on the true electrolyte species concentrations, we use electrochemical techniques to corroborate the KQHQ value measured by UV-Vis spectrophotometry. To extract the E_{neg} and E_{pos} experimentally, Dr. Qing Chen installed a reference electrode in the quinone-bromine flow battery (QBFB) to separate the two half-cell voltage contributions from the total cell voltage. The cell configuration for this half-cell experiment is illustrated in Figure 2.5b. A Pd-H reference electrode is sandwiched between two sheets of Nafion membrane, the location of which is justified by prior research.[38] All potentials are reported here vs. SHE based on an average potential of the Pd-H electrode measured before and after the half-cell testing. Under these conditions, the reference electrode potential is ~50 mV vs. RHE.[39] A less than 5 mV potential change is usually observed during the measurement. The build of the quinone-bromide cell follows the published setup.[39]

The quinhydrone complexation can be used to improve the predictive capability of the analytical half- and full-cell potential. Quinone speciation affects its redox potential, which is also the negative terminal potential in the quinone-bromine flow battery (QBFB), through the Nernst equation as

$$E_{neg} = E_Q^0 + \frac{RT}{nF}\ln\left(\frac{a_Q a_{H^+}^2}{a_{HQ}}\right) = E_Q^{0\prime} + \frac{RT}{nF}\ln\left(\frac{[Q][H_{neg}^+]^2}{[HQ]}\right) \qquad \text{(Equation 7)}$$

$$E_Q^{0\prime} = E_Q^0 + \frac{RT}{nF}\ln\left(\frac{\gamma_Q \gamma_{H^+}^2}{\gamma_{HQ}}\right) \quad \text{(Equation 8)}$$

where E_Q^0 is the standard potential (0.213 V vs. SHE) and $E_Q^{0'}$ is the formal potential of the Q/HQ redox couple, a_i and γ_i are the activities and molar activity coefficients respectively of each species and are functions of the species concentrations (e.g. [Q]). The formal potential, defined by the measured negative half-cell potential when [Q] = [HQ], is 0.219 ± 0.016 V and is closely approximated by the quinone standard potential. This results in $\gamma' = \gamma_{QHQ}/\gamma_Q\gamma_{HQ} \sim 1$, leading to the approximation $K'_{QHQ} = K_{QHQ}$, where K'_{QHQ} is the activity coefficient corrected equilibrium constant. [Q] and [HQ] can be numerically derived from Equations (6), (7), and (8) with K_{QHQ} = 80 M^{-1} from the analysis of the UV-Vis spectrophotometry measurements. A plot of the concentration vs. SOC of each of these three species at $[Q]_0$ = 0.2 M is shown in Figure 2.8a.

The measured E_{neg} vs. SOC at $[Q]_0$ =0.2 M is plotted as black dots in Figure 2.8b. Calculated E_{neg} values based on Equation 11 are plotted as solid lines. The blue curve in Figure 2.8b assumes no quinhydrone formation and shows a steep voltage ascent or descent close to 0% and 100% SOC but little voltage variation in the remaining SOC region. This contrasts sharply with the measured result. The orange line instead uses the [Q] and [HQ] values shown in Figure 2.8a applied to Equation 7. The greatly improved agreement between the measured E_{neg}, the orange line indicates that the Q/HQ redox potential is significantly influenced by the formation of QHQ.

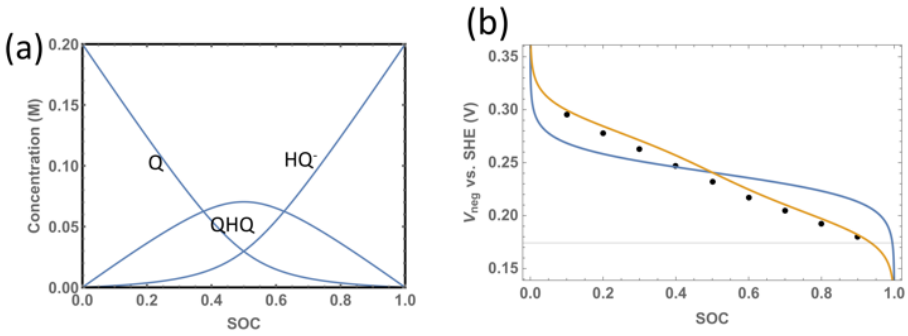

Figure 2.8. (a) Q, HQ and QHQ concentrations with 0.2 M $[Q]_0$ vs. SOC. **(b)** Half-cell voltage vs. SOC. Black dots are experimental data measured in the AQDS-Bromide cell, Figure 2.5b, orange and blue lines are the calculated values of E_{neg} with and without considering QHQ formation with KQHQ=80 M^{-1}, respectively.

Similarly, bromine/bromide/tribromide equilibrium also played an important role in the overall cell voltage. Dr. Qing Chen assembled cell according to setup Figure 2.5b, and we observed that by incorporating both negolyte quinone complexation and posolyte complexation, a much-improved modeling of cell potential is achieved. Detailed modelling work can be accessed in our co-authored publication.[25]

2.5 DHAQ decomposition study

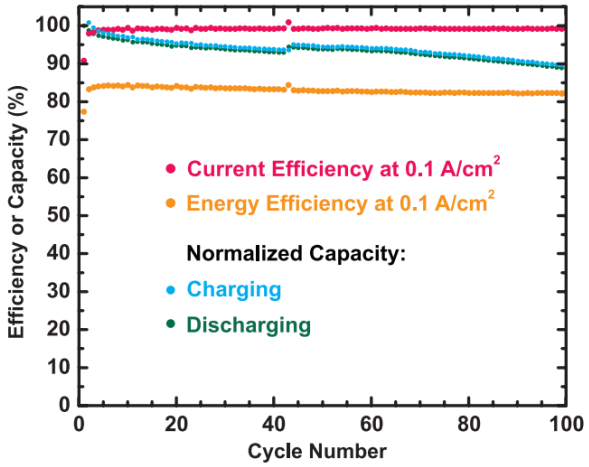

Figure 2.9. Capacity retention, current efficiency, and energy efficiency values of 100 cycles of DHAQ vs potassium ferrocyanide cell

Based on the reported DHAQ cycling data[16], a 0.1% capacity loss/cycle was observed. When cycling at 0.1 A/cm^2 for a 4 mL 0.5 M DHAQ cell with 5 cm^2 electrode, each charge/discharge time cycle takes around 30 minutes to complete. This translates to a temporal degradation of around 5 % loss per day. If a linear degradation rate was observed, the battery would be completely dead after 20 days. This presented a serious problem for using DHAQ as the molecule for long term energy storage. Unlike metals such as vanadium and iron that are electrochemically active but chemically inactive, there are numerous possibilities for DHAQ to decompose. Therefore, it is critically important to elucidate the degradation mechanism of DHAQ so that we could rationally design the next generation

redox-active organic molecules.

In order to rapidly study the molecular stability, Dr. Marc-Antoni Goulet developed a symmetric cell setup to evaluate the stability of an organic molecule. Instead of cycling DHAQ vs ferrocyanide, a 50 % SOC DHAQ was cycled against another 50 % SOC DHAQ. This setup allows us to focus on the degradation of the organic molecule during cycling and to prevent any capacity loss due to cross-over through the membrane. Any capacity loss observed in this setup is the true capacity loss of the molecule. The symmetric cell was cycled between -200 mV and +200 mV, and achieved similar degradation rate as the full cell cycling, validating the setup to study the stability of organic molecules.

After several days of symmetric cell cycling, high-resolution LC-MS analysis of DHAQ decomposition was performed in the Small Molecule Mass Spectrometry Facility on a Bruker Impact II q-TOF with internal calibration sodium formate clusters. Liquid chromatography was performed on an Agilent 1290 Infinity HPLC using a Allure PFPP column (5 um particle size, 150 x 2.1 mm) at a flow rate of 0.4 mL/min and the following elution conditions were applied: 100% solvent A for 2 min, a gradient increasing from 0% to 15% solvent B in solvent A over 13 min, a gradient increasing to 100% solvent B over 5 min, a gradient decreasing to 0% solvent B in solvent A over 0.1 min, and 100% solvent A for 4.9 min (solvent A = 0.1% v/v formic acid in water; solvent B = 0.1% v/v formic acid in acetonitrile). The ESI mass spectra were recorded in negative ionization mode.

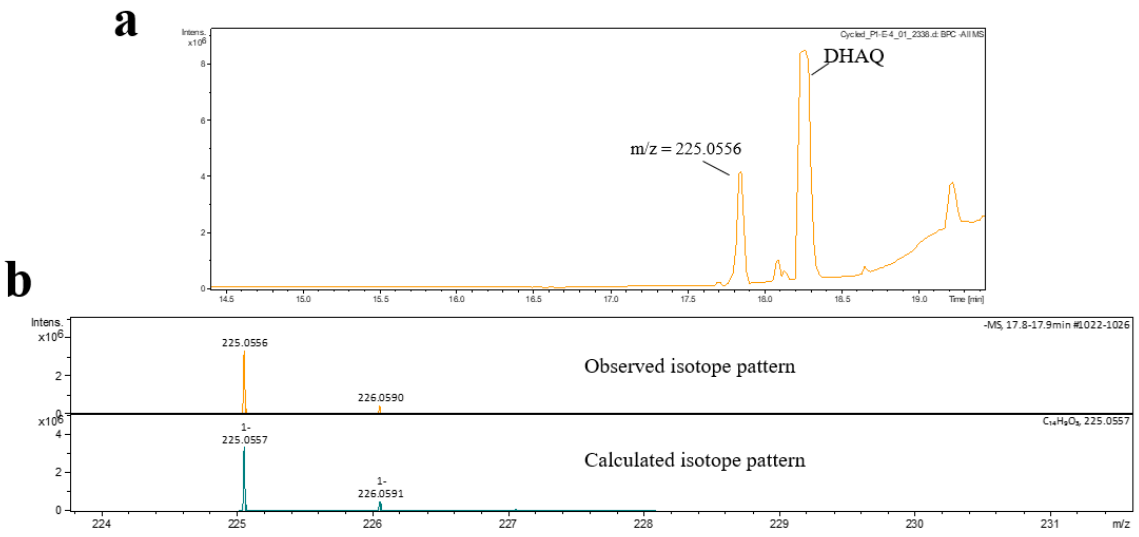

Figure 2.10. a) LC-MS chromatograph of the decomposed DHAQ. A mass to charge ratio of 225.0556 at 17.9 min was observed. **b**) Observed isotopic pattern matched calculated isotope pattern for $C_{14}H_{10}O_3$

LC-MS chromatograph of the decomposed DHAQ from symmetric cell after several days of cycling was shown in Figure 2.10a. The largest peak at 18.3 min was DHAQ starting material peak as confirmed by running a pure DHAQ sample that retained on the column at the exact same time. The second largest peak, which did not exist in the pure DHAQ sample, eluted at 17.9 min was observed. This molecule was presumably less hydrophilic than DHAQ as reverse phase LC column was used. The peak had an accurate mass to charge ratio of 225.0556, which matched a molecular formula of $[C_{14}H_{10}O_3 - H]^-$ with an error of less than 1.5 ppm. The observed isotope pattern of the peak matched the calculated isotope pattern for $C_{14}H_{10}O_3$, further confirming the molecular formula. A molecular formula of $C_{14}H_{10}O_3$ is one oxygen atom fewer, but two hydrogen atoms more

than the DHAQ formula $C_{14}H_8O_4$. Assuming the benzene ring stayed stable during cycling, the only reasonable structure for this molecular formula is 2,6-dihydroxyanthrone. Indeed it has been reported in literature that anthrone can be generated from electrochemical[40-41] and chemical reduction[42] of anthraquinone in acidic solutions.

In order to confirming the molecular structure of proposed anthrone and study its properties in alkaline solution during electrochemical cycling, chemical synthesis of 2,6-dihydroxyanthrone was performed.

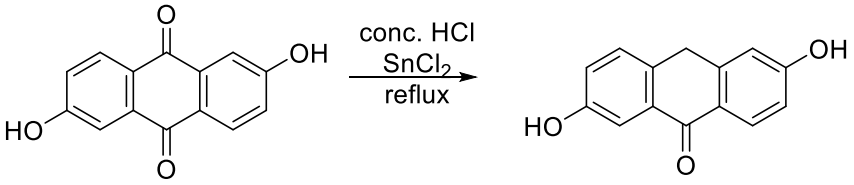

Scheme 2.2. Chemical synthesis of 2,6-anthrone.

To a 50 mL solution of the HCl (37 %) in a 200 mL round bottom flask were added 2,6-dihydroxyanthraquinone (0.8 g, 3.3 mmol), and anhydrous $SnCl_2$ (10 g, 52.7 mmol). The reaction mixture was stirred and reflux in dark. After 8 hours, the reaction mixture was cooled down and filtered. The solid was washed with hot water (3 x 20 mL) and dried to afford pale yellow solid (0.7 g, 93 % yield). **^{1}H NMR** (600 MHz, DMSO-d_6) δ 10.41 (s, 1H), 6.69 (s, 1H), 8.03 (d, 1H), 7.51 (d, 1H), 7.35 (d, 1H), 7.06 (dd, 1H), 6.87 (m, 2H), 4.22 (s, 2H); HRMS (ESI) m/z: calcd for $C_{14}H_9O_3$ $[M-H]^-$, 225.0552; found, 225.0556

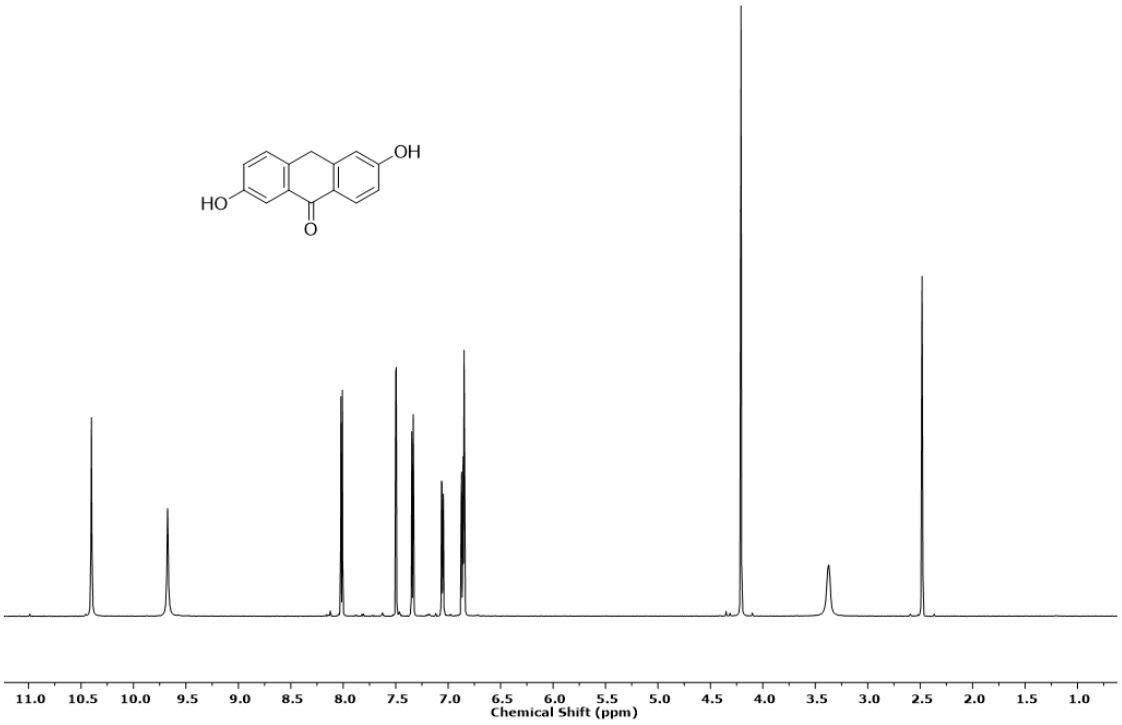

The 2,6-dihydroxyanthrone existed in its anthrone form rather than in its isomer anthrol form in DMSO. To confirm that 2,6-anthrone was the correct structure for the DHAQ degradation product, LC-MS method was re-optimized. The following elution conditions were applied: 100% solvent A for 2 min, a gradient increasing from 0% to 60% solvent B in solvent A over 13 min, a gradient increasing to 100% solvent B over 5 min, a gradient decreasing to 0% solvent B in solvent A over 0.1 min, and 100% solvent A for 4.9 min (solvent A = 0.1% v/v formic acid in water; solvent B = 0.1% v/v formic acid in acetonitrile).

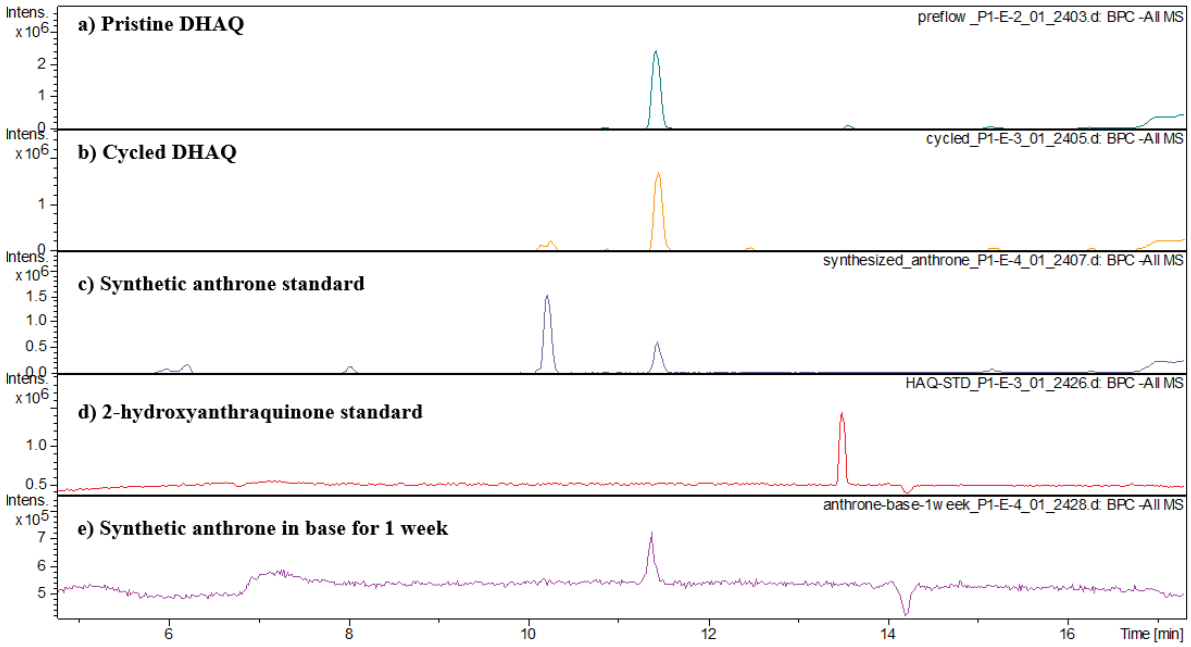

Figure 2.11. LC-MS chromatograph of **a)** pristine DHAQ. **b)** cycled DHAQ. **c)** synthetic anthrone standard. **d)** 2-hydroxyanthraquinone standard. **e)** synthetic anthrone standard sitting in 1 M KOH for 1 week

DHAQ starting material (Figure 2.11a), cycled DHAQ from symmetric cell setup after several days of cycling (Figure 2.11b), and synthetic anthrone (Figure 2.11c) were run in sequence in LC-MS. The synthetic anthrone standard had the same retention time as the degradation peak from cycled DHAQ, further confirming the decomposition product to be 2,6-anthrone.

It was surprising that despite that the synthetic anthrone was pure by NMR in DMSO, DHAQ was detected in LC-MS (Figure 2.11c confirmed by retention time and m/z), of which the sample was prepared in alkaline solution. We then conducted a NMR study on anthrone in base.

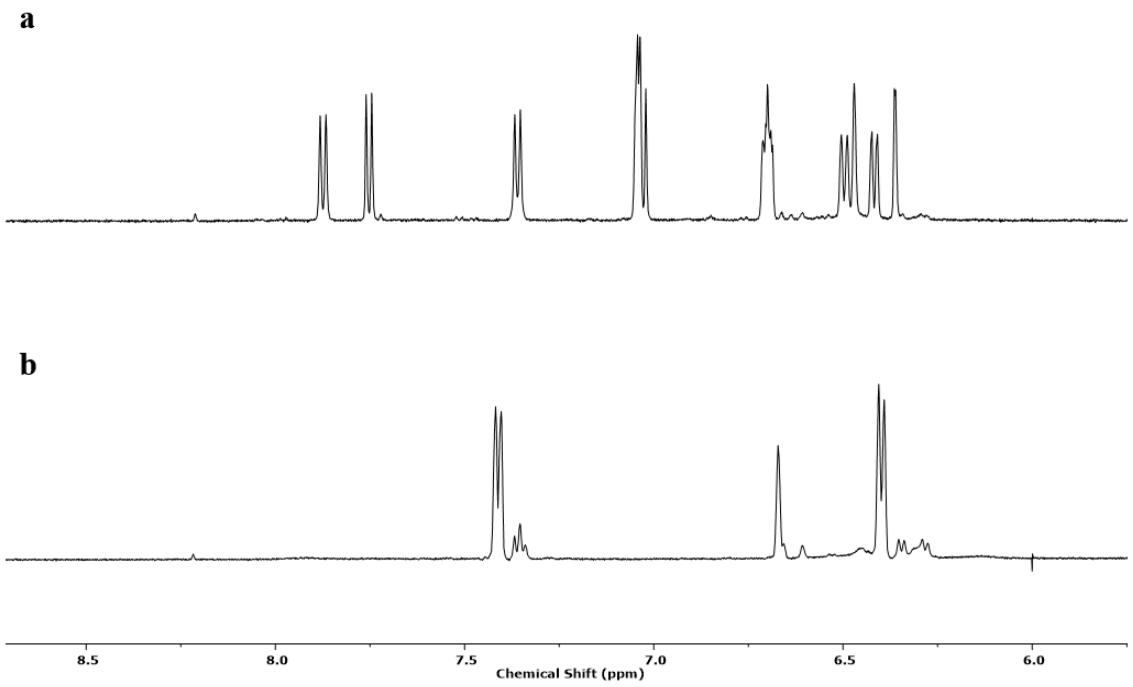

Figure 2.12. ^{1}H NMR study in D_2O of **a)** 40 mM anthrone dissolved in 1 M KOD and spectrum recorded immediately. **b**) Spectrum recorded after 1 week.

Figure 2.12 showed that 2,6-anthrone turned into another species over the week. The new species matched the NMR spectrum of DHAQ, and Figure 2.11e also confirmed its m/z to be the same as DHAQ. Some impurities (20 %) was also observed during this oxidation process. This decomposition-regeneration was stunning, but at the same time it offered an opportunity to rejuvenate the DHAQ flow battery by pumping air through, converting redox-inactive anthrone back to redox-active anthraquinone.

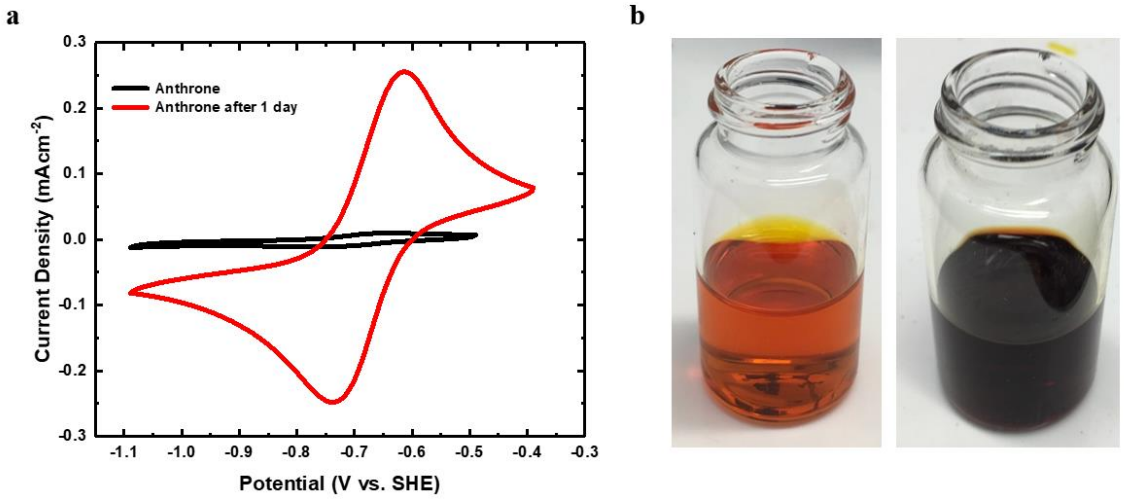

Figure 2.13. a) cyclic voltammetry of synthetic anthrone and the same sample after 1 day of stirring in air. **b)** left: synthetic anthrone in 1 M KOH; right: same sample after 1 day for stirring in air

We demonstrated this regeneration idea by running a cyclic voltammetry on the synthetic anthrone in 1 M KOH (Figure 2.13a, black line), and observed no redox activity. The same sample stirred overnight in air (Figure 2.13b, red line) restored its redox activity, and matched exactly with DHAQ standard. This experiment served as a proof-of-principle study for regenerating the lost capacity in DHAQ, which could potentially dramatically increase the life time of DHAQ vs ferrocyanide flow battery. A later full cell study of DHAQ vs ferrocyanide without nitrogen protection showed a capacity loss of ~0.5 % per day, significantly slower than the full cell tested with nitrogen protection that has a capacity loss of ~ 5% per day.

In addition to converting back to DHAQ, a small amount (20 %) of 2,6-dihydroxyanthrone was also converting to another species (Figure 2.12b, small peaks). The LC-MS chromatograph showed that it had a m/z of 449.1025 for $[M-H]^-$. Indicating the

formation of anthrone dimer. Preparative scale HPLC on the oxidized anthrone sample was performed to isolate the pure side product. Column used was Thermo Scientific Hypersil GOLD aQ 250 X 20 mm with 5μm particle size. NMR confirmed the structure to be anthrone dimer linked through the two de-oxo carbons (Figure 2.14). It should be noted that the electron spray ionization (ESI), a usually soft ionization, can fragment this dimer in LC-MS, showing up m/z of 239.0344 as the predominate ion. 449.1025 parental $[M-H]^-$ can be observed at high concentration loading of anthrone dimer.

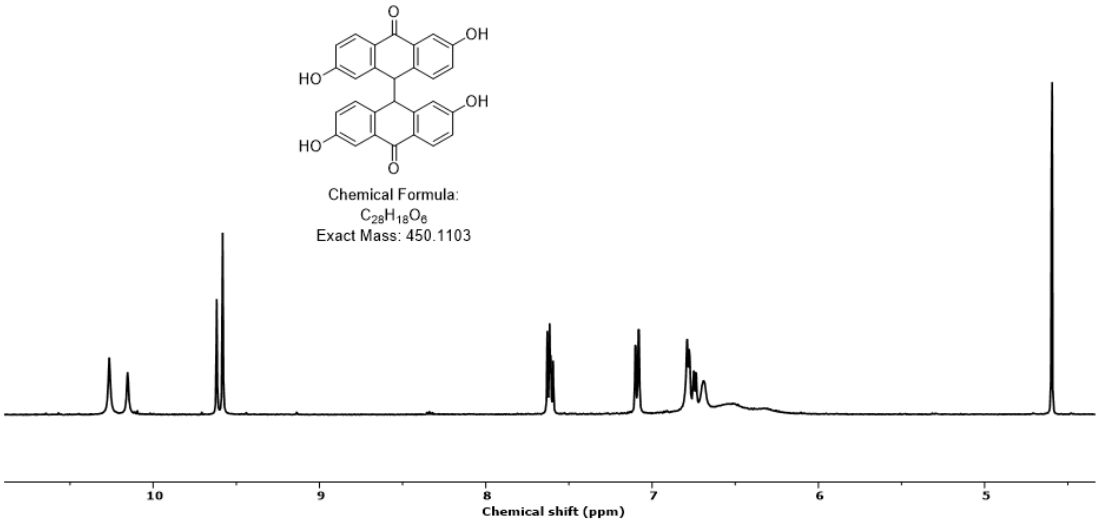

Figure 2.14. Structures of anthrone dimer in DMSO-d_6

Degradation from DHAQ into 2,6-anthrone seemed not just limited to DHAQ, but to be a general mechanism of degradation for anthraquinone based organic molecules in redox-flow battery, as anthrone was observed in other anthraquinone based molecules developed in Gordon and Aziz lab.

2.6 Conclusion

In this work, we chemically synthesized reduced 2,7-anthraquinone-disulfonate (AQDS) in its pure form, and evaluated its optical properties including fluorescent spectroscopy and UV-Vis absorption spectrophotometry in situ, and quantitively calculate the equilibrium constant of quinhydrone formation. Density functional theory (DFT) calculations was also employed to aid the understanding of quinone/hydroquinone interactions and underlying mechanism for quinhydrone formation based on which we estimate a value for the quinhydrone equilibrium constant. UV/VIS spectroscopy has already been established as a valuable tool for those interested in operating commercial flow batteries[16,17]. In situ UV-Vis spectrophotometry while AQDS is cycling was also performed, and by considering quinhydrone formation as well as complexation in the bromine-based positive electrolyte, full-cell and half-cell voltage approximations using the unbound monomer species concentrations applied to the Nernst equation are significantly improved, matching experimentally measured values.

We have also used DHAQ as model system to study the degradation of anthraquinones in alkaline solution during cycling. We demonstrated that DHAQ decomposed into anthrone, which upon contact with oxygen would re-oxidize back to DHAQ (Figure 2.15). This offered a unique opportunity to rejuvenate the DHAQ vs ferrocyanide flow battery

and dramatically improve the lifetime of the molecule.

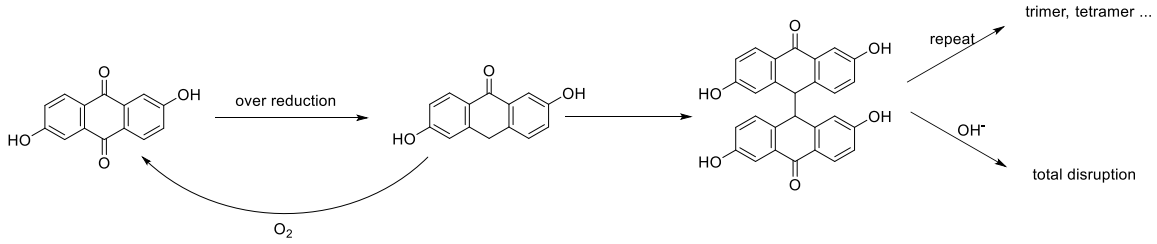

Figure 2.15. Degradation pathway for DHAQ

Chapter 3 Alkaline Benzoquinone Flow Battery

Part of this chapter is published as my co-first author paper.[19] Some details that were published were omitted in this chapter.

3.1 Abstract

We introduce an aqueous flow battery based on low-cost, non-flammable, non-corrosive and Earth-abundant elements. During charging, electrons are stored in a concentrated water solution of 2,5-dihydroxy-1,4-benzoquinone (DHBQ), which rapidly receives electrons with inexpensive carbon electrodes without the assistance of any metal electro-catalyst. Electrons are withdrawn from a second water solution of a food additive, potassium ferrocyanide ($K_4Fe(CN)_6$). When these two solutions flow along opposite sides of a cation-conducting membrane, this flow battery delivers a cell potential of 1.21 V, a peak galvanic power density of 300 mW/cm^2 and a coulombic efficiency exceeding 99%. Continuous cell cycling at 100 mA/cm^2 shows a capacity retention rate of 99.76%/cycle over 150 cycles. Various molecular modifications involving substitution for hydrogens on the aryl ring were implemented to block decomposition by nucleophilic attack of hydroxide ions in solution. These modifications resulted in increased capacity retention rates of up to 99.962%/cycle over 400 consecutive cycles, accompanied by changes in voltage, solubility,

kinetics and cell resistance. Quantum chemistry calculations of a large number of organic compounds predicted a number of related structures that should have even higher performance and stability. Flow batteries based on alkaline-soluble dihydroxybenzoquinone and derivatives are promising candidates for large-scale, stationary-storage of electrical energy.

3.2 Motivation and background

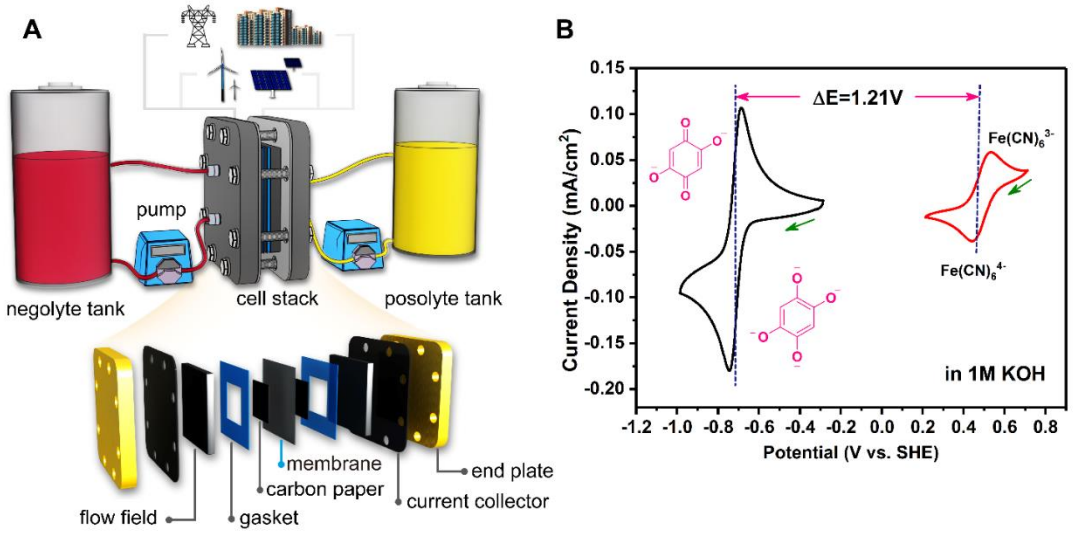

Figure. 3.1 a) Illustration of the AORFB assembled in this contribution. The expanded scheme shows the components of the cell stack. **b)** Cyclic voltammograms of 1mM potassium ferricyanide/ferrocyanide posolyte ($K_3Fe(CN)_6/K_4Fe(CN)_6$, red line) and 1mM DHBQ/reduced-DHBQ negolyte (black line) in 1 M KOH at a scan rate of 10 mV/s. Potentials are referenced to the standard hydrogen electrode (SHE). The theoretical cell potential is determined from the difference in reduction potentials (ΔE) of the posolyte and negolyte.

Small molecule-based AORFBs can be run at acidic [43], neutral [15, 44], or basic pH [11, 17, 45]. Substantially higher cell potentials have been demonstrated in basic pH. A current challenge for AORFBs is reaching high energy density (governed by the product of reactant concentration and cell potential) while keeping reactant cost per kWh of energy storage capacity below the corresponding value for vanadium. Anthraquinone-2,7-disulfonate is a negative reactant with high solubility (2.8 M electrons) for an acidic RFB with cost per kWh roughly 1/3 that of vanadium but, when paired with a bromine/bromide positive reactant, delivers only a modest voltage of 0.81 V [43](Table 3.1 and Figure 3.2). 2,6-dihydroxy-anthraquinone has comparable cost and is soluble in alkaline media (1.2 M electrons), where it has been demonstrated as a negative reactant in a 1.20-volt cell against $K_4Fe(CN)_6$ [11]. Benzoquinones, which are substantially less expensive than anthraquinones (*vide infra*), have been utilized in acidic cells: 4,5-dihydroxybenzene-1,3-disulfonic acid [46-47] and 3,6-dihydroxy-2,4-dimethylbenzenesulfonic acid [48] have each been paired on the positive electrode with anthraquinone-2,6-disulfonic acid on the negative electrode. To date, these cells have been limited by low voltage, with discharge potential < 0.4 V when cycling stably.

Table 3.1. Overview of reported negolytes for aqueous organic flow battery and lab-scale reagent grade prices [a].

Negative electrolyte	FW (g/mol)	Potential (V vs.SHE)	Solubility (mol/L)	No. of electrons delivered	Year of Publication	Cost/Sources ($/g)
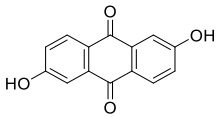 2,6-dihydroxyanthraquinone (DHAQ)	240.2	-0.68 (pH 14)	0.6 M	2	2015[11]	Sigma:19.3 TCI: 59.4 AK: 11.2

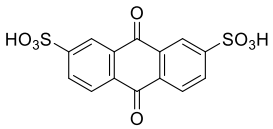					Sigma: 6.6
	368.3	0.22 (pH 0)	1.5 M	2	2014[43]	TCI: 28.2
9,10-anthraquinone-2,7-disulphonic acid						AK: 12.9
AQDS						
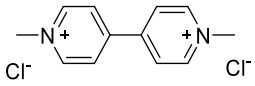					
	257.2	-0.45 (pH 7)	3.0 M	1	2016[13-14]	Sigma:46.8
Methyl viologen					
(MV)					
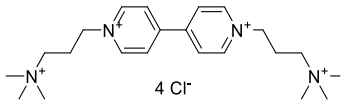					
	500.4	-0.34 (pH 7)	2.0 M	1	2017[15]	3-step lab synthesis
(3-trimethylammonio)propyl					
viologen tetrachloride					
(BTMAP-Vi)					

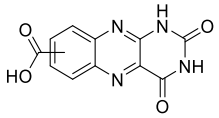 Alloxazine 7/8-carboxylic acid (ACA)	258.2	-0.62 (pH 14)	0.5 M	2	2016[45]	1-step lab synthesis
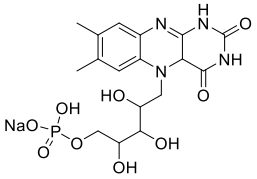 Riboflavin-5'-monophosphate sodium salt (FMN-Na)	480.4	-0.52 (pH 14)	0.24 M	2	2016[17]	Sigma: 3.5 TCI: 3.2 AK: 2.8
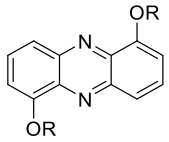 (R is PEGylated TEMPO) Phenazine	785.0	-0.39 (pH 7)	10 mM	2	2016[18]	4-step lab synthesis

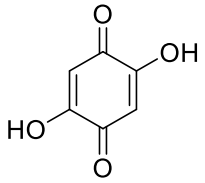 DHBQ	140.1	-0.72	4.31 M	2	This work	Sigma: 2.06 TCI: 2.68 AK: 5.44

[a] Although mass production cost is hard to ascertain for new molecules, the predicted cost vs. quantity curve (Fig. S1, from a consulting company) suggests that the price could be much lower if mass production is guaranteed.

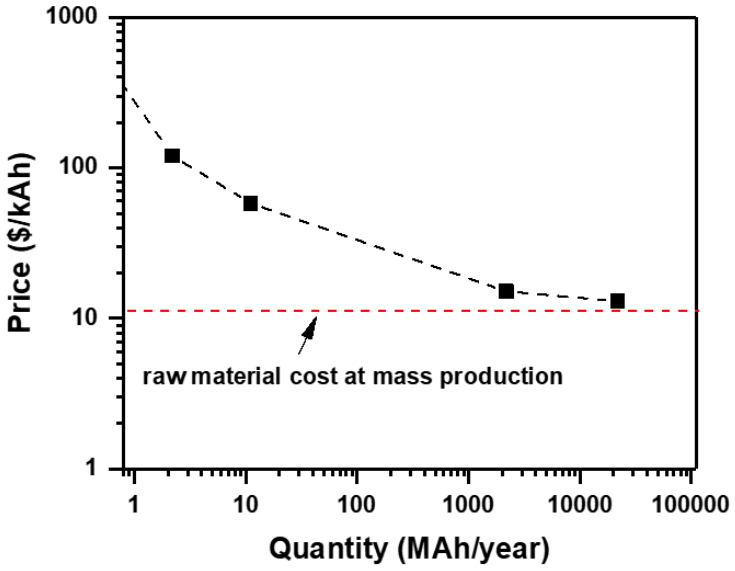

Figure. 3.2 Prediction of anthraquinone (2,6-DHAQ and AQDS) mass production cost as a function of quantity (Sources: Borealis Technology Solutions LLC)

The ultimate goal for organic flow battery reactants is to achieve sufficient stability at a reasonable cost. For long-lifetime projects such as flow batteries for grid storage, discounting can become an important consideration. If the present value of the accumulated annual replacement cost is less than the savings in capital cost compared to vanadium then, other things being equal, the low-cost, shorter-lived reactant is the lower-cost option. This is illustrated in Figure 3.3, which displays the breakeven point for the ratio of the annual replacement cost to the capital cost savings between a lower cost organic electrolyte and a higher cost infinitely stable reactant. For example, if the infinite-life electrolyte cost is 50$/kWh and the low-cost organic reactant costs 10$/kWh but requires 30% be replaced

per year, the breakeven ratio is (30%*10)/ (50-10) = 7.5%. For a 20-year project, replacement of the cheaper shorter-lived reactant becomes the economically favorable choice when the interest rate for discounting exceeds 4%. This requires, of course, that decomposition products do not compromise the battery performance and that replacement is technically achievable and has negligible additional associated costs. We propose that benzoquinone functionalization, similar to the one presented in this study, is a promising path toward achieving this commercialization goal.

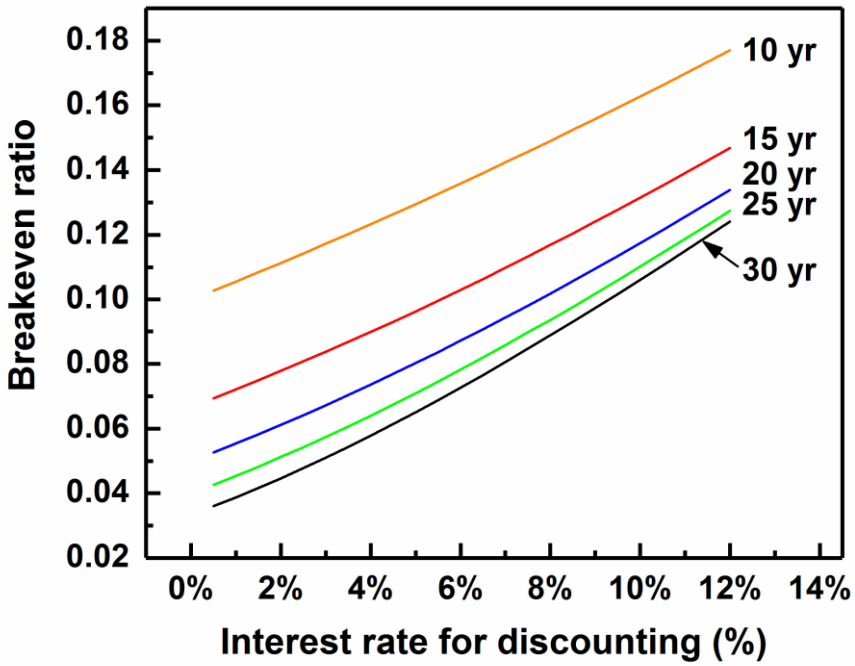

Figure 3.3. Breakeven ratio of annual replacement cost to savings in capital cost vs. interest rate for discounting. A 10 to 30-year project life is assumed.

Here we report the performance of 2,5-dihydroxy-1,4-benzoquinone (DHBQ) as a

promising negolyte (negative electrolyte) material for basic pH. DHBQ is highly soluble in base (> 8 M electrons in 1M KOH) with low reduction potential (-0.72 V vs. SHE at pH 14). Although mass production cost is hard to ascertain for new molecules, our investigation of lab-scale reagent grade prices from commercial vendors suggests DHBQ can be obtained at much lower prices than anthraquinones. (Table 3.1 and Figure 3.2). We paired DHBQ with potassium ferrocyanide to create an AORFB with a cell potential of 1.21 V. Cells exhibited peak power densities of up to 300 mW/cm^2, limited primarily by membrane resistivity, and capacity retention rates upon cycling of up to 99.76% per cycle over 150 cycles. The capacity loss of 0.24% per cycle appears to be caused by a combination of DHBQ crossover through the membrane and the chemical instability of DHBQ. Strategies were undertaken to further raise the capacity retention rate. By blocking the un-substituted carbon atoms in DHBQ, a hydroxylated benzoquinone–based AORFB was attained with improved stability, showing a capacity retention rate of 99.962% per cycle over 400 consecutive cycles, albeit with increased internal resistance.

3.3 Electrochemical characterization

DHBQ is ubiquitous in cellulose products and is the major survivor of bleaching treatment of cellulose products[49]. It is readily formed from the breakdown of cellulose

products and enjoys high resistance towards oxidants such as hydrogen peroxide, ozone and oxygen by virtue of resonance stabilization[49] (Figure 3.4). The accumulation of negative charge at the unsubstituted positions mitigates possible attack by nucleophilic species (e.g. water or OH^-) through Michael addition, which was proposed to be the major mechanism of capacity fade in an AORFB with a 1,2-benzoquinone-3,5-disulfonic acid posolyte (positive electrolyte).[47] The combination of chemical resistance and synthetic accessibility of DHBQ made it a logical alternative to investigate.

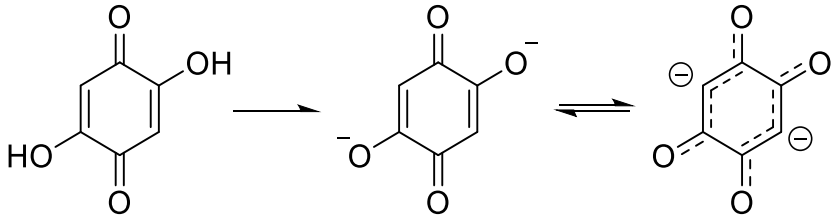

Figure 3.4. DHBQ and its resonance stabilized dianions.

Initial cyclic voltammetry experiments confirmed that DHBQ undergoes reversible two-electron reduction/oxidation, with well-defined anodic and cathodic peaks having a small peak separation (Figure 3.5). In order for DHBQ to be used in a practical cell, it has to have a high solubility at the operating pH. As expected, DHBQ is highly soluble at high pH due to its two solubility-enhancing hydroxy groups, which are deprotonated above pH 10. UV-Vis spectrophotometry of a saturated solution of DHBQ potassium salt in 1 M KOH showed a solubility of 4.31 M (Figure 3.6), which corresponds to a negolyte (negative

electrolyte) capacity of 231 Ah/L. A comparison of DHBQ with other reported AORFB negolytes (Table 3.1) shows that DHBQ enjoys high commercial availability, high solubility, low cost and low redox potential.

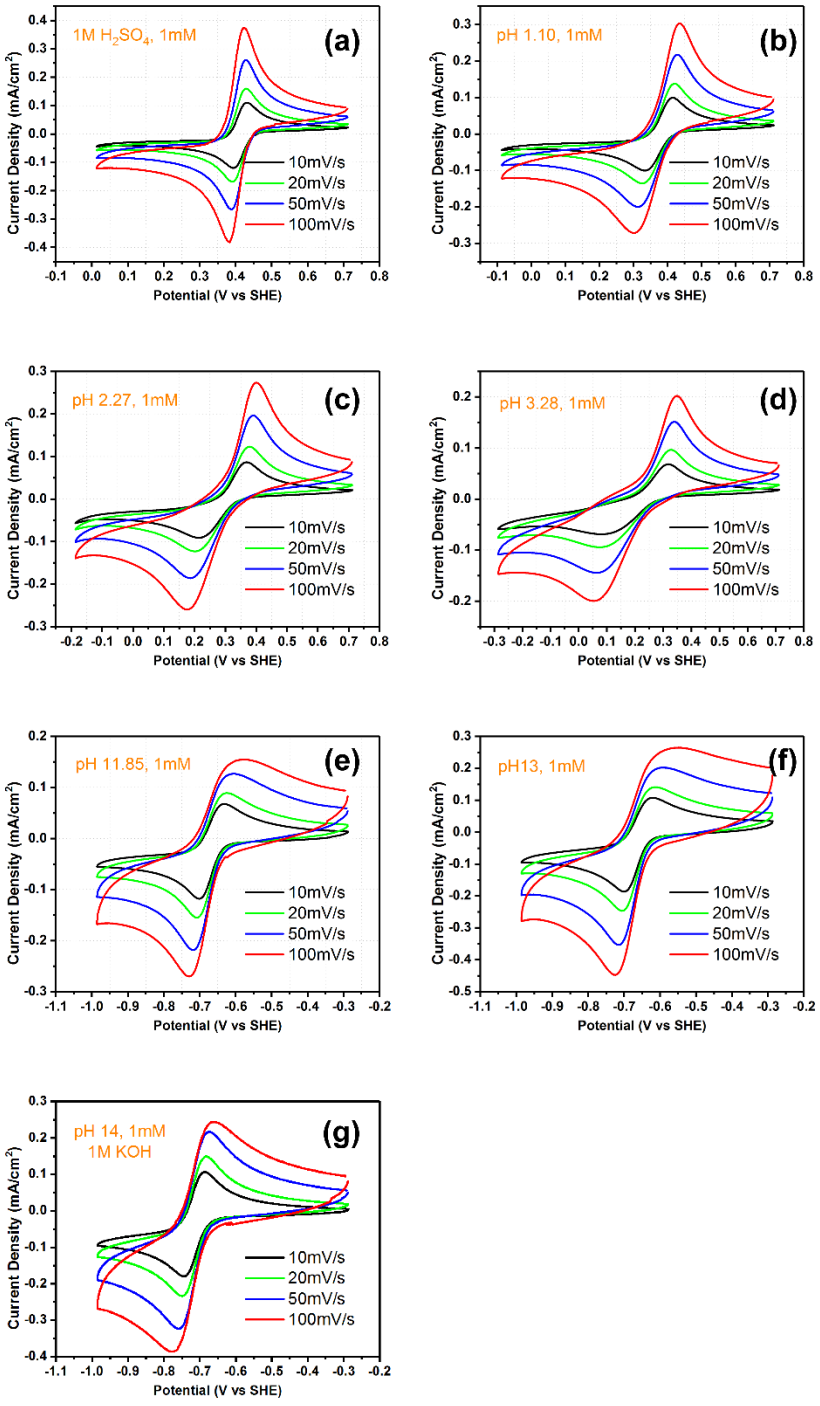

Figure 3.5. Cyclic voltammograms of 1 mM **DHBQ** solution at different pH with varied potential-scanning rates. For b-f, 1 M NaCl was used as the supporting electrolyte. The potential is reported relative to the standard hydrogen electrode (SHE) and is iR-corrected

(pH 0.0, from 1M H_2SO_4 and pH 14 from 1M KOH).

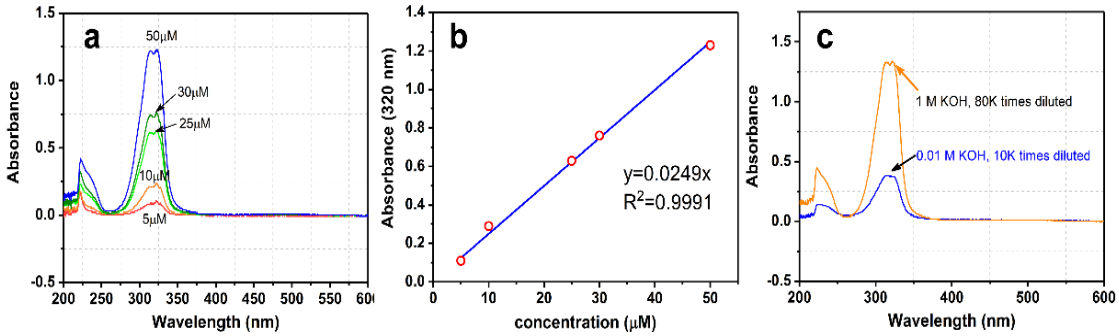

Figure 3.6. a) UV-Vis spectra of **DHBQ** at different concentrations; **b)** the absorbance at 320 nm versus the concentration; a least-squares linear fit to the data was performed to generate the calibration curve utilized in this work; **c)** the absorbance of **DHBQ** solutions in 0.01 M KOH and 1M KOH made by diluting saturated solutions by the ratio indicated in the figure, implying solubilities of 0.15 M and 4.31 M, respectively (note the redox electron concentrations are twice the molecule concentrations).

We performed rotating-disk-electrode experiments to evaluate the reduction kinetics of DHBQ, by sweeping negatively from -0.3 V to -1.4 V vs. SHE. Voltammograms were acquired over a range of rotation rates (Figure 3.7). A diffusion coefficient (D) of 3.66×10^{-6} cm^2/s was determined from a Levich plot of the limiting current vs. square root of rotation rate. A Koutecký-Levich plot reveals good linearity of reciprocal electrode currents against the reciprocal square root of rotation rate at different overpotentials from the formal reduction potential (E^0 = -0.72 V vs. SHE at pH 14). Fitting the kinetically-limited current i_k to the Tafel equation yields an electron transfer rate constant (k^o) of 2.12×10^{-3} cm/s.

Compared with other small redox-active molecules, DHBQ shows a diffusion coefficient similar to those of 9,10-anthraquinone-2,7-disulphonic acid [43], ferrocene derivatives[44], TEMPO derivatives or viologens[13], and slightly higher than those of the sodium salts of flavin mononucleotide[17] and DHAQ[11]. As expected, the experimental diffusion coefficient is 5 orders of magnitude higher than that of the redox-active polymers that have been demonstrated in an aqueous RFB[50]. The electron-transfer rate constant (k^o) is greater than those of ferrocene derivatives[44], alloxazine [45], V^{3+}/V^{2+} and VO^{2+}/VO_2^+ [51], which makes it promising as an AORFB reactant (Table 3.2)

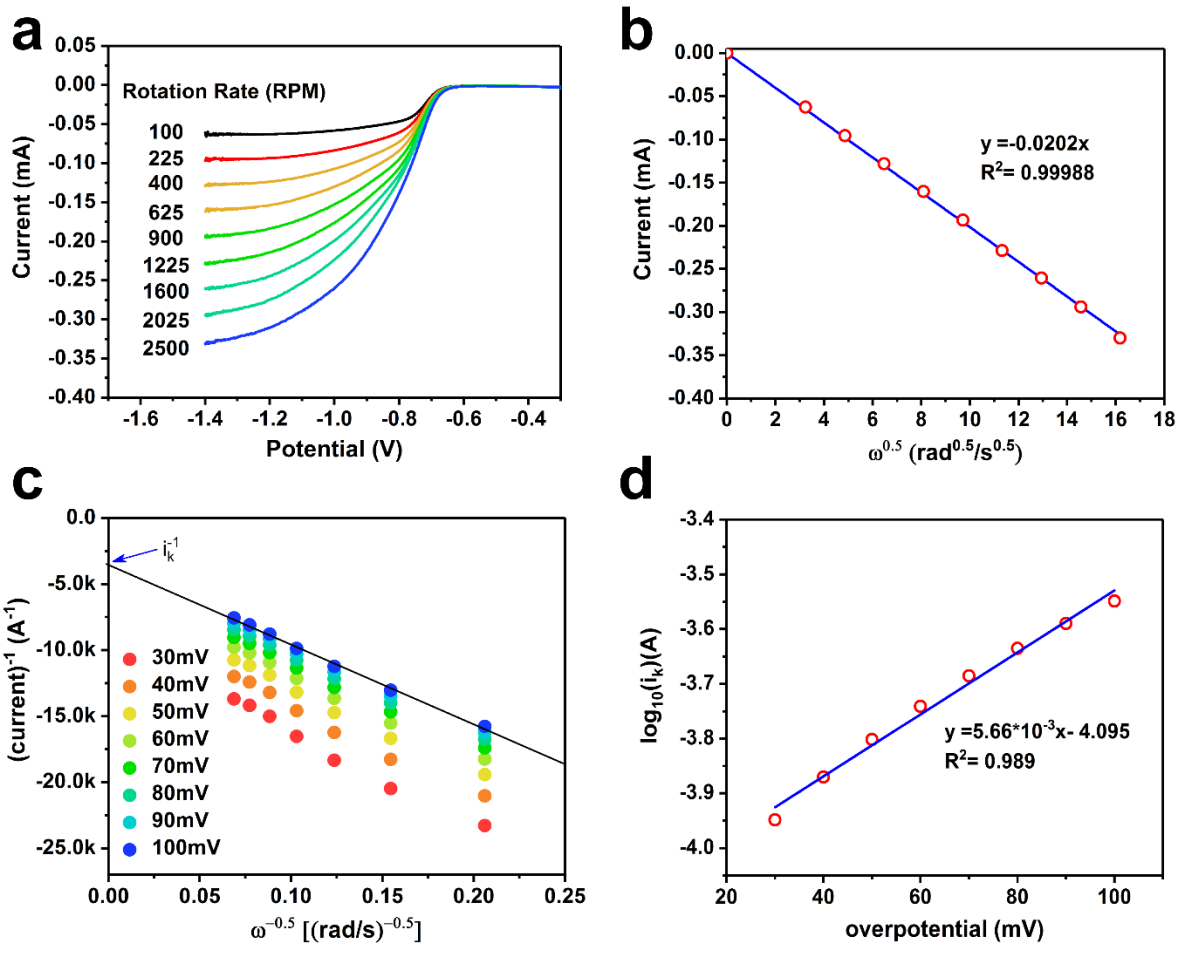

Figure 3.7. Rotating-disk-electrode (RDE) experiment on DHBQ (1 mM in 1 M KOH). **a)** Current versus potential at rotation rate from 100 rpm to 2500 rpm with potential sweep rate of 5 mV/s; **b)** Levich-plot of limiting current versus square root of rotation rate ($\omega^{1/2}$); **c)** Koutecky-Levich plot at different over-potentials; reciprocal of kinetically limited current is indicated on vertical axis. **d)** Tafel plot, the logarithm of kinetically-limited current vs. overpotential (potential deviation from the formal reduction potential).

Table 3.2. The diffusion coefficient (D) and electron-transfer rate constant (k^o) of presentative redox couples at glassy carbon electrode

Redox couple	D (cm^2/s)	k^o(cm/s)	Ref
FcNCl	$3.74*10^{-6}$	$3.66*10^{-5}$	44
FcN_2Br_2	$3.64*10^{-6}$	$4.60*10^{-6}$	44
alloxazine	-	$1.2*10^{-5}$	45
V^{3+}/V^{2+}	$4*10^{-6}$	$1.7*10^{-5}$	52
VO^{2+}/VO_2^{+}	$1.4*10^{-6}$	$7.5*10^{-4}$	53
DHBQ	$3.66*10^{-6}$	$2.12*10^{-3}$	this work

3.4 Full cell cycling analysis

To demonstrate the capability of DHBQ as the negolyte for an alkaline AORFB, a lab-scale AORFB prototype was assembled using graphite flow plates with serpentine flow fields. The positive reservoir (6 mL) comprised 0.4 M potassium ferrocyanide ($K_4Fe(CN)_6$) in 1 M KOH and the negative reservoir (22.5 mL) was assembled from 0.5 M of DHBQ in 2 M KOH (1 M OH^- was consumed in deprotonating DHBQ). A lower DHBQ concentration than the solubility limit was utilized to ensure osmotic balance with the ferrocyanide posolyte, which has a limited solubility in 1M KOH. The theoretical cell potential of DHBQ/$K_4Fe(CN)_6$in 1 M KOH is 1.21 V(Figure 3.1). We varied the state of

charge (SOC) by a constant-coulomb incremental charging technique from 10% to ~100% and recorded the corresponding open-circuit voltage. The cell potential at 10% SOC is 1.141 V and climbs up to 1.202 V at 50% SOC. The cell voltage reaches 1.255 V at ~100% SOC.

Initial cell performance was evaluated with three different commercial cation exchange membranes, namely Nafion 212 (N212), Nafion 115 (N115) and Nafion 117 (N117). Polarization curves (Figure 3.8) show that the cells assembled with N212, N115 and N117 exhibit peak power densities of 300 mW/cm^2, 164 mW/cm^2 and 137 mW/cm^2, respectively. The difference in peak power density results from the overall cell resistance as reflected in the potential-current curves.

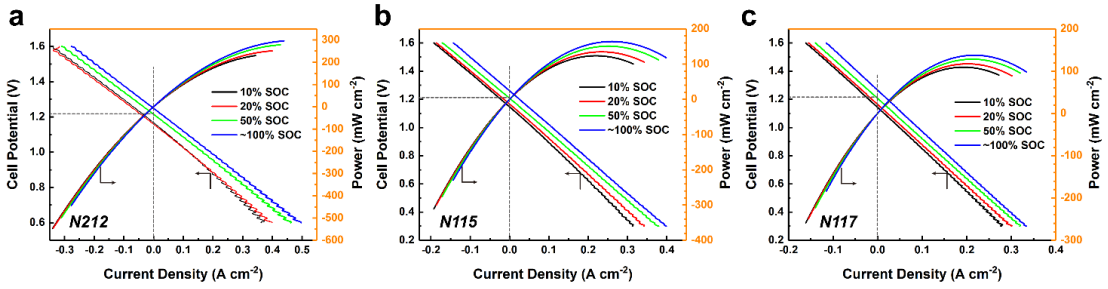

Figure. 3.8 Electrochemical performance of a DHBQ/$K_4Fe(CN)_6$ cell. Electrolytes comprise 6 mL of 0.5 M DHBQ in 2M KOH (the negolyte) and 22.5 mL of 0.4 M potassium ferrocyanide ($K_4Fe(CN)_6$) in 1M KOH (the posolyte). The cell-polarization plots, composed of cell potential (left vertical) and power density (right vertical) versus discharge current density, correspond to the cell assembled with **a)** Nafion 212 membrane (N212), **b)** Nafion 115 membrane (N115) and **c)** Nafion 117 membrane (N117). The dashed lines indicate open circuit potential at 50% SOC.

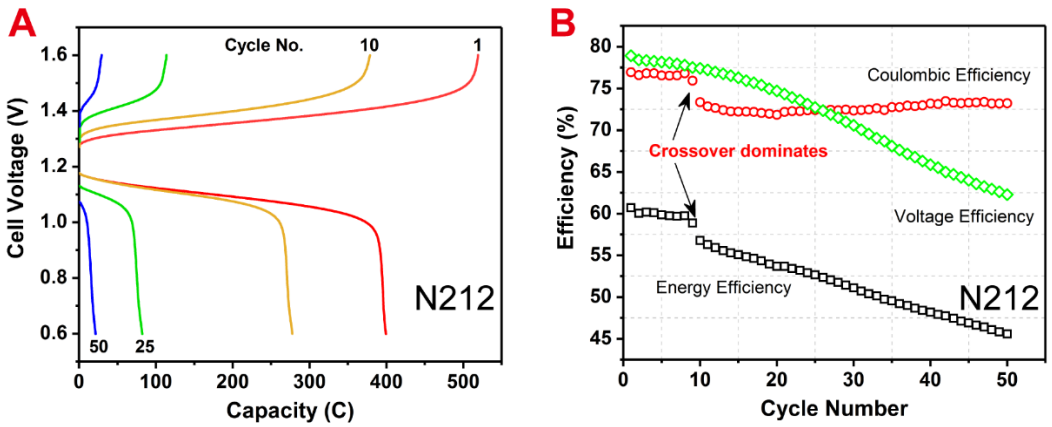

Figure. 3.9 Cell cycling performance of a **DHBQ**/$K_4Fe(CN)_6$ cell with a Nafion 212 separator. The electrolytes comprise 6 mL of 0.5 M **DHBQ** in 2 M KOH and 22.5 mL of 0.4 M $K_4Fe(CN)_6$ in 1M KOH and the cells are cycled at 100 mA/cm^2 with potential cut-offs of 1.6V and 0.6 V. The potential was not maintained at the cut-off potentials once they were reached. For clarity, representative cell potential versus capacity curves (A) and efficiencies (coulombic efficiency, energy efficiency and voltage efficiency, B) over the whole cycling process are presented. Each cycle takes approximately 38 min.

Cell cycling experiments were conducted to evaluate the capacity retention rate of the DHBQ/$K_4Fe(CN)_6$ cell. Prior to cycling, the cell capacity was evaluated with a full charge-discharge process to be 531.4 C, which is 91.8% of the theoretical value (578.9 C in 6 mL negolyte). When cycled galvanostatically at 100 mA/cm^2 between voltage cutoffs of 1.6 and 0.6 V, the initial capacity was 23.15 Ah/L, which is 86.4% of the theoretical capacity, 26.79 Ah/L. We tentatively attribute the value of 91.8% to DHBQ purity and transfer loss, the difference between 91.8% and 86.4% to overpotential during cell cycling. The DHBQ/$K_4Fe(CN)_6$ cell assembled with the N212 membrane suffers from severe capacity fade (Figure 3.9). The coulombic efficiency (CE), which is the ratio of the discharge

capacity to the immediately preceding charge capacity, is around 77% and drops to 72.5% after 10 cycles. The low value of the CE indicates that self-discharge of the N212-cell is taking place during cycling, which we hypothesize to be caused by crossover of active electrolytes across the membrane. The high DHBQ crossover rate stems from its small molecular size as well as the high water-uptake and small thickness of N212 membrane. On the one hand, by switching to thicker membranes, N115 and N117 (Figure 3.10), a clear increase in the coulombic efficiency of the cell of up to 99% is observed. This coulombic efficiency remains high during cycling, suggesting a reduced membrane crossover rate of the capacity-limiting reagent, DHBQ. The same capacity is obtained at 100 mA/cm^2 with either the N115 or the N117 membrane, but not with N212. On the other hand, thicker membranes contribute a higher area-specific resistance, as reflected in the polarization curves (Figure 3.8); high resistance in turn leads to decreased round-trip energy efficiency (EE). The EE of N117-based DHBQ/$K_4Fe(CN)_6$ cell is around 61% at first and stabilizes at ~ 56%, whereas it is slightly higher for a N115-based DHBQ/$K_4Fe(CN)_6$ cell and remains comparatively stable at 65%. If the current efficiency loss current is independent of current density, then the EE of the N115 cell can be increased to ~88% by reducing the current density to 15 mA/cm^2 – but at an increased capital cost per kW due to the large cell area per unit current.

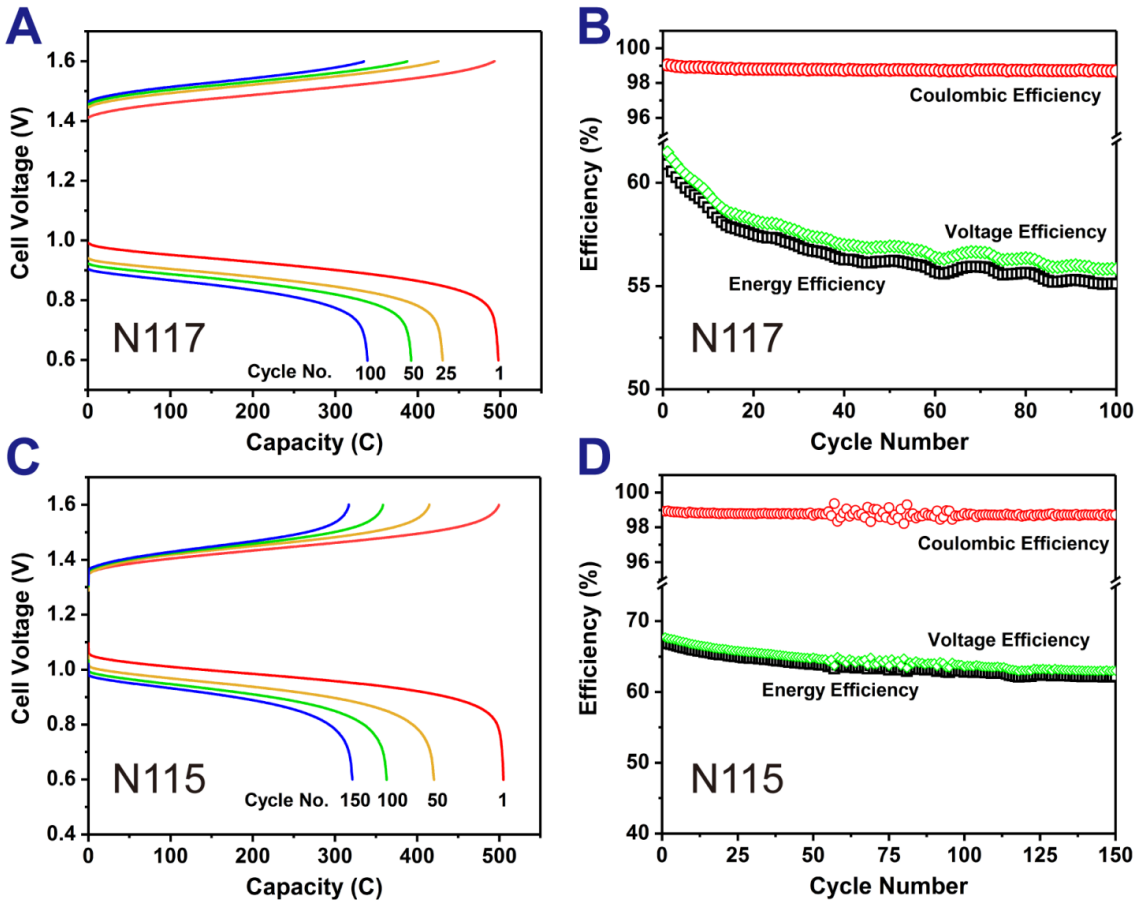

Figure. 3.10 Prolonged galvanostatic cell cycling performance of Nafion-based DHBQ/$K_4Fe(CN)_6$ cell at 100 mA/cm^2 with potential cut-offs of 1.6V and 0.6 V. No potential holds were employed. The electrolytes comprise 6 mL of 0.5 M DHBQ in 2 M KOH and 22.5 mL of 0.4 M $K_4Fe(CN)_6$ in 1 M KOH. Representative cell potential versus capacity curves (A and B for Nafion 117 membrane, C and D for Nafion 115 membrane) and efficiencies (coulombic efficiency, energy efficiency and voltage efficiency) over the whole cycling process are presented.

The capacity retention rates for N115-based and N117-based cells are 99.76% and 99.68% per cycle, respectively. Although the cell remains quite stable from each charge-discharge cycle to the next, the accumulation of the tiny capacity fade during prolonged cycling is not ideal for practical application. The capacity fade rate for the N115-based cell of 0.24% per cycle extrapolates, assuming exponential decay, to 290 cycles before the capacity drops to 50% of the original, which is inadequate for practical application.

3.5 Degradation analysis

3.5.1 Methods

High-Resolution LC-MS. High-resolution LC-MS analyses of DHBQ decomposition was performed in the Small Molecule Mass Spectrometry Facility on a Bruker Impact II q-TOF with internal calibration sodium formate clusters. Liquid chromatography was performed on an Agilent 1290 Infinity HPLC using a Dikma Platisil PH column (150mm, 5um particle size, 4.6mm ID, catalog number 99510) at a flow rate of 0.4 mL/min and the following elution conditions were applied: 100% solvent A for 2 min, a gradient increasing from 0% to 15% solvent B in solvent A over 13 min, a gradient increasing to 100% solvent B over 5 min, a gradient decreasing to 0% solvent B in solvent A over 0.1 min, and 100% solvent A for 4.9 min (solvent A = 0.1% v/v formic acid in water; solvent B = 0.1% v/v formic acid in acetonitrile). The ESI mass spectra were recorded in negative ionization

mode.

Permeability measurements (conducted by Dr. Diana De Porcellinis). The permeability of DHBQ across the membrane was evaluated with a lab-made two compartment cell[15]. The donating side was filled with a solution of DHBQ (0.5 M) in KOH (1 M) and the receiving side was filled with 1 M KOH. Both compartments had the same volume. The cell was continuously agitated on a nutating table. At different time intervals, aliquots were taken from the receiving side, diluted and characterized by UV-Vis spectrophotometry. The concentration was calculated from a calibration curve. The permeability was then calculated based on Fick's law, using equations as follows.

$$P = \frac{c_t V_0 l}{At(c_0 - c_t)} \approx \frac{c_t V_0 l}{Atc_0}$$

Where, P is the permeability (cm^2/s), A is the effective area of the membrane (0.942 cm^2), t is the elapsed time (s), c_t is the concentration of active species in the receiving side at time t (mol/L), V_0 is the volume of the solution in either compartment (5 cm^3), l is the thickness of the membrane (127 μm), and c_0 is the concentration of DHBQ in the donating side (0.5 mol/L).

3.5.2 Analysis

By reducing the volume of the positive reservoir, a DHBQ/$K_4Fe(CN)_6$ cell that was capacity-limited by the posolyte was assembled and cycled. Results show that discharge capacity of the cell remained unchanged for the first 45 cycles (around 20 hours), although the charge-capacity varied slightly. This implies that $K_4Fe(CN)_6$ loss is not contributing to the capacity loss of the DHBQ/$K_4Fe(CN)_6$ cell.

Dr. Diana De Porcellinis conducted the cross over experiments. The crossover rate of DHBQ across a N115 membrane was measured in a two-compartment rotating cell. The DHBQ concentration in the receiving reservoir was found to increase linearly over time, indicating a permeability of $1.27*10^{-9}$ cm^2/s. Considering the time every cycle takes, the effective membrane area and the reservoir volume of the cell, the expected capacity loss caused by DHBQ crossover would be 0.012% per cycle. Although the membrane properties in a static permeability measurement may not permit one to accurately infer its properties in a cycling cell, this is more than an order of magnitude below the observed capacity loss rate in a cycling N115-based DHBQ/$K_4Fe(CN)_6$ cell (0.24% per cycle). The discrepancy suggests molecular decomposition as a potential mechanism of capacity fade. This hypothesis was then tested by separate experiments, in which the negolyte solution composition after cell cycling, and DHBQ stored in alkaline solutions at elevated

temperature, were both analyzed using NMR. A typical ^{1}H-NMR spectrum (Figure 3.11) was too complicated to interpret and suggests the coexistence of multiple species. However, more information was extracted from the ^{13}C-NMR spectra (Figure 3.12). According to the standard spectra of DHBQ in DMSO-d_6 provided by Sigma-Aldrich, two carbon signals should be observed, one at 105 ppm and the other at around 172 ppm; however, the latter is broad and could hardly be observed. After 300 cell cycles, a new peak was observed at 162 ppm, indicating the generation of a new species during cycling. Combined with the information obtained from the ^{1}H-NMR spectrum, we conclude that multiple species are generated during cell cycling although their concentrations are not high enough to be clearly observed in the ^{13}C-NMR spectra. In a separate experiment, in which the oxidized form of DHBQ was subjected to prolonged ex-situ alkaline treatment at an elevated temperature of 80 °C for 40 days, no carbon peaks at all could be observed, indicating that DHBQ had degraded chemically into possibly smaller fragments.

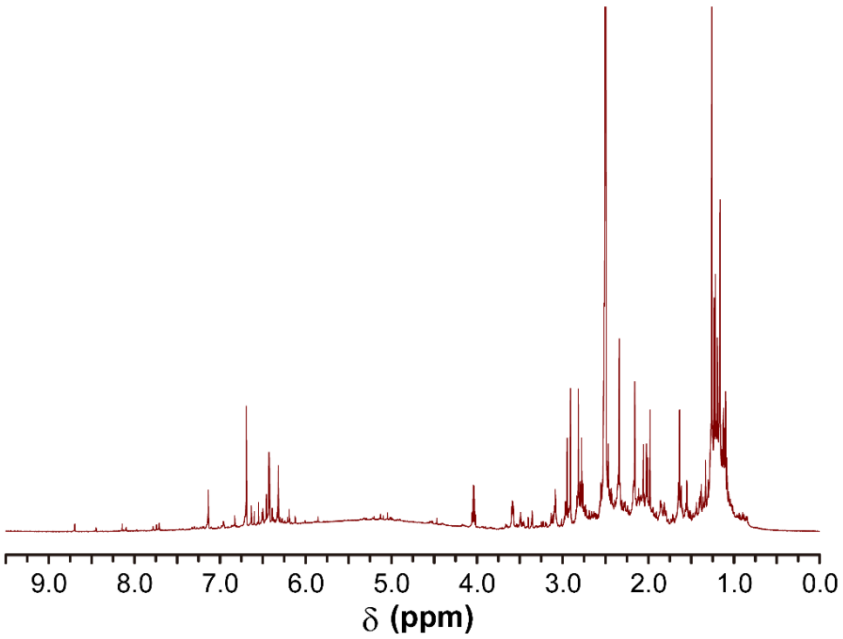

Figure. 3.11 A typical ^{1}H-NMR spectrum recorded in DMSO-d_6 for **DHBQ** after cell cycling. After prolonged cell cycling, the anolyte reservoir was neutralized with HCl and evaporated under vacuum at 40 °C. The remaining solids were dissolved in DMSO-d_6.

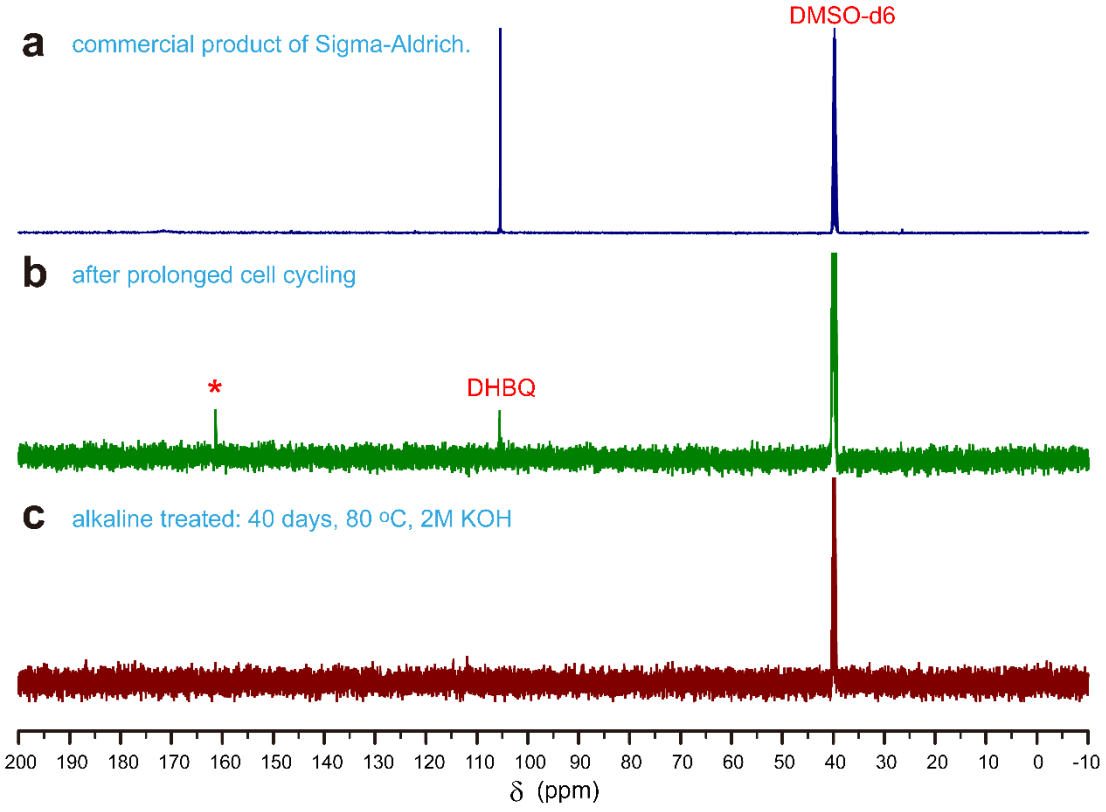

Figure. 3.12 ^{13}C NMR of (a) commercial **DHBQ** from Sigma-Aldrich, (b) the **DHBQ** anolyte after prolonged cell cycling and (c) 2 M KOH–treated **DHBQ** at 80 °C after 40 days. The asterisk indicates the appearance of a new carbon signal. All spectra were recorded in DMSO-d_6 on Varian INOVA 500 spectrometers (500 MHz for ^{1}H, 125 MHz for ^{13}C). During ex-situ alkaline treatments, the sample solutions (10 mL, flushed with N_2 for 15 mins) were kept in a glass via (20 mL), sealed with PTFE tape and parafilm.

LC-MS analysis of a fresh DHBQ solution shows a single peak at a retention time of 14–15 min, with a mass(m/z) of 139.0037, which agrees exactly with the chemical structure. Although DHBQ could be detected in the LC-MS spectrum of the alkaline treated DHBQ solution, multiple peaks were observed, which is consistent with the results we obtained in NMR study (Figure 3.13). Despite the fact that LC-MS was able to detect the mass of each peak, we have not yet determined the degradation mechanism. Our working hypothesis is that the chemical decomposition of DHBQ during cell cycling is possibly caused by nucleophilic attack of the hydroxide ions on the un-substituted carbon atoms of DHBQ.

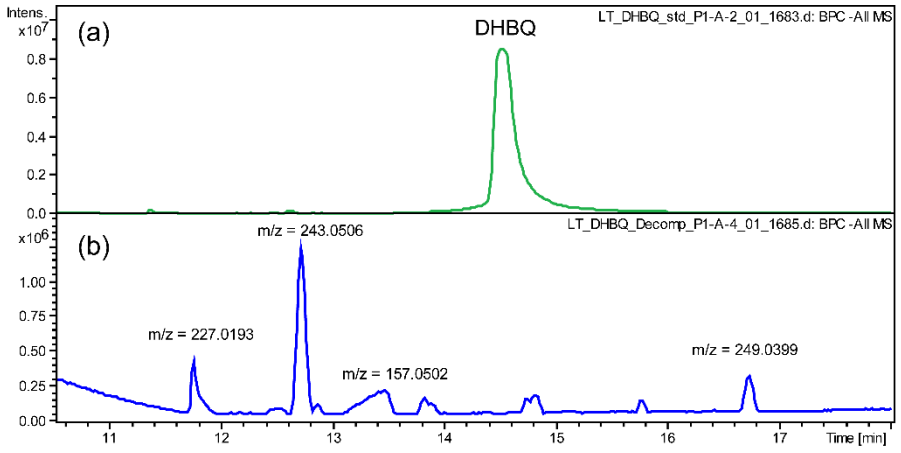

Figure. 3.13 (a) Base Peak Chromatograph of **DHBQ** standard and (b) **DHBQ** treated in pH14 KOH solution for 40 days. Mass with highest intensity in representative decomposition peak was annotated above the corresponding peak (within 5 ppm error and correct isotopic pattern).

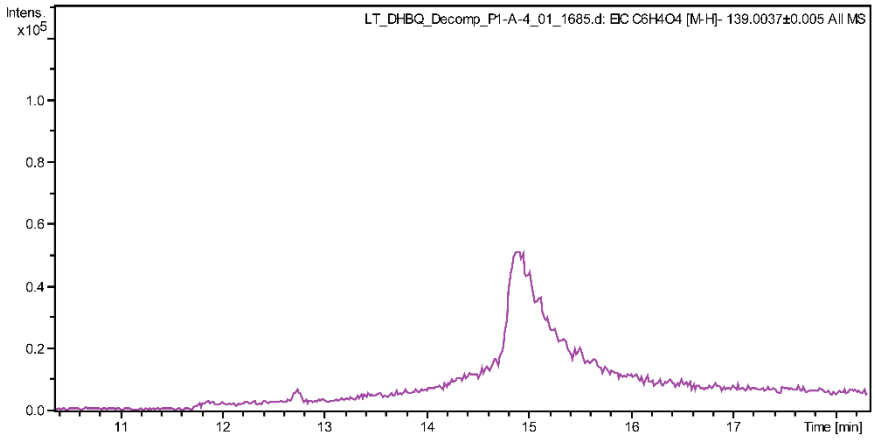

Figure. 3.14 Extracted ion chromatograph ($C_6H_4O_4$ $[M-H]^-$) of decomposed **DHBQ**.

3.6 Structure modification of DHBQ

The appearance of multiple NMR peaks in 0 – 3 ppm indicates the formation of multiple fragments of smaller molecular weights. This is further confirmed by detecting multiple lower mass molecules in LC-MS. It has been proposed that the degradation of benzoquinones in acidic conditions is caused by Michael addition[47] of water molecules onto the electrophilic site of benzoquinone molecule. In basic pH, hydroxide ions are stronger nucleophiles than is water in acid. In contrast to reports that a stable hydroxy-

added Michael addition product can be formed, based on the NMR and LC-MS data indicate a cascade of further degradation takes place afterward. Therefore, we strive to mitigate the initial Michael attack by blocking the open position on DHBQ.

3.6.1 Improved stability by substituting DHBQ open sites

Synthetic efforts were made to verify the effectiveness of improving the chemical stability of DHBQ by blocking the un-substituted positions. 3,6-bis(diphenylmethyl)-2,5-dihydroxy-1,4-benzoquinone (DPM-DHBQ) was synthesized using a reported procedure and characterized by cyclic voltammetry (Scheme 3.1). Results indicate that DPM-DHBQ is redox-active and the reduction and oxidation occur at -1.0 V and -0.5 V, respectively, showing a half-wave potential of roughly -0.75 V vs. SHE (Figure 3.15). The redox potential is close to that of DHBQ, and the peaks remain unchanged during repeated scans. However, adding extra aromatic rings to block the un-substituted carbon atoms led to an increased peak separation in the CV, implying sluggish redox kinetics on glassy carbon. Incorporating extra aromatic rings also caused a severe decrease in solubility that precluded full cell studies.

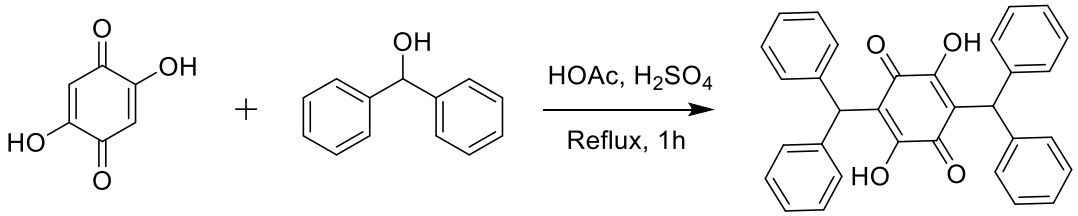

Scheme 3.1. Synthesis of **DPM-DHBQ**.

3,6-Bis(diphenylmethyl)-2,5-dihydroxy-1,4-benzoquinone (DPM-DHBQ). The synthesis of **DPM-DHBQ** was carried out according to reported procedure (**Scheme 1**)[54]. 2,5-dihydroxybenzoquinone (DHBQ, 2.00 g, 14.3 mmol), diphenylmethanol (5.50 g, 29.9 mmol) and concentrated sulfuric acid (0.5 mL) were refluxed for 1 h in 20 mL of acetic acid. The resulting solution was cooled to room temperature and the product precipitated out. The precipitate was crushed with a spatula and collected by vacuum filtration. The collected yellow crystals were washed with a small amount of acetic acid and then with DI water. The product was finally dried overnight in air at 95 °C. To ensure purity for electrochemical study, it was further purified by recrystallization from acetic acid. NMR of the product matched previously reported values in the literature.

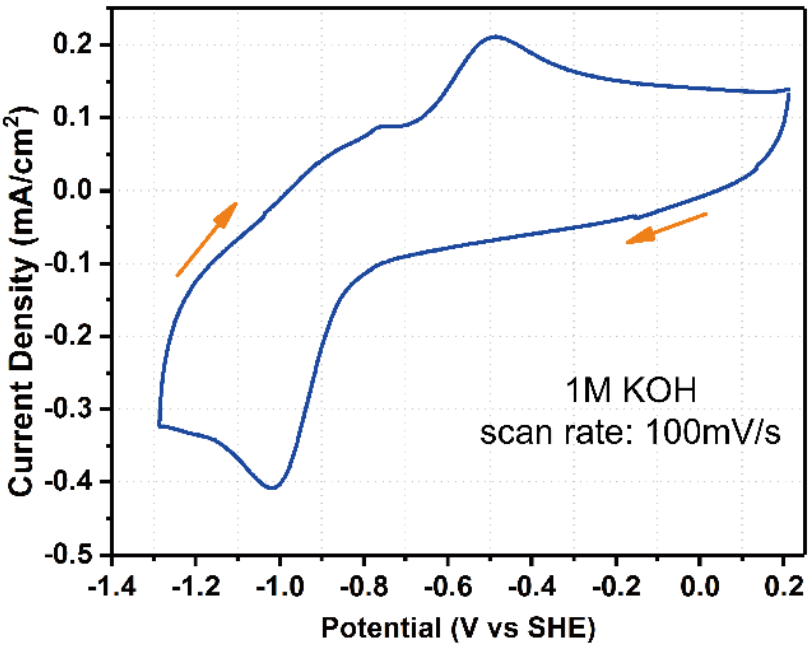

Figure. 3.15 Cyclic voltammogram of 3,6-bis(diphenylmethyl)-2,5-dihydroxy- 1,4-benzoquinone (**DPM-DHBQ**) recorded in 1 M KOH. The potential is referenced to the standard hydrogen electrode (SHE) and the potential sweep rate is 100 mV/s. The CV is reproducible in repeated scans and only one curve is presented for clarity (the 10th scan).

Since DPM-DHBQ was too insoluble for any practical battery application, we seek to modify DHBQ with only one phenyl rings following a literature preparation[55] (Scheme 2) to afford a dimethoxydiphenyl-DHBQ. Removing the methoxy group was realized by standard deprotection procedure using BBr_3 in dichloromethane to yield a brown powder with has a solubility of ca. 0.2 M in 1M KOH.

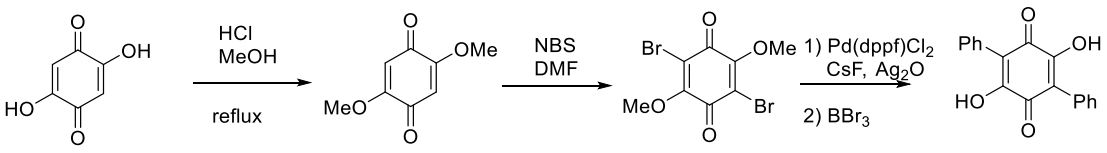

Scheme 3.2. Synthesis of **DP-DHBQ**.

3,6-Bis(diphenyl)-2,5-dihydroxy-1,4-benzoquinone (DP-DHBQ). The synthesis of **DP-DHBQ**. 3,6-Bis(diphenyl)-2,5-dimethoxy-1,4-benzoquinone (1.5 g, 4.68 mmol) in dichloromethane (50 ml) was cooled to – 79 °C. The reaction mixture was slowly added BBr_3 (14 mL, 1 M in DCM). The mixture was allowed to warm to room temperature and stirred for 7 hours. The resulting mixture was added water and filtered through Celite and concentrated in vacuo to afford a black colored solid. The solid was dissolved in 1 M NaOH (20 mL) and extracted with EtOAc (2 x 20 mL). The aqueous phase was added 3 M HCl (20 mL) and extracted with DCM (3 x 10 mL). The combined organic phase was concentrated in vacuo to afford a brown powder (0.45g, 33%)

The stability of DP-DHBQ was evaluated by CV. A 2 mM DPDHBQ was prepared in 1M KOH, and CV was recorded. The same solution was left on the bench without protection, and CV was recorded after 1 day. 2 CV curves nearly overlap with each other with no appreciable decrease in peak height for the 24-hour sample. This is in contrast with DHBQ in alkaline solution, in which it usually loses ca. 10% of CV activity. DP-DHBQ illustrated the successful application of blocking strategy in making a more stable redox active molecule.

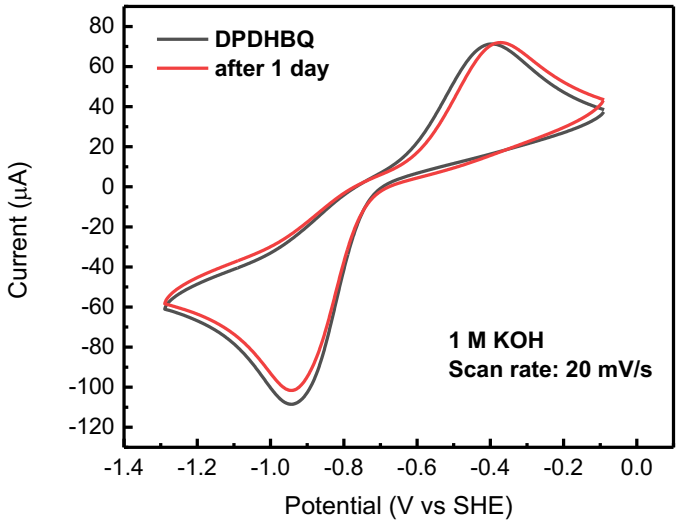

Figure. 16 Cyclic voltammogram of 3,6-Bis(diphenyl)-2,5-dihydroxy-1,4-benzoquinone **(DP-DHBQ)** recorded in 1 M KOH. The potential is referenced to the standard hydrogen electrode (SHE) and the potential sweep rate is 20 mV/s. The CV is reproducible in repeated scans and only one curve is presented for clarity (the 3rd scan).

Although that blocking the free site on DHBQ does not fully prevent the degradation, but DP-DHBQ illustrated the successful application of blocking strategy in making a more stable redox active molecule, at least by slowing down proposed the initial Michael attack. From a fundamental science perspective, we were also interested in studying the structure-stability relationship of substituted DHBQ. Practically, we would synthesize DHBQ with increasing size of alkyl or alkoxy groups, and study their decreased degradation rate during cycling. Both series of DHBQ can be easily synthesize according to literature procedure with modification. The dialkyl substituted DHBQ can be synthesized from simple dialkylbenzoquinone. Aziridination of dialkylbenzoquinone affords diaziridinyl-dialkylbenzoquinone.[56] Subsequent hydrolysis of nitrogen-carbon bond in alkaline solution

easily affords alkyl substituted DHBQ.[57] The dialkoxy substituted DHBQ can be synthesized from a simple 2 step reaction starting from chloranil. Sodium alkoxide substitution of chloranil yields tetra-alkoxybenzoquinone, which can be selectively hydrolyzed in alkaline solution to desired dialkoxy substituted DHBQ.[58] A complete evaluation of the structure-stability relationship will be explored in future endeavor

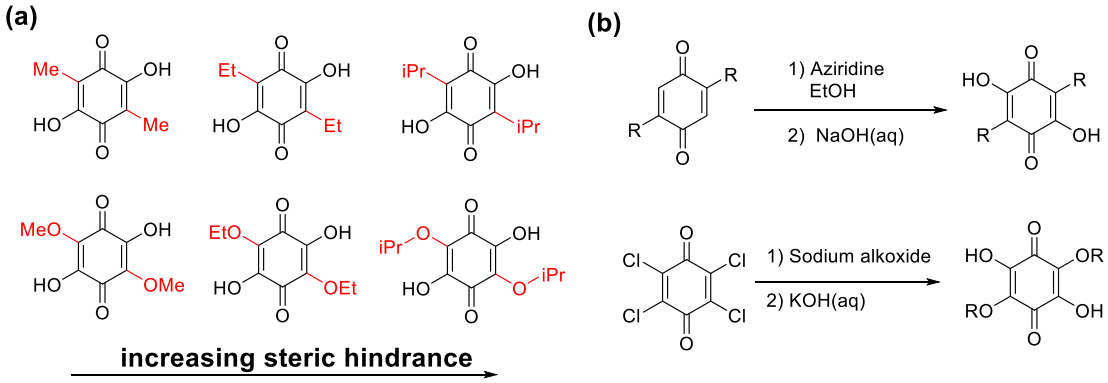

Scheme. 3.3 (a) DHBQ with alkyl or alkoxy groups of increasing steric hindrance. (b) synthetic scheme for alkyl or alkoxy substituted DHBQ.

3.6.2 Improved stability by polymerization

Despite that adding substitution groups to DHBQ can improve the stability, the increased molecular weight and decreased solubility both lead to a battery with decreased energy density. Alternatively, the vulnerable 3- and 6- positions on DHBQ can also be blocked by polymerization. The polymerization of benzoquinone in alkaline solutions (polyBQ, Scheme 3) and the acid-catalyzed condensation of DHBQ with formaldehyde[59]

generate polymers that have repeating units with a similar structure to DHBQ. Each repeating DHBQ unit will contribute to the overall solubility, and we anticipate such structures would be redox-active but no longer susceptible to nucleophilic attack.

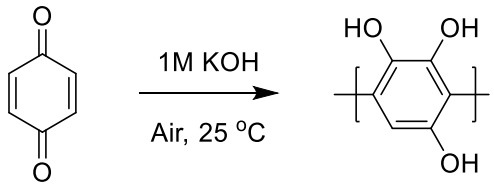

Scheme 3.4. Polymerization of benzoquinone in aqueous alkali (1 M KOH, bubbled air, room temperature)

Polybenzoquinone (PolyBQ). PolyBQ was synthesized according to published procedure (**Scheme 3**)[60]. Benzoquinone (2.70g, 25 mmol) was added to aqueous KOH (25 mL, 1 M) and a considerable amount of heat was immediately generated. The mixture was vigorously stirred and cooled to room temperature. The reaction vessel was sealed with a septum and air was driven through the solution via a needle. To prevent the loss of water, the gas inlet was connected to a bubbler containing a solution of 1 M KOH. After 24 h of reaction, concentrated HCl was added and the neutralized solution was cooled. The precipitated polymer was collected by filtration, washed with DI water and finally dried at 90 °C under vacuum for 6 h.

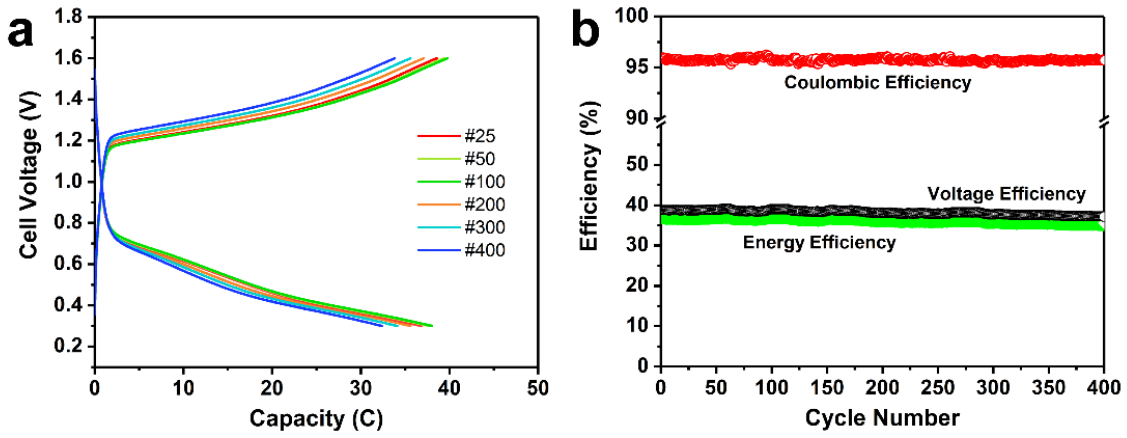

Figure. 3.17 Cell cycling performance of a polyBQ/ $K_3Fe(CN)_6$ cell utilizing Nafion 115. Due to a higher overall resistance, the cell was cycled at 10 mA/cm^2 with potential cut-offs of 1.6 V and 0.6 V, without any potential holds. Representative cell potential versus capacity curves (a) and efficiencies (b) over 400 consecutive cycles are presented.

A polyBQ/$K_3Fe(CN)_6$ cell was assembled and run at pH 14 (Potassium ferricyanide, $K_3Fe(CN)_6$ was utilized because polyBQ is produced in its reduced form.). The assembled polyBQ/$K_3Fe(CN)_6$ cell was cycled for 400 cycles at 10 mA/cm^2 (Figure 3.17). The CE and EE at 10 mA/cm^2 were 96% and 37%, respectively and remained unchanged over 400 cycles, indicating a stable charge-discharge process. The capacity of the cell is ~25 % of the theoretical capacity, which may be due to the coil-conformation and chain entanglement of polyBQ in solution, as well as the slower kinetics compared with small molecules. In the meantime, the increase in viscosity due to increased molecular size also reduces the contact of redox-active repeating units to the electrodes. During the first 100 cycles, the capacity is slightly variable and increases slightly. During the following 300 cycles, the capacity retention rate was 99.962%/cycle (Figure 3.17a). Compared with the highest

capacity retention rate we acquired for a N115-based DHBQ/$K_4Fe(CN)_6$ cell (99.76% per cycle), the improvement in capacity retention rate supports our hypothesis about the effectiveness of the blocking strategy.

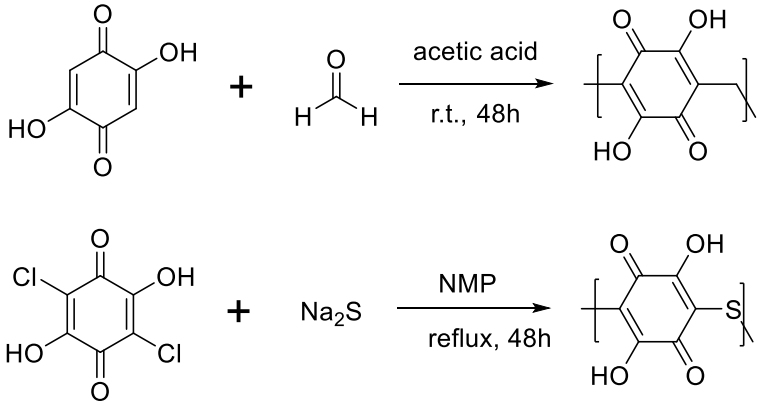

Scheme 3.5. PolyDHBQ with carbon or sulfur linkage

We also devise to link the DHBQ unit with carbon or sulfur linkage. We believe further increase in capacity retention rate can be achieved by incorporating poly(2,5-dihydroxyl-1,4-benzoquinone-3,6-methylene), the polymer from acid-catalyzed condensation of DHBQ with formaldehyde (Scheme 4), as negolyte. Although the reaction was claimed to be readily carried out [59], we have encountered more difficulties than expected in acquiring the polymeric products; more specifically, DHBQ was not soluble in acetic acid as the previous report has claimed. Varying solvent, acid, formaldehyde source, or temperature all led to incorrect product. On the other hand, PolyDHBQ with sulfur linkage was successfully synthesized from dichloroDHBQ and sodium sulfide.[61-62] However, the sulfur linked DHBQ has negligible solubility in alkaline solution, which makes it unsuitable for

aqueous flow battery application. Future research effort will focus on understanding the difference in redox behavior between the monomer and its polymer counterpart. Synthetic efforts will also be devoted to acquiring the most promising substituted DHBQ based on theoretical modelling and evaluating the electrochemical properties.

3.7 Conclusion

Our results indicate that DHBQ-based reactants are promising for alkaline organic RFBs. Compared with anthraquinone-based reactants, benzoquinones have higher alkaline solubility, lower molecular weight, and lower cost. The lower molecular weight, however, causes enhanced membrane permeability and thereby poses challenges for membrane development toward low molecular permeability while maintaining high ionic conductivity, in order to prevent capacity fade due to molecular crossover. Fortunately, many membranes now available seem to be sufficiently stable up to pH 14. 2,5-DHBQ, without further substitution, is not sufficiently stable to provide the service life needed for practical implementation. Our observations support the hypothesis that nucleophilic attack of hydroxide ions on the unsubstituted carbon atoms of the DHBQ aryl ring is responsible for the observed capacity fade. Synthesized derivatives of DHBQ, in which the aryl ring is fully substituted in various ways, substantially altered the capacity retention rate as well as the solubility and redox activity. The insight gained from computational screening, in

conjunction with these experiments, points out avenues for further performance improvement and give us a fighting chance of using benzoquinone-based alkaline organic RFBs to provide safe, cost-effective, robust stationary electrical energy storage.

Chapter 4 Fused Quinone

4.1 Motivation and background

Recent works have explored low-cost electrolytes containing redox-active quinone molecules for aqueous flow batteries. Anthraquinones have been rendered highly soluble in acidic and basic solutions through sulfonation[12] and hydroxylation[11] respectively, and the low redox potentials of certain anthraquinones yield a considerable cell voltage when paired with a high potential redox couple.[11] Quinone-based flow batteries have attracted a great deal of attention for their potential to regulate fluctuations in energy demand and the address the intermittency challenge of renewable wind and photovoltaic supply through cost-effective grid-scale storage.[11-12]

However, as discussed in Chapter 1 (Table 1.1), most of the high performing quinones are low-redox quinones as negolyte. Popular choices for posolytes are still inorganic materials such as bromide[12] and ferrocyanide.[11, 19] Cross-over and toxicity issues from these inorganic-based posolyte diminished the attractiveness of the organic flow battery. Nafion membrane, which can cost up to 1/3 of the material cost,[63] has to be used to minimize cross-over while maintaining low resistivity. On the other hand, there are very limited reports on using quinones, or even organic molecules in general as posolyte. Narayan group from USC has reported[23] using tiron (4,5-Dihydroxy-1,3-benzenedisulfonic acid disodium salt)

as posolyte, but the performance was poor and tiron underwent Michael additional which lowers its stability and reduction potential. TEMPO (2,2,6,6-Tetramethylpiperidine-N-oxyl), a non-quinone radical, has also been employed as posolyte[14, 64], but the poor stability limits its application in long-term grid-scale energy storage. In sharp contrast with the limited quinone selections in aqueous flow battery, quinones are very popular choices as cathode materials in lithium ion battery research to replace metal oxides.[65] Benzoquinone, naphthoquinone, and anthraquinone with different structures and functional groups have all been studied.

The redox center in a quinone molecule is the quinone moiety. C=O double bond was reduced with C-OH single bond together with the aromatization of the benzene ring. It is conceivable that if we install two quinone moieties on a single molecule, two redox centers are available to store and release electrons. This idea is termed fused quinone when two quinone moieties are "fused" together into a single molecule. The advantage is obvious as a single organic molecule can be used as both posolyte and negolyte. Cross-over will not be an issue since both sides are the same, similar to the setup in symmetric cell discuss in Chapter 2. Organic molecules are generally much larger than metal ions, which offers the opportunity to replace the expensive Nafion membrane with other cheaper membranes that have larger pores.

In this chapter, the idea of using fused quinone as both posolyte and negolyte materials for aqueous flow batteries will be discussed. Their limitation and potential application will

be presented.

4.2 Electrochemistry of fused quinones

Fused quinones are two quinones fused together via chemical bonds. Ideally one quinone is the redox center for the low potential part, and the other quinone is the redox center for high potential part.

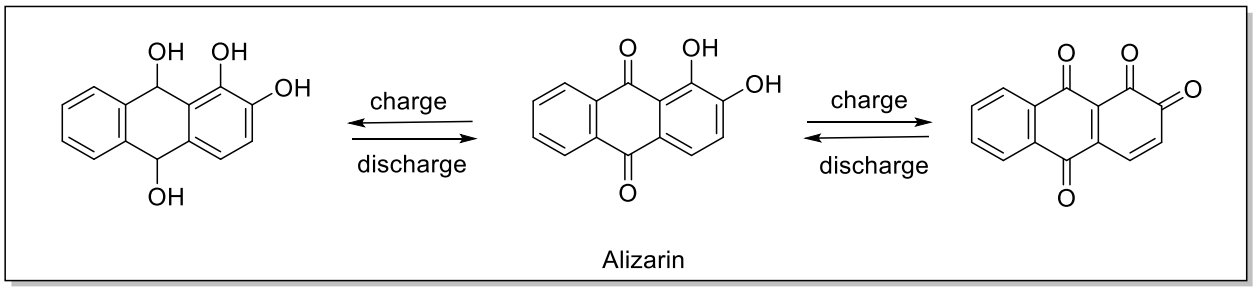

Scheme 4.1. Alizarin as both posolyte and negolyte.

Alizarin family quinones are multi-hydroxylated anthraquinones, and one of the simplest class of fused quinone. Traditionally, multi-hydroxylated quinones were used as negolyte materials in aqueous flow batteries.[11, 20] Only the center quinone moiety was used as redox center, while the hydroxyl groups were used as solubilizing groups or reduction-potential tuning groups. However, when these decorative hydroxyl groups are in ortho- or para- position on a benzene ring, they form a quinone redox center on its own, which makes it a fused quinone with the center quinone moiety. Scheme 4.1 showed charging and

discharge reaction for alizarin (1,2-dihydroxyanthraquinone). For the positive side, the ortho catechol group would be oxidized to be ortho benzoquinone during charge, and the 9,10-benzoquinone would be reduced into 9,10-hydrobenzoquinone in the negative side. During discharging, the reaction is reversed.

Solubilizing fused quinone was simple, and we employed the same strategy as we did for anthraquinone-2,7-disulfonic acid. Starting from cheap, commercially available alizarin, mono-,di-sulfonic acid derivatives can be synthesized by sulfonation with fuming sulfuric acid.

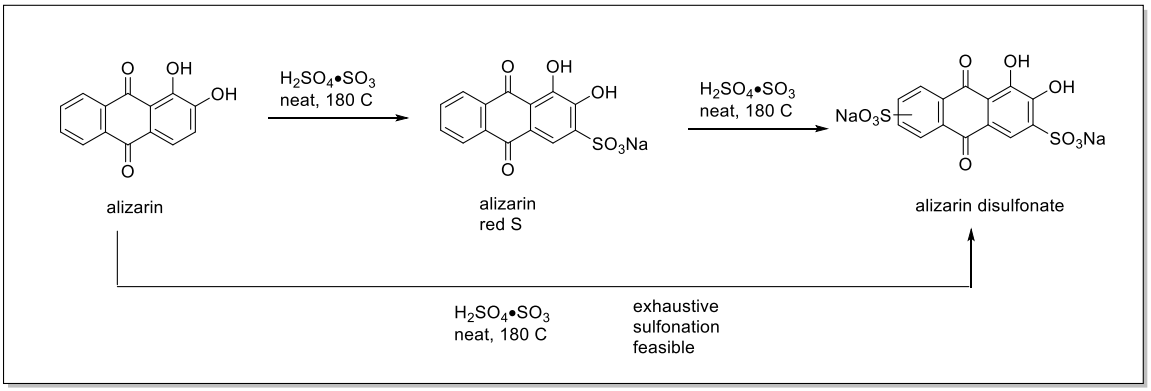

Scheme 4.2. Stepwise and exhaustive sulfonation of alizarin

Several alizarin family quinones were made soluble via this route including alizarin (1,2-dihydroxyanthraquinone), quinizarin (1,4-dihydroxyanthraquinone), purpurin (1,3,4-trihydroxyanthraquinone), and etc. It was worth noting that the alizarin-disulfonic acid has a record solubility exceeding 1.5 M in 1 M sulfuric acid.

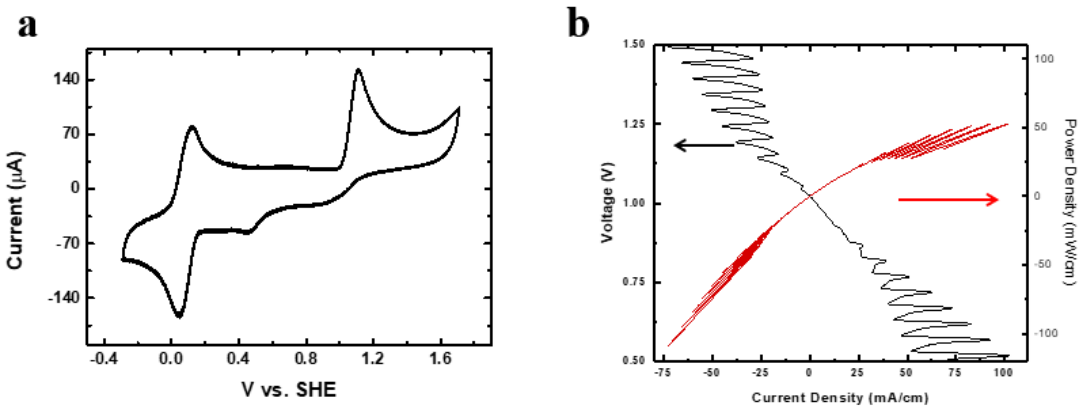

Figure 4.1. a) CV of 5 mM alizarin disulfonic acid in 1M H_2SO_4. Scanning rate is 100 mV/s. **b)** Electrochemical performance of an alizarin disulfonic acid symmetric cell

3-electrode cyclic voltammetry was used to study their solution phase redox behavior. A typical alizarin-disulfonic acid was shown in Figure 4.1a. The low redox pair behaved as expected, but to our surprise, the reduction peak was missing in the high redox pair. Instead, two small and broad peaks at 1.0 V and 0.5 V vs SHE were observed. In addition, the oxidation peak for high redox pair seemed always to be roughly twice the height of the oxidation peak for low redox pair.

Nevertheless, we assembled a symmetric flow battery using 0.1 M alizarin disulfonic acid in pure water on both side of the cell. Pretreated 2 cm^2, stacked (x3) Toray carbon paper electrodes were used on both sides of the cell. Nafion 212 was used as a proton-exchange membrane, and PTFE gasket was used to seal the cell assembly. A chronoamperometry charge and discharge of 1.5 V and 0 V was applied until current reach less than 10 mA. As expected from CV study, an open-circuit potential of 1.02 V was

achieved, and a peak power density of 50 mA/cm^2 was obtained for the first cycle (Figure 4.1b). However, the capacity dropped significantly each cycle and the active materials were nearly all gone after 3 cycles.

The CV curve and electrochemical performance shown in Figure 4.1 was typical for all the sulfonated alizarin family in acidic solutions. NMR analysis of the negolyte run in Figure 4.1. showed an intact starting material, but the posolyte NMR turned to be too messy to interpret. The poor stability of fused quinone as posolyte was the culprit of the poor cycling performance.

The hypothesis for the instability of the high potential quinone was two fold. First, the oxidized tetraketone (bisquinone) species was an excellent Michael 1,4-addition acceptor. Nucleophiles such as water or another alizarin molecule could attack the oxidized species, which turned it into 1,2,3-trihydroxyanthraquinone that could be oxidized again. This hypothesis is consistent with the observation that the oxidation peak in CV for high-redox pair was always twice the size of that for low-redox pair. Second, since the high-redox pair reduction potential was so high (~1.1 V vs SHE), water can add in a 1,2-additon reaction to form the geminal diol, which subsequently started a series of degradation reactions.

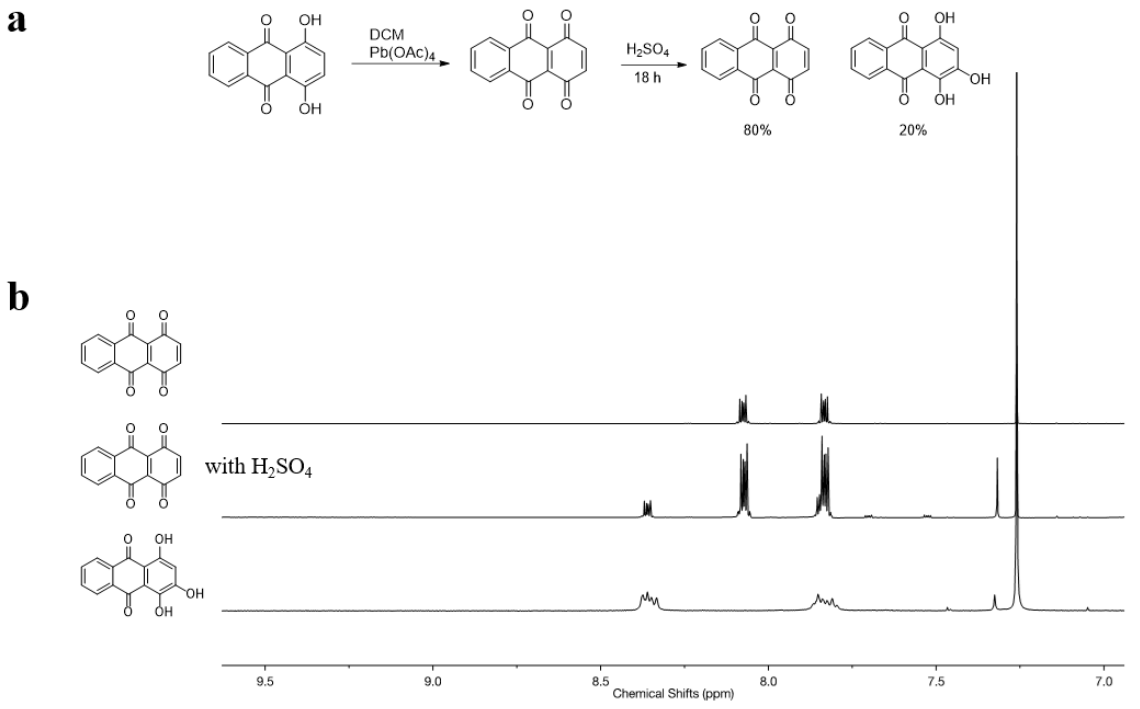

Figure 4.2. a) Synthesis of oxidized quinizarin. **b)** NMR spectra of synthetic oxidized quinizarin(top), quinizarin stirred with sulfuric acid (middle), purpurin standard (bottom).

To probe the first Michael addition product, oxidized form of quinizarin was chemically synthesized according to literature preparation (Figure 4.2a).[66] The fact that the oxidized quinizarin can be synthesized meant that the molecule itself was accessible. However, by stirring in 1 M sulfuric acid, a solvent typically used for flow battery applications, 20 % of the quinizarin was attacked by water and turned into purpurin (Figure 4.2b). It is worth noting that the solubility of oxidized quinizarin in sulfuric acid was very limited, and the above described water attack was a heterogeneous reaction. It is conceivable that in a real flow battery setting when a sulfonated fused quinone is employed, the rate of water attack will be orders of magnitude faster.

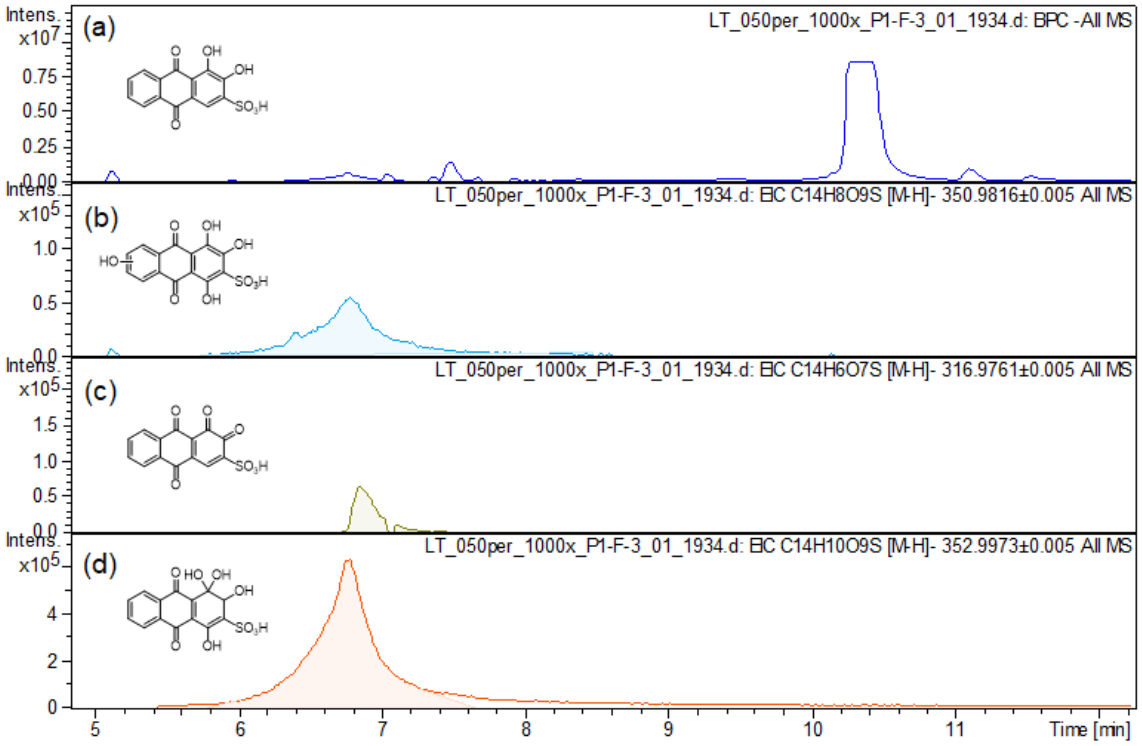

Figure 4.3. high-resolution LC-MS chromatograph of the electrolyte in an alizarin-3-sulfonic acid symmetric battery.

To probe the second gem-diol formation, a high-resolution LC-MS analysis was performed on an alizarin-3-sulfonic acid symmetric battery posolyte at 50 % state-of-charge in the first cycle. The method of LC-MS is the same as described in Chapter 2.

The extracted ion chromatographs from the LC-MS result were shown in Figure 4.3. hydroxylated alizarin was observed by LC-MS (Figure 4.3b), confirming the Michael addition product. A molecular formula of $C_{14}H_{10}O_9S$ $[M-H]^-$, which is one degree of unsaturation less than alizarin starting material. Considering that the posolyte was under oxidative stress rather than in reductive environment in the first cycle, it is no possible for

the molecule to be reduced. The reasonable explanation for this observed decreased degree of unsaturation was a Michael addition followed by a gem-diol formation.

In addition to the m/z shown in Figure 4.4., many smaller fragments from C4 to C10 were also observed, indicating that a series of decomposition product was generated, destroying the alizarin molecule during oxidative stress.

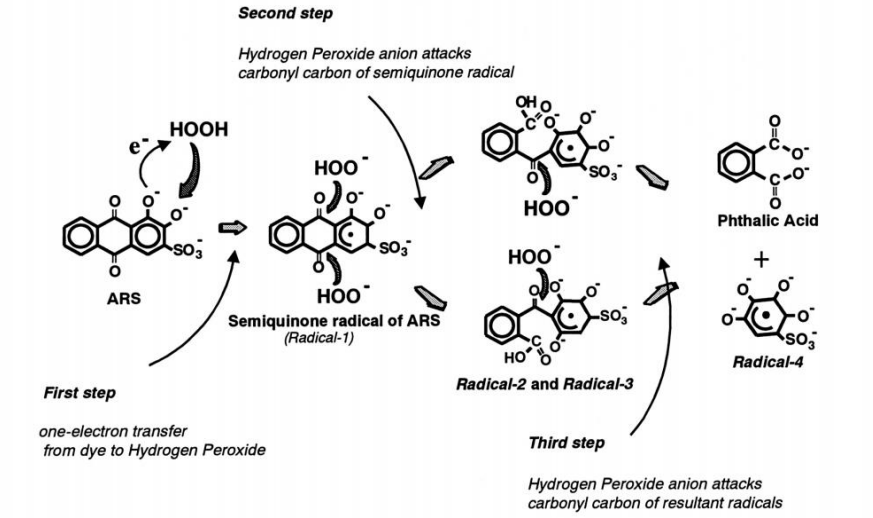

Scheme 4.3. Degradation of alizarin under oxidative stress. (from Ref 67)

However, the fact that the oxidized tetraketone was accessible, and that it does not degrade other than getting hydroxylated meant the decomposition happened during this electrochemical cycling. An old literature report[67] discussed the degradation of alizarin under oxidative stress with hydrogen peroxide in buffered pH=10 solution. A single electron oxidation by hydrogen peroxide induced the radical generation in alizarin. Further attack onto the alizarin radical fragmented the molecule (Scheme 4.3). The analogous reaction can be postulated in an alizarin symmetric cell. When the kinetics of the high-

redox pair of alizarin was sluggish, alizarin radical can be induced by the electrode. This relatively long-lived radical would be attacked by another alizarin molecule to start the fragmentation sequence. This hypothesis is consistent with smaller fragments observed in LC-MS, and consistent with the observation that an increased kinetics aided by high-surface area carbon electrode improves the electrochemical reversibility (discussed in Chapter 4.3, 4.4).

4.3 Adsorbed fused quinone chemistry

During our pursuit of fused quinone in aqueous flow battery, we had a serendipitous discovery. Instead of a regular 3-electrode CV setup using glassy-carbon as working electrode and 10 mM dissolved quinone as electrolyte, an adsorption CV setup was employed (Figure 4.4a). We first dipped the carbon paper in to a high concentration (~0.1 M) quinone solution. During this process, some of the quinones were physio-adsorbed onto the carbon paper. Non-adsorbed quinone was washed off with water and the carbon paper was used directly as working electrode. The CV was then conducted as a normal 3-electrode setup except that the electrolyte solution was pure 1 M sulfuric acid with no quinone added.

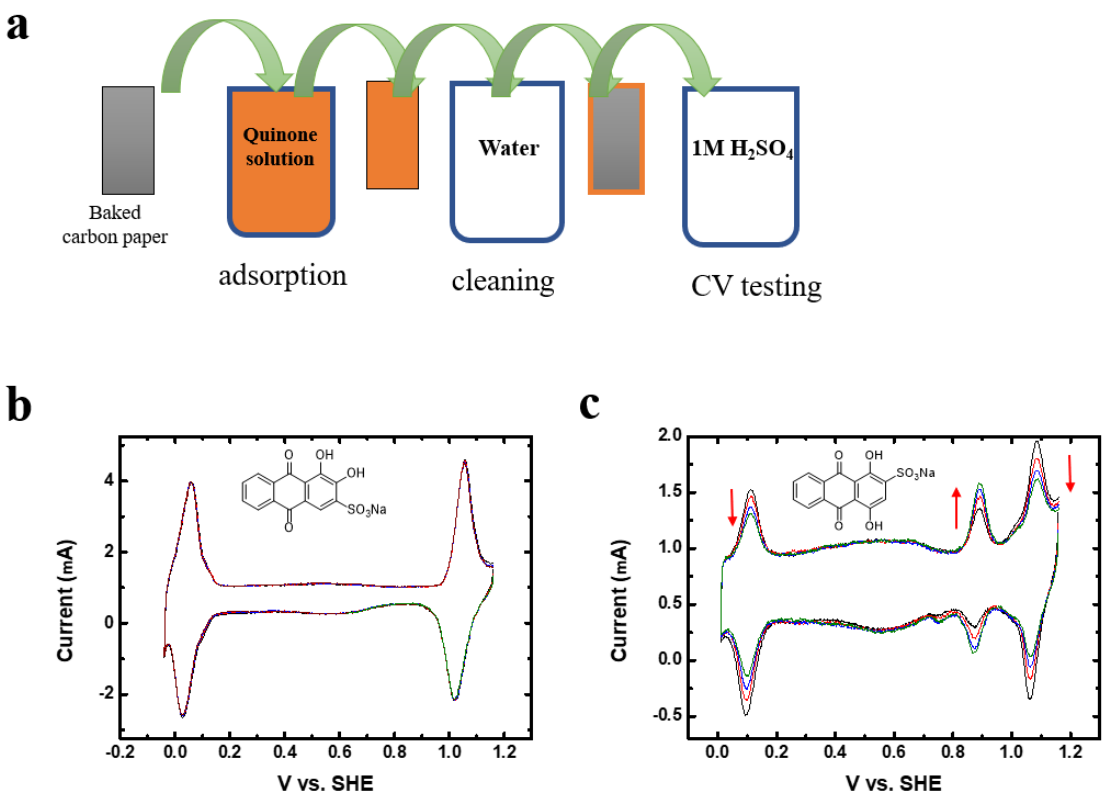

Figure 4.4. a) Schematics of adsorption CV setup. **b**) CV of adsorbed alizarin-3-sulfonate. Overlap of 5scans. Scan rate is 10 mV/s. **c)** CV of adsorbed quinizarin-2-sulfonate. Overlap of 5 scans. Scan rate is 10 mV/s.

It can be seen in Figure 4.4b. that alizarin-3-sulfonate showed a very reversible CV peaks for both low-redox pair and high-redox pair. The peak height of the high-redox pair oxidation curve was now comparable to that of the low-redox pair. A scanning of 5 cycles showed no changes in peak height, demonstrating the improved stability. However, not all members of alizarin family showed a as good stability as alizarin. For example, quinizarin-2-sulfonate (Figure 4.4c) showed a decrease in main peaks but an increase in side peaks (at 0.9 V vs SHE) during 5 CV scans.

The origin of this improved stability was unclear at this point. The hypothesis is 1) The

intimate contact between carbon electrode and alizarin molecule improved the electron transfer kinetics; therefore, no transient reactive intermediate was formed. 2) Since alizarins were immobilized onto carbon paper, even if when transient reactive intermediate was formed, it could not react with another molecule before another electron transfer takes place.

Adsorbed CV on non-sulfonated alizarin was even better because it has very low solubility in sulfuric acid (Figure 4.5a). Based on the good CV result, we assembled a Swagelok-type solid battery with cathode and anode material both being alizarin-adsorbed Sigracet carbon paper. The 0.5 cm-diameter cathode and anode disk were separated by two layers of 0.5 cm-diameter filter paper wetted with 1 M sulfuric acid. The sandwiched cell was compressed with carbon rod as current collector from each side and subjected to galvanostatic electrochemical testing.

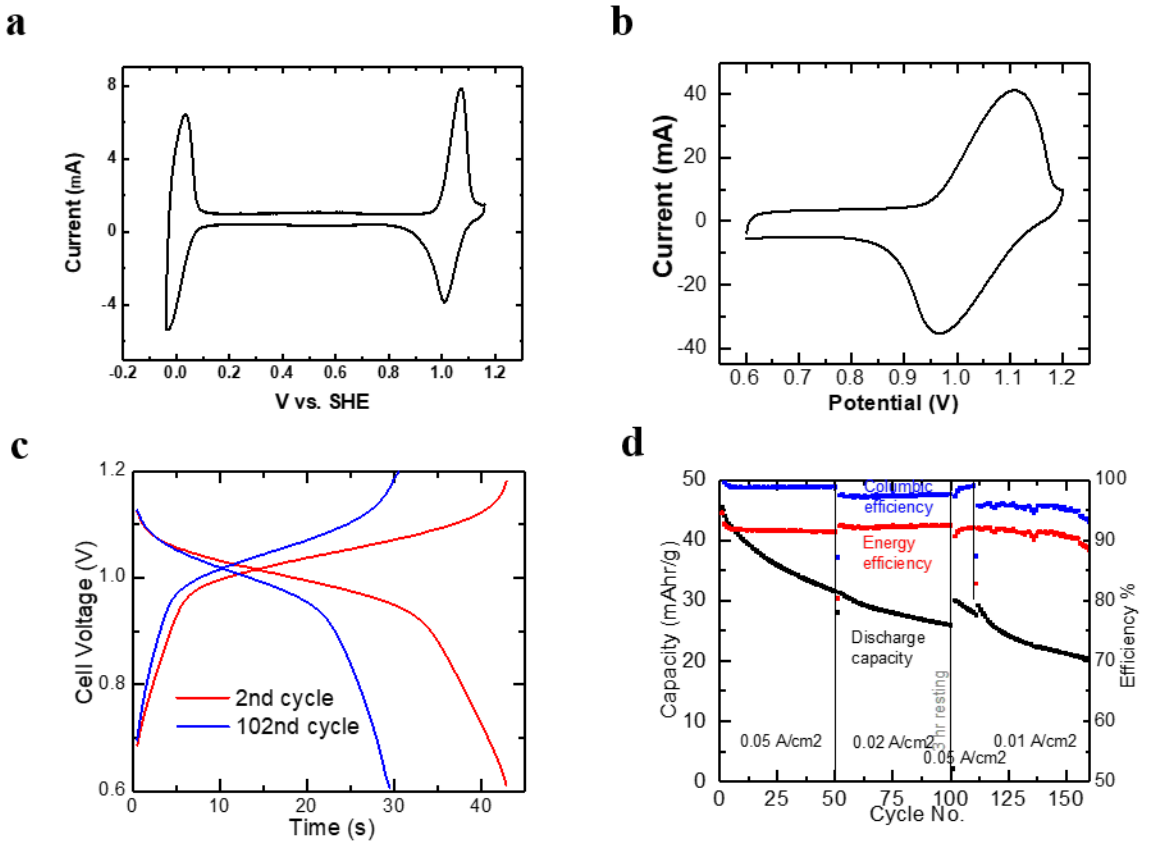

Figure 4.5. a) Half-cell CV of adsorbed alizarin. Scan rate is 10 mV/s. **b**) Swagelok type full-cell CV of adsorbed symmetric alizarin cell. Scan rate is 10 mV/s. **c)** Charging and discharging of full-cell. **d)** Capacity retention and efficiency analysis of full-cell

The CV of the full cell showed an expected OCP of 1.04 V based on the difference between two redox-pairs in half-cell CV. The battery showed clear charging plateau starting at ~0.97 V and discharging plateau starting at ~1.03 V (Figure 4.5c). The battery could be cycled for 180 cycles. The columbic efficiency was higher when cycled at a fast rate (Figure 4.5d), which indicated a competing side reaction when alizarin was charged and contributed to the gradual capacity loss. Part of the capacity loss was also due to a dissolution of the active materials from the carbon paper. When the cell was dissembled,

we observed that the separator was stained yellow by alizarin.

4.4 Solid fused quinone battery

Chapter 4.3 demonstrated that the idea of fused quinone can be used in an adsorbed setting. However, the active material loading was poor because it was relying on physical adsorption. In order for a fused quinone to be truly useful in batteries, active material loading much be improved.

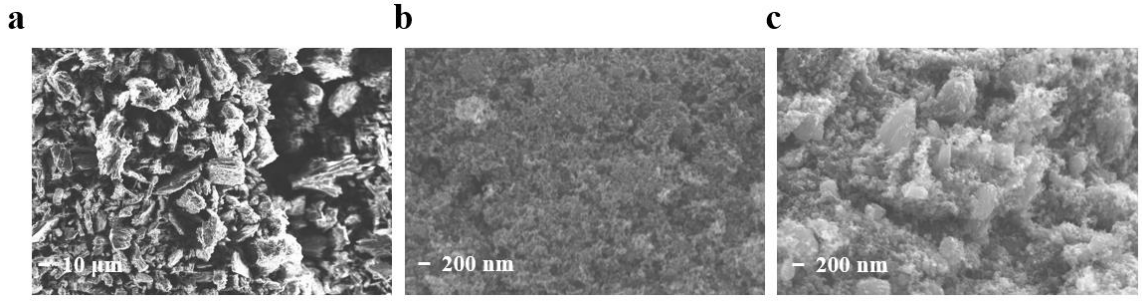

Figure 4.6. SEM image of a) Alizarin powder, b) Ketjen Black powder, c) Ball-milled 3:7 alizarin:KB powder

Fortunately, there are a vast number of literatures[28, 65] on loading quinones onto carbon electrode. However, the pellet made from initial mixing of alizarin and Ketjen Black (KB) carbon powder did not reproduce the reversible CV curve for the high-redox pair. We hypothesized that it was due to uneven mixing of alizarin and KB. When alizarin was still

in its large crystal form, the overall electroconductivity was bad and the kinetics was sluggish. Therefore, in order to create an intimate mixture of alizarin and KB, we ball-milled 30 % w/w alizarin with 70 % KB together using a Retsch PM 100 planetary ball mill instrument for 2 hours at 200 RPM using 10 5-gram stainless steel balls, and another 2 hours at 400 RPM using 100 0.5-gram stainless steel balls. The alizarin powder obtained directly from manufacturers were 10 μm in sizes. After ball milling, the alizarin was reduced to 200 nm in sizes and intimately mixed with KB.

Polytetrafluoroethylene (PFTE) water suspension was added as binder to the ball-milled alizarin-KB powder to make an overall 3:7:1 alizarin:KB:PTFE film after drying. The thickness of the film was about 1 mm.

We assembled the Swagelok-type full cell using the film of 1 mg on each side as both cathode and anode material separated by 2 layers of filter paper wetted with 1 M sulfuric acid. The full cell CV (Figure 4.7a) demonstrated a reversible peak with OCV of 1.04 V, as expected from previous results. This showed the importance of ball-milling in improving the kinetics of alizarin cycling.

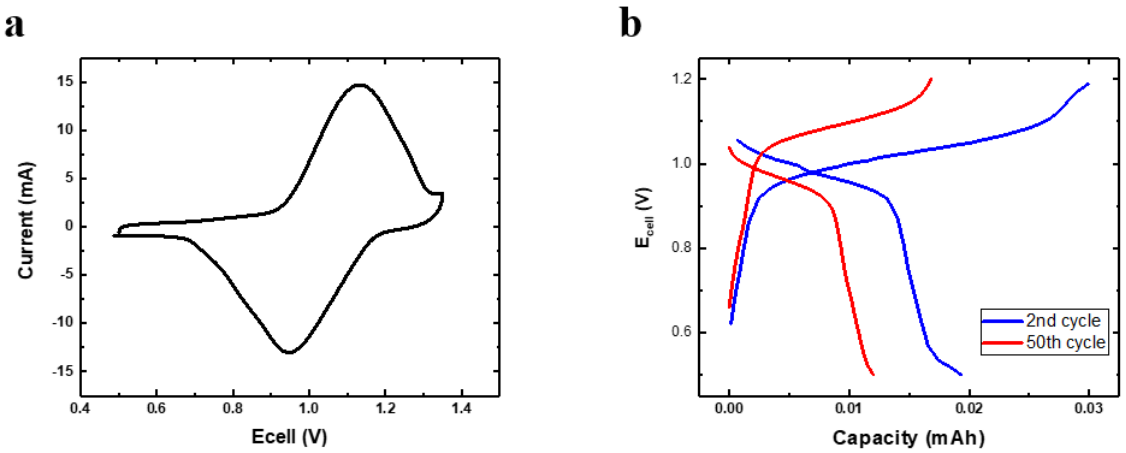

Figure 4.7. a) Full-cell CV of solid fused quinone battery. The scan rate is 10 mV/s. b) Charging and discharging of full-cell. The cycling rate is 10C.

We then cycled the battery at 10 C of theoretical capacity, a very fast charging and discharging rate for aqueous solid batteries. Each half cycle in theory takes 6 min if all capacity could be assessed. Similar to the adsorbed cell cycling (Figure 4.6c), the battery showed a clear charging and discharging plateau. 30 % of the capacity was assessed in the first cycle, and 40 % was assessed capacity was lost after 50 cycles.

This proof-of-concept study demonstrated the idea of using fused quinone in all-organic, symmetric, aqueous solid batteries. The increased loading from adsorption to 30 % w/w demonstrated the potential for developing into a commercial battery. Current efforts are on optimizing many of the parameters such as ball-milling recipe, loading ratio, charging rate, binder, and additives. It is also conceivable that a semi-solid redox-flow battery can be constructed from this idea of fused quinone, which would be useful for grid scale energy storage.

Chapter 5 Synthesis of Volatile, Thermally Stable, and Reactive Coinage Metal 5,5-Bicyclic Amidinates for Chemical Vapor Deposition

Part of this chapter was published in my co-authored paper and in prepared manuscript that will be submitted soon.[68] Some details that were published were omitted in this chapter.

5.1 Abstract

We describe the first syntheses of aliphatic 5,5-bicyclic amidines. The syntheses are facile and scalable, and can be easily modified to produce other 5,5-bicyclic amidine ligands with other substitution patterns. We have synthesized and characterized a copper(I), silver(I) amidinate and a gold(I) bicyclic amidinate as chemical vapor deposition (CVD) precursors. The syntheses process by a simple one step reaction of the amidinate ligand and copper(I), silver (I) and gold(I) source. The synthesis completes the coinage series based on aliphatic bicyclic amidine as stable CVD precursors. X-ray crystallography revealed that the copper(I) and gold(I) compound adopted the symmetrical dimeric structure analogous to the copper(I) compound, while the silver(I) compound adopted a tetrameric structure. The compounds are stable in air and light, and thermal gravimetric analysis (TGA) showed good thermal stability up to 250 °C. Gold and silver metallic films were obtained

by CVD with hydrogen as reductant at low temperature (<220 °C). The films showed little to none carbon content and excellent conductivity.

Together, the ligands enable a general method for producing a library of thermally stable metal amidinate precursors with a wide variety of metals for use in vapor deposition.

5.2 Introduction

Chemical Vapor Deposition (CVD) and Atomic Layer Deposition (ALD) are vapor deposition processes that are capable of depositing highly conformal thin films while affording a great degree of control over film thickness.[69-72] They have found many applications in areas such as microelectronic devices, machine tools and window coatings.[73] The precursors must possess high volatility, high thermal stability, high reactivity with other precursors, with volatile and non-corrosive reaction byproducts.[74]

Gold and silver metal films have important applications in industry. Gold is extensively used in microelectronics industry due to its low resistivity and inertness to chemical and electrochemical corrosion. For example, gold was used as metal interconnects to enhance reliability and performance for GaAs-based semiconductors[75], to repair defects in thin-film circuits.[76] Silver is the most conductive metals (1.59 μΩcm) and was used in many microelectronics. For example, it has been used as good material for forming low-resistivity contacts with superconducting ceramic materials.[77]

Despite that copper has a wide selection of CVD precursors,[78-85] the CVD industry is falling behind in its selection of gold and silver CVD precursors. Metal amidinates, as exemplified by *N*,*N*'-diisopropylacet-amidinatocopper(I), have been a popular choice as a precursor for the vapor deposition of films containing transition metals or rare-earth metals.[81, 86-89] However, they can decompose at elevated temperatures, which may limit their usefulness as precursor ligands when a higher deposition temperature is desired. In addition, rarely have all three coinage metal precursors been prepared using the same ligands. Silver and gold amidinates are difficult to make and decompose easily in the useful temperature range,[82] and are usually extremely sensitive to oxygen, water, and light, which severely limit their application in CVD

It has been hypothesized that such thermal decomposition takes place *via* a β-hydride migration from one of the ligand side chains to the metal center, followed by M–N bond cleavage. DFT calculations on the mechanism and the transition state through which this takes place revealed that in the transition state, the transferred H atom, the metal atom and the N–C–N functional group of the ligand all lie in the same plane.[90-91]

Barry *et al*. have come partway to solving the problem with their careful study of tert-butylimino-2,2-dimethylpyrrolidine as the ligand.[92] A copper(I) complex with this ligand, which can be thought of as a monocyclic amidine, showed improved thermal stability compared to *N'*,*N''*-diisopropyl-*N*-dimethyl-guanidinatocopper(I). However, this

monocyclic amidine still has one exocyclic alkyl group that could potentially undergo β-methyl migration to the metal.

As a result, we propose to make a fully β-substituted 5,5-bicyclic amidine ligand (Scheme 5.1), in which the H atom cannot reach the planar transition state without twisting the ring system into a much higher energy state. Thus the β-hydride (or β-methyl) migration to the metal is expected to be much slower in a metal bicyclic amidinate than in the corresponding acyclic amidinate.

5.3 Ligand synthesis

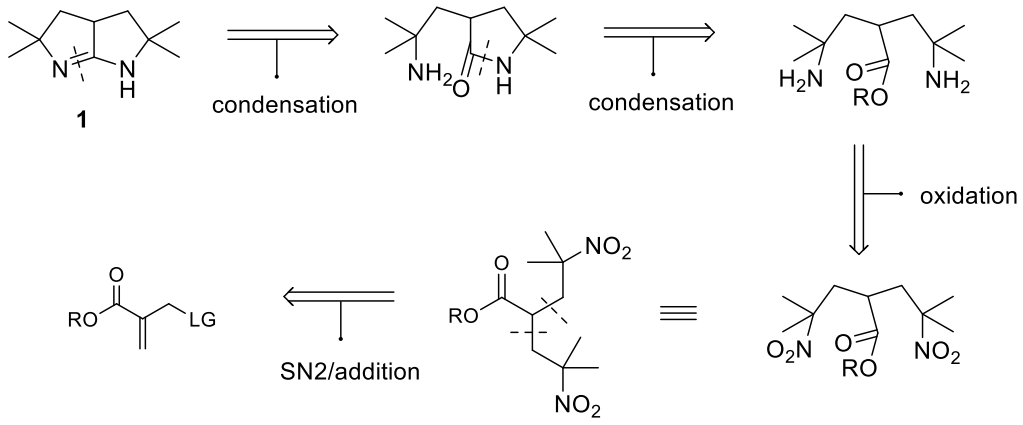

Scheme 5.1. Retrosynthetic analysis of 5,5-bicyclic amidine ligand.

Retrosynthetic analysis indicates breaking the amidine bond to yield the free amine and amide, which will condense in catalyzed condition. Further breaking the amide yields a symmetric diamine which can be synthesized from 2-nitropropane as a nucleophile attacking onto two leaving groups or 1,4-addition onto a α,β-unsaturated ester. Such

synthetic plan takes advantage of the inherent symmetry from **1**, and the success depends on the final condensation reactions to generate amidine.

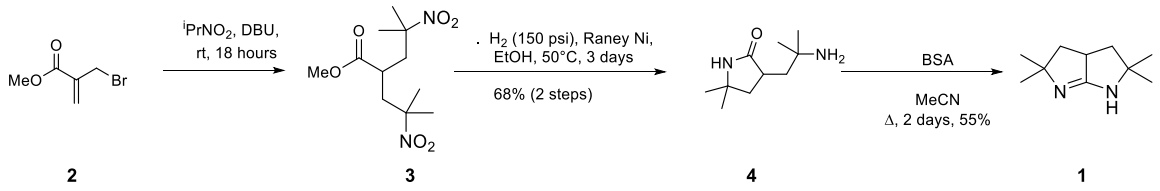

Scheme 5.2. Synthetic routes to 5,5-bicyclic amidines.

After screenings of suitable starting materials, we employed ethyl 2-(bromomethyl)acrylate **2** as a Michael acceptor with a leaving group. The synthesis commences with deprotonation of 2-nitroprone by 1,8-Diazabicyclo(5.4.0)undec-7-ene (DBU) and subsequent addition-substitution onto **1** to form the symmetrical dinitro-ester **3**. Raney Ni turned out to be the most effective catalyst for the reduction of the dinitro-ester into diamino-ester intermediate, which self-condensed into amino-cyclicamide **4**. The final condensation was challenging as it required a free amino group condensing onto a relatively stable cyclic amid. Several methods were unsuccessfully attempted: refluxing in toluene with catalytic TsOH under a Dean-Stark trap,[93] as was BOP.[94] After some experimentation, *N*,*O*-bis(trimethyl-silyl)acetamide (BSA) was found to react cleanly to give the product amidines.[95] It should be noted that the addition of BSA had to be very slow and reaction progress need to be constantly monitored by NMR to avoid over addition of BSA, or else the intermediate will be double trimethylsilylated into an unreactive side

product (Scheme 5.3).

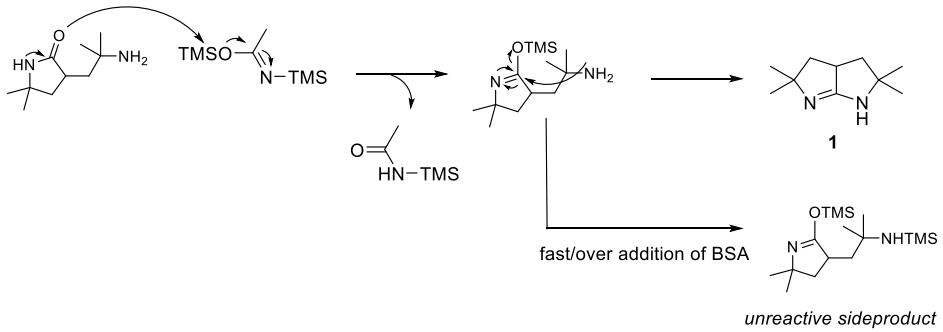

Scheme 5.3. Mechanisms of cyclization by BSA.

5.4 Precursor synthesis

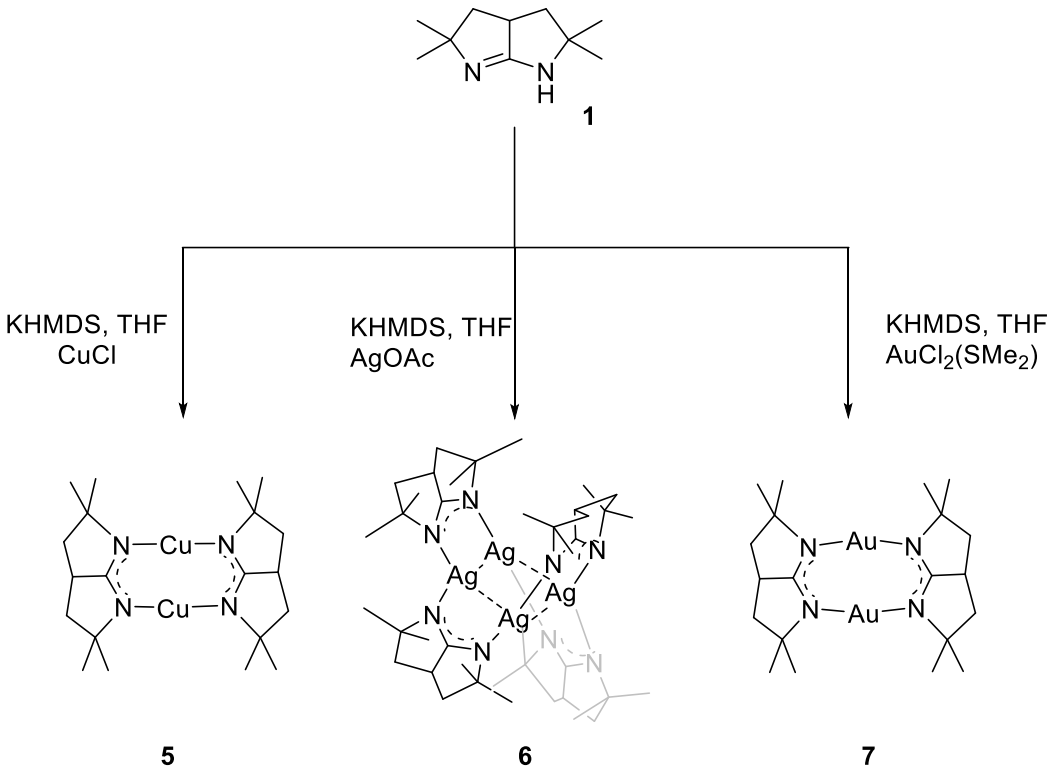

Scheme 5.4. Synthesis of bicyclic amidinate Cu(I), Ag(I) and Au(I) compounds

5.4.1 Bicyclic amidinate Cu(I) synthesis

Treatment of a solution of **1** in THF with KHMDS, followed by transmetalation with CuCl, gave **5,** a Cu(I) complex of **1**. **5** was isolated in 55% yield as white crystals after recrystallization from pentane. **1** is an air-stable compound that do not decompose for several weeks in air.

X-ray crystallography of copper complex **5** was conducted by Dr. Jun-Jieh Wang and Dr. Shao-Liang Zheng, and it showed that Cu(I) I complex exist as dimer form (Figure 5.1) with C_{2h} symmetry. However, the doublet in ^{1}H NMR (Figure 5.2) suggested the existence of another C_{2v} symmetric dimmer at equal amount in the product.

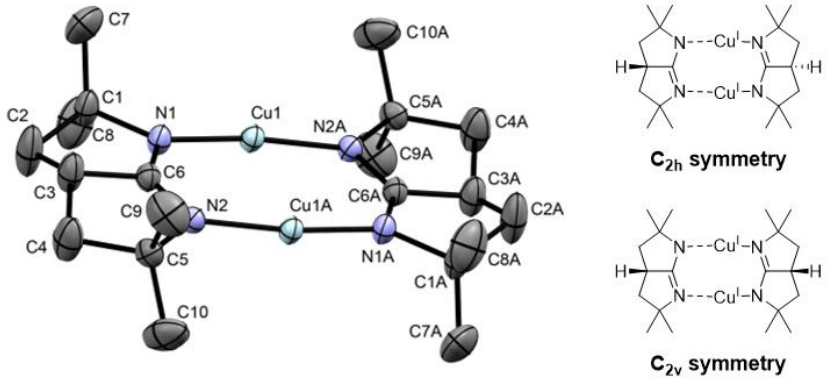

Figure 5.1. X-ray crystal structure of **5**, showing 50% probability ellipsoids and partial atom-labeling schemes

To order to study the thermal stability of **5**, Dr. Eugene Beh dissolved **5** in deuterated mesitylene in a sealed heavy wall NMR tube. The degradation of NMR signal with respect to internal standard was monitored. The same experiment was also conducted for

N,*N*'-diisopropylacet-amidinatocopper(I), an analogous non-cyclic homoleptic dimeric Cu(I) CVD precursor for comparison. The bicyclic precursor **5** was found to decompose an order of magnitude more slowly than acyclic counterpart at 200°C. Assuming that the decompositions both obey first-order kinetics, the decomposition rates are 4.2×10^{-7} s^{-1} and 4.1×10^{-8} s^{-1} respectively, corresponding to respective solution half-lives of 19 days and 200 days. This dramatically enhanced thermal stability was attributed to **5** having a rigid 5,5-bicyclic framework and no β-hydrogen for any possible β-hydrogen or β-methyl decomposition mechanism.[90-91]

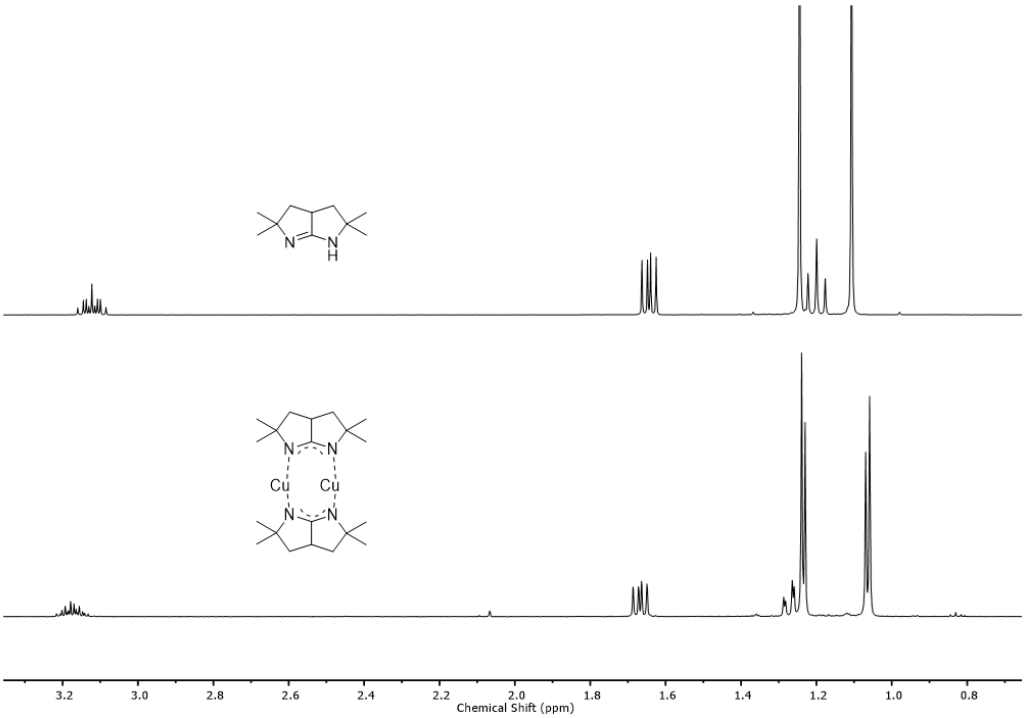

Figure 5.2. ^{1}H NMR of starting material (top) and Cu(I) complex **5**. Doublet was observed in **5**

During the synthesis of copper complex, we found out an interesting phenomenon. Despite that the Cu(I) complex was stable in air and moisture, the MS detection of the compound dissolved in benzene/MeCN showed a m/z ratio of 167 and 395, which corresponded to the free ligand and mono-demetalated **5**, and no parental ion (m/z = 457) was observed (Figure 5.3.). This showed that these metal complex seemed to be labile in MS condition, but it also provide a fast and crude way are determining the success of the synthesis, which proves to be very convenient in the silver and gold precursor synthesis later.

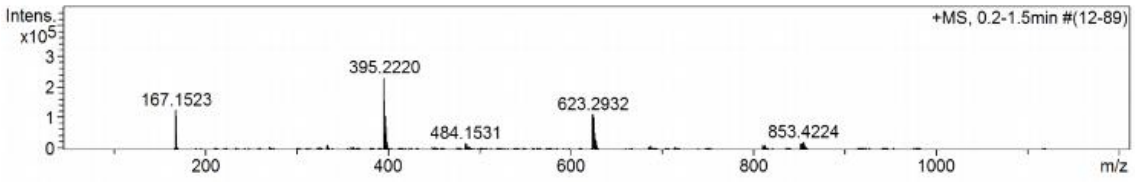

Figure 5.3. Mass-spectrometry data showed the existence of free ligand (m/z = 167), and mono-demetalated **5** (m/z = 395).

5.4.2 Bicyclic amidinate Au(I) synthesis

The synthesis of Au(I) complex is analogous to the synthesis of Cu(I) complex **5**. However, despite that AuCl as the gold source will give the correct product by NMR and MS, the reaction was quite peculiar as AuCl was not very stable, and yield was not very reproducible. Instead, a stabilized and soluble gold source, $AuCl(SMe_2)$ was used. $AuCl(SMe_2)$ is a white powder that can be easily synthesized one step from the reduction

of HAuCl4 by SMe_2 and used without further purification.[96] Treatment of a solution of **1** in THF with KHMDS, followed by transmetalation with $AuCl(SMe_2)$ gave **7,** a Au(I) complex of **1**. During the reaction, the suspension turned pink to purple, indicating the formation of Au^0 nanoparticles. Filtration of the purple suspension through Celite gave a clear solution, which upon concentration *in vacuo* afford a white solid. Washing with pentane afforded **7** in 60 % yield in sufficient purity as analyzed by NMR. Further purification can be achieved by sublimation at 170 °C at 30 mTorr. The solubility of **7** was very poor in THF; therefore, a large quantify of THF was needed to ensure all product was dissolved and can pass through Celite.

It was worth noting that **7** was a particularly air-stable compound that do not decompose for several weeks in air, in fact, the above synthesis was carried out in the hood rather than in glove box.

The ^1H NMR spectrum of **7** in C_6D_6 was very similar the copper complex. The methylene and methine protons were slightly shifted to the left as compared to free ligand **1**. The doublets also indicated the existence of two diastereomers with C_{2v} and C_{2h} symmetry.

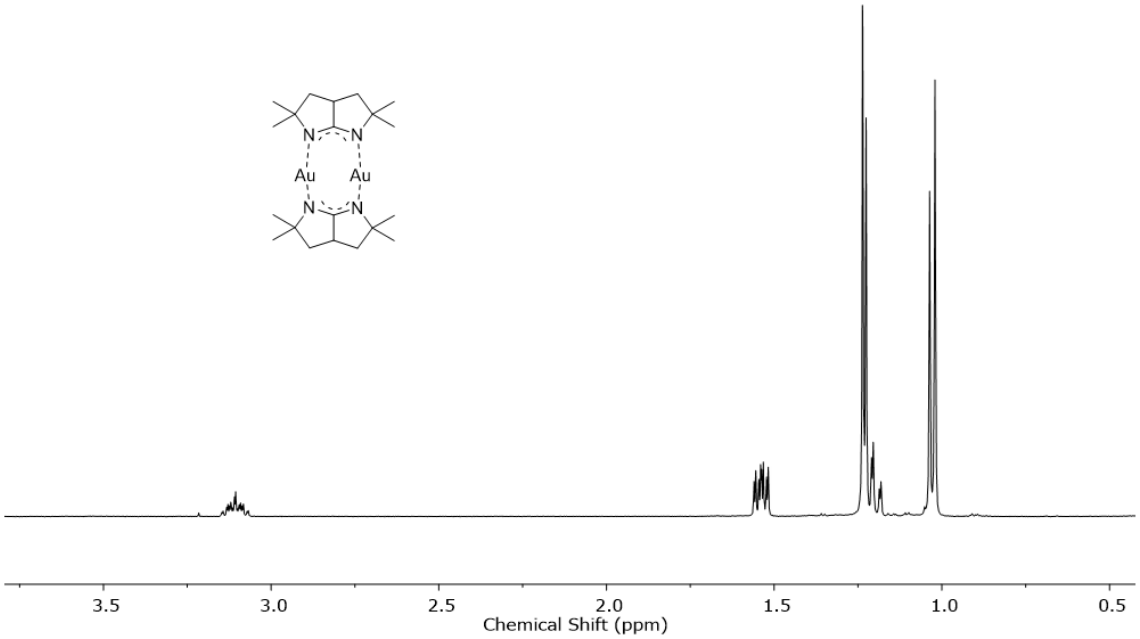

Figure 5.4. NMR spectrum of **7**. The doublets indicated the existence of two diastereomers

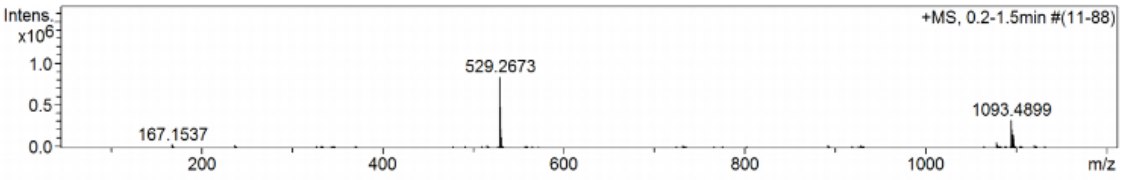

Figure 5.5. Mass-spectrometry data showed the existence of free ligand (m/z = 167), and mono-demetalated **7** (m/z = 529).

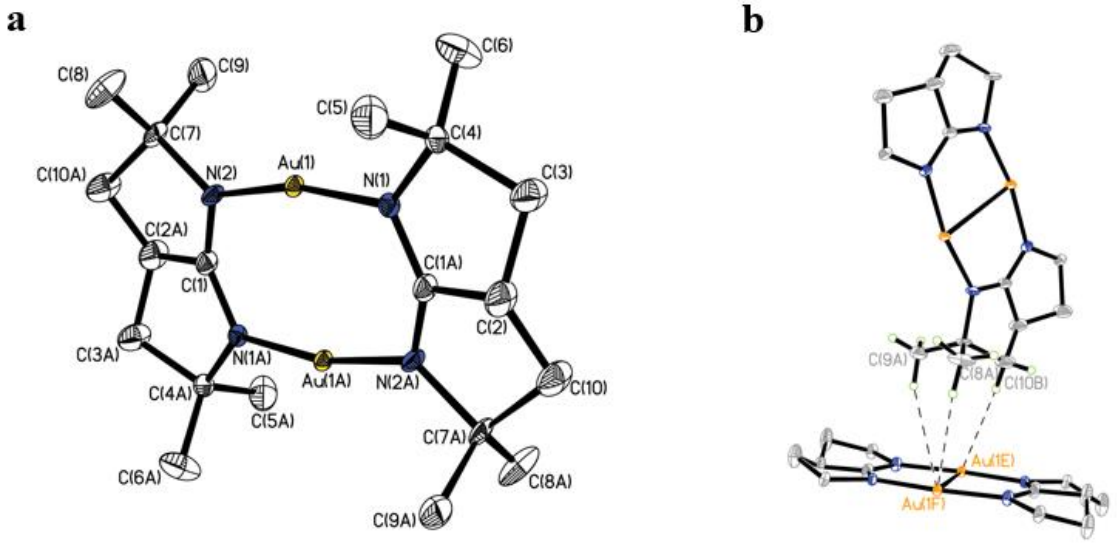

Figure 5.6. a) X-ray crystal structure of **7**, showing 50% probability ellipsoids and partial atom-labeling schemes. **b**) interactions between two neighboring molecules. Hydrogen atoms and some methyl groups were omitted for clarity

Table 5.1. Selected bond length and angle in Figure 5.6b.

Au	C	d(H), Å	d(C), Å	∡, °
1E	10B	2.932	3.909	177.4
1F	8A	2.967	3.895	174.7
1F	9A	3.201	4.073	172.9

X-ray quality crystals were grown from of slow evaporation of a dichloromethane solution of **7**.

Dr. Luke M. Davis performed X-ray crystallography of **7**. As expected, the gold complex existed in the same dimer form as the copper complex **5** (Figure 5.6) Interestingly, in solid state, the neighboring molecule was almost perpendicular to this molecule. The Au-H distance was around 3 Å, Au-C distance was around 4 Å, and the Au-

H-C angle was near linear (Table 5.1). This implied a weak hydrogen bonding interaction between two molecules. A review of gold···H-C interactions described as hydrogen bonding interactions for Au(I)···H-C interactions with distances Au···H < 3 Å and Au···C < 4 Å, preferably with Au···H-C approaching 180 ° .[97] This hydrogen bonding characteristics in the Au(I) bicyclic amidinate probably attributed to its surprising stability in air.

5.4.3 Bicyclic amidinate Ag(I) synthesis

Synthesis of silver compound was more complicated than gold and copper counterparts. Despite that previous efforts usually used AgCl as silver source to synthesize silver amidinate compound[82, 98], the reactions with **1** was always incomplete even after several days of stirring due to extremely low solubility of AgCl in organic solvent. In addition, black suspension was usually formed either by the reducing nature of the amidinate ligand, or a slight excess of KHMDS or *n*-Buli.

After careful screening, AgOAc was selected as the Ag(I) source as it has high solubility in organic solvents. The reaction speed was dramatically increased and typically completed within 5 hours.

Treatment of a solution of **1** in diethyl ether with KHMDS, followed by transmetalation

with AgOAc gave **6,** a Ag(I) complex of **1**. During the reaction, the suspension turned grey to black, indicating the formation of Ag^0 nanoparticles. Filtration of the black suspension through Celite gave a clear brown solution, which upon concentration *in vacuo* afford a pale-grey solid. Excess amount of pentene was used to wash the solid to afford **6** as white solids in 45% yield. It was worth noting that the **6** was a particularly air-stable compound that do not decompose for several weeks in air, in fact, the above synthesis was carried out in the hood rather than in glove box.

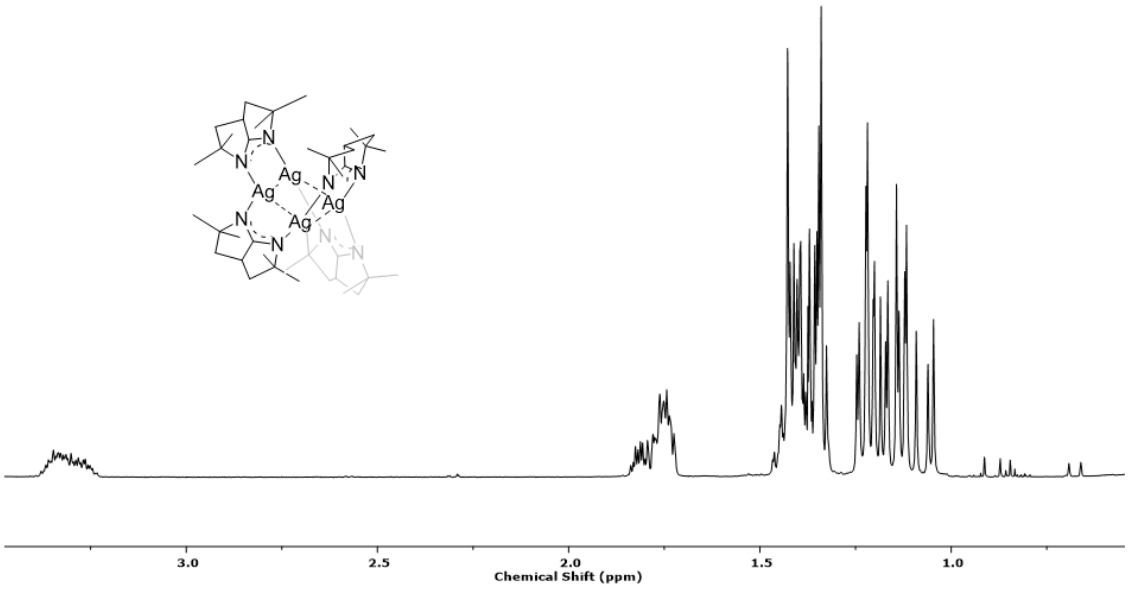

Figure 5.7. NMR spectrum of **6**

Interestingly, the NMR spectrum of the above product was very messy, and very

different from Cu(I) and Au(I) complex. Sublimation at 160 °C at 30 mTorr did not make the spectrum any better. In order to elucidate the structure, X-ray quality crystals were grown from hot dichloromethane solution of **6**.

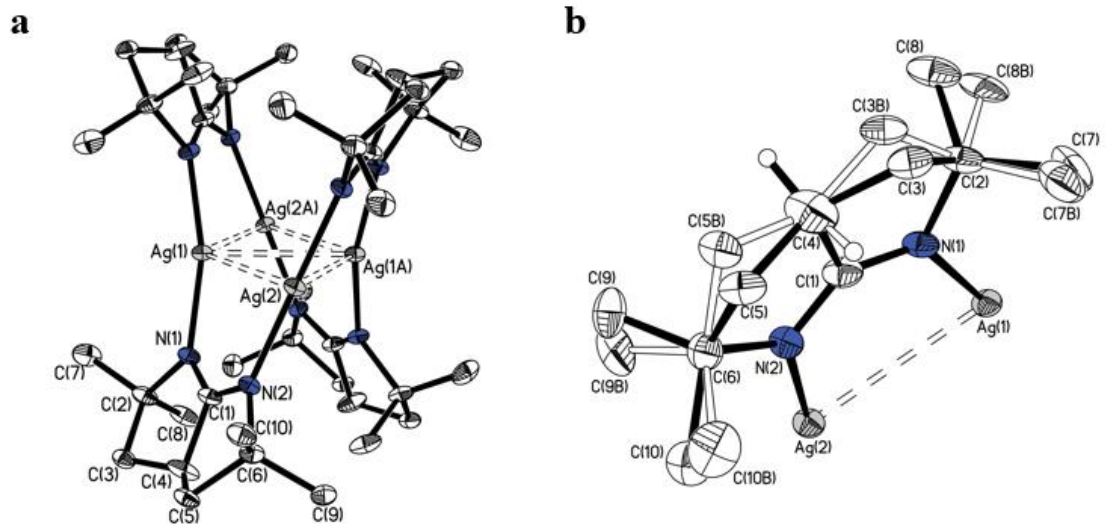

Figure 5.8. a) X-ray crystal structure of **6,** showing 35% probability ellipsoids and partial atom-labeling schemes. **b)** two conformations, black stick and white stick, exist in the ligand

Dr. Luke M. Davis performed X-ray crystallography on **6**. Surprisingly, the structure of **6** was confirmed to be tetrameric (Figure 5.8a). In addition, there about 1/4 of the ligands (Figure 5.8b, white stick) have the opposite conformations as the rest (Figure 5.8b, black stick), adding more complexity to the overall structure. This tetrameric structure and conformation in the ligands attributed to the complicated NMR observed. There were many reports are dimeric, trimeric or polymeric silver clusters, but reports on tetrameric organometallic silver compound were limited.[99]

5.5 Properties of coinage metal 5,5-bicyclic amidinate

In order to study the thermal stability and evaporation rate of these three amidinate compound. Ramped thermal gravitational analysis (TGA) and stepped isothermal was performed on a TGO Q50 (TA Instruments, Inc.) under 1 atm of N_2. For ramped TGA, about 10 mg of each sample was placed on an alumina pan, and the heated at a linear temperature ramp of 10 °C /min. Figure 5.9a showed the TGA curve of three samples. Copper amidinate **5** sublimed cleanly starting at a temperature of ~170 °C and completing at ~290 °C, with 50 % mass loss at 270 °C and <0.2% of residue. A previously reported TGA of an acyclic compound, *N'*,*N''*-diisopropyl-*N*-dimethyl-guanidinatocopper(I), under identical conditions[82] also showed clean sublimation beginning at ~150 °C and completing at ~260 °C. As such, the volatility of cyclic amidinate **5** is slightly lower than that of the acyclic one, with a which is to be expected because of its higher molecular weight (457.61 g/mol *vs*. 409.57 g/mol).

However, TGA curve showed that the gold compound **7** had two weight loss curve overlapping each other, with the second curve starting at around 310 °C. After heating to 500 °C, the compound showed a ~25 % residual, which presumably was the gold film decomposed from the precursor. The 50 % mass sublimation point was at ~ 310 °C, about

40 °C higher than copper compound **5** which had the 50 % mass loss point at 270 °C. Such trend was expected as the gold compound was much heavier than copper compound (724.45 g/mol *vs*. 457.61 g/mol)

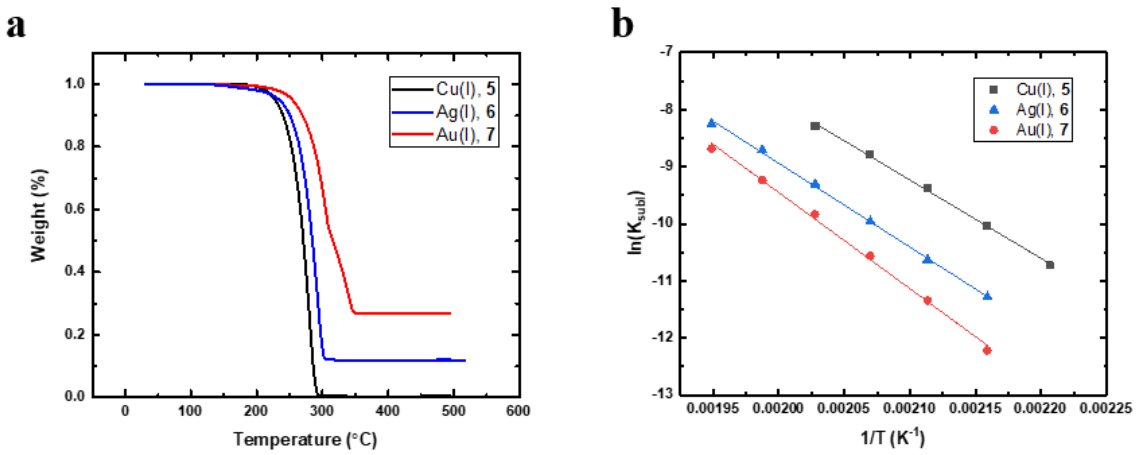

Figure 5.9. a) Ramped TGA of Cu(I), Ag(I), and Au(I) complex. Linear ramp of 10 °C/min was used. **b)** Arrhenius plot of stepped-isothermal TGA. Each temperature was held for 11 min.

More surprising was the TGA of tetrameric silver(I) compound **6**. Despite that X-ray analysis showed that silver compound existed as a tetramer, the silver compound had a 50 % mass loss temperature at 290 °C, between that of Cu(I) and Au(I) compound. This 50 % mass loss temperature would only mass sense if the silver was actually dimeric, rather than the heavy tetrameric complex. It is hypothesized that the tetrameric Ag(I) compound may rearrange to dimeric Ag(I) upon heating.

In order to be used as a CVD precursor, the amidinate compounds need to cleanly

sublime at the temperature of sublimation in the bubbler. The complicated ramped TGA curve made it difficult to judge whether there would be a sublimation-only region for this compound. Therefore, we conducted stepped-isothermal TGA. The temperature was raised at a constant rate of 10 °C/min until 180 °C was reached, then maintained at 180 °C for 11 minutes. Following that, the temperature was raised successively to 240 °C in 10 °C increments at a rate of 10 °C/min. The temperature was maintained for 11 minutes at each step. The curves were plotted according to Arrhenius equation:

$$\ln(K) = lnA - \frac{E_a}{RT}$$

Plotting of ln(rate of sublimation) vs the reciprocal of temperature in Kelvin should give a linear curve, and the slope of the curve was $-E_a/R$. It is quite evident from Figure 5.9b that all three compounds had a linear sublimation region below 240 °C. The slope of Cu(I) **5** is -13731, which corresponds to an enthalpy of sublimation of 109 kJ/mol. The slope of Ag(I) **6** is -14692, which corresponds to an enthalpy of sublimation of 122 kJ/mol. The slope of Cu(I) **7** is -16843, which corresponds to an enthalpy of sublimation of 140 kJ/mol.

This completed the synthesis of the 5,5-bicyclic amidinate series of coinage metal. They all displayed exceptional stability towards air and moisture and improved thermal stability owning to the restricted bicyclic frame and a lack a β-hydrogen for side reactions. They all displayed a linear sublimation region under 240 °C suitable for CVD applications.

5.6 CVD deposition of metallic silver and gold films

To investigate the volatility and reactivity of Ag/Au precursor, both silver and gold metal films were deposited by our home-made CVD system by using the vapor of precursors and H_2 (collaboration with Xian Gong and Dr. Jun Feng). The schematic diagram of the CVD system is shown in Figure 5.10. During the deposition process, the vaporized precursor was carried with a constant flow of 100 sccm N_2 flow. Then the precursor vapor was mixed with purified hydrogen (H2) and then delivered into a preheated reaction chamber (16 in. long and 1.25 in. diameter) with an 11 in. × 1.25 in. semicylindrical sample holder inside. The total pressure in the chamber is controlled and maintained at 5 torr. The temperature of the precursor was maintained at various values from 160-180 for both silver and gold deposition. The substrate temperature was hold constant at 200℃ and 220℃ for Ag and Au deposition, respectively.

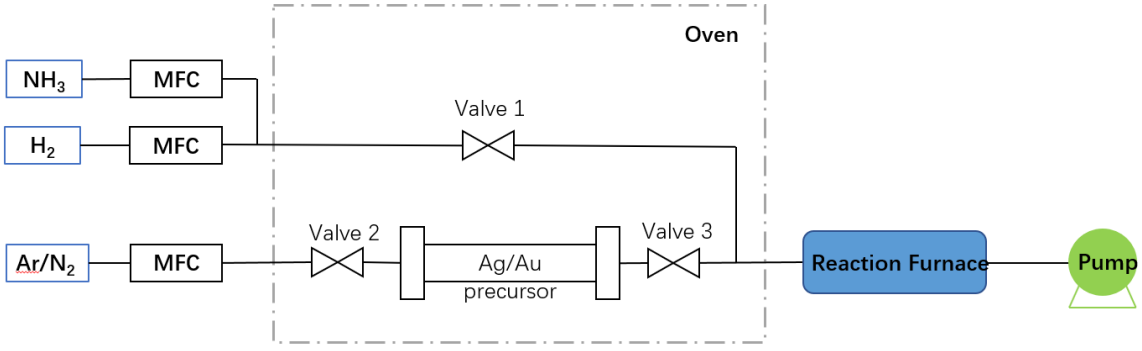

Figure 5.10. Schematics of home-made CVD reactor

Figure 5.11a and 5.11b demonstrate the cross-sectional and top view image of Au and Ag took by Scanning Electron Microscopy (SEM). Small crystalline grains were observed in both Au and Ag films. Film thickness and growth rate was measured and calculated through cross-sectional images.

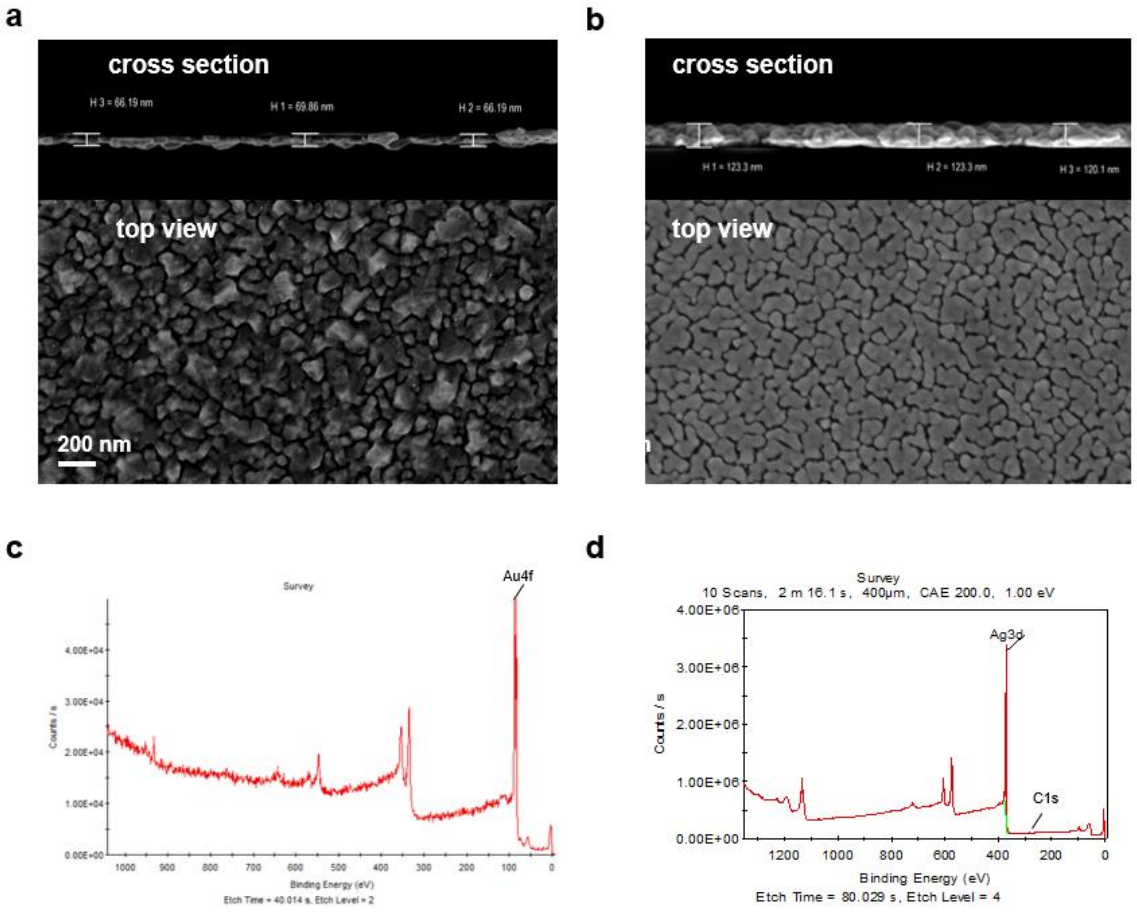

Figure 5.11. a) SEM image of gold film. **b)** SEM image of silver film. **c)** XPS analysis of

gold film showed no detectable carbon content. **d**) XPS analysis of silver film showed small amount of carbon content

X-ray photoelectron spectroscopy (XPS) was then used to determine the elemental composition and the purity of the film. Survey scan of both Au and Ag films with best purity achieved are shown in Figure 5.11c and 5.11d. The carbon content was below detection limit for Au film while 6.61 percent of C was observed in Ag film. No oxygen peak can be detected in both Au and Ag film XPS fine scans. High purity silver and gold films were achieved under our deposition condition development.

Photos of CVD gold and silver were shown in Figure 5.12a. They both displayed metallic reflection. A positive linear relation between growth rate and the precursor temperature for both Au and Ag film was observed (Figure 5.12b). The higher growth rate was resulted from an increased vapor pressure induced by the higher precursor temperature. This data is consistent with TGA data that gold precursor sublimed at a higher temperature and had a higher enthalpy of sublimation. Control experiments were also conducted. No gold film was obtained without hydrogen gas co-reactant. Some silver films were obtained probably due to thermal decomposition of silver at 230 °C. However, this silver film had ~ 40% carbon content by XPS and was not conductive.

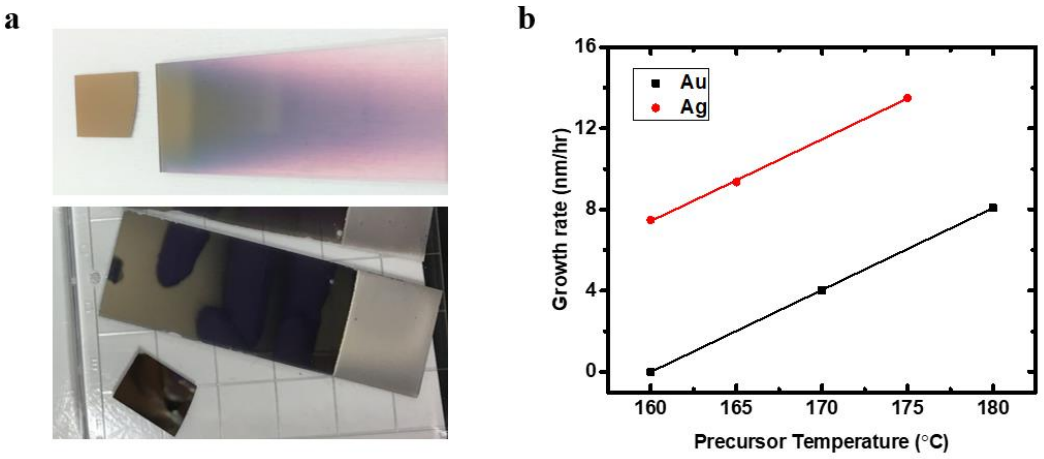

Figure 5.12. a) Photos of deposited gold film (top) and silver film (bottom). **b)** growth rate increases linearly with precursor temperature

In terms of electrical property, resistivity was measured for both Au and Ag films by 4-point probe and hall measurement system. In the case of Au films, relative constant resistivity was obtained as 245, 221.94, 250.745 Ω·nm under different deposition conditions, which is only one order magnitude higher than that if bulk Au (Ω·nm). While for Ag films, resistivity ranging from 192.5 Ω·nm to 15000 Ω·nm was acquired due to different carbon impurity level under various condition. The purest Ag film give least resistivity as 192.5 Ω·nm, showing only one order magnitude higher than bulk Ag (15.9 Ω·nm).

5.7 Conclusion

In summary, volatile homoleptic, dimeric Au(I) amidinates and tetrameric Ag(I) were synthesized in one step through a salt metathesis reaction between metal(I) source and

amidines without any involvement of potential trace metal contaminants. Tetrameric organometallic silver complex was reported and was hypothesized to undergo dissociation to dimeric form upon heating. Both compounds showed remarkable thermal and air stability, yet excellent reactivity with hydrogen. CVD of metallic gold and silver films were obtained via benign hydrogen reduction at low temperatures. The film obtained were high quality with high conductivity and low carbon content. Bicyclic amidinate ligands provide the opportunity for synthesis of other stable and reactive CVD or ALD metal precursors.

5.8 Synthesis experimental

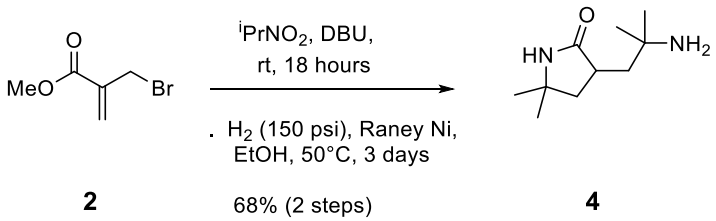

3-(2-amino-2-methylpropyl)-5,5-dimethylpyrrolidin-2-one 4. DBU (36 mL, 240.48 mmol) was dissolved in 500 mL of 2-nitropropane, followed by addition of methyl 2-(bromomethyl)acrylate **2** (20.5 g, 114.5 mmol). This was stirred at room temperature for 18 hours, then concentrated under reduced pressure at 70°C to give a large quantity of brown oil. This oil was taken up in 300 mL of Et_2O and washed with 3.0 M HCl (3 × 200 mL), brine (2 × 100 mL), then dried using anhydrous $MgSO_4$. Filtration and subsequent evaporation gave a blue-green oil that slowly solidified to pale-yellow plates.

This was dissolved in 1 L of EtOH, to which 20 g of anhydrous $MgSO_4$ was added,

followed by 20 g of Raney®-Nickel (Raney® 4200, slurry in water). The suspension was placed in a Parr hydrogenator and pressurized with H_2 to 150 psi, then mechanically stirred for 3 days at 50°C. After release of H_2, the suspension was filtered through a Celite pad and volatiles removed in vacuo to give a large amount of crude **4** as a pale brown solid. This was dissolved in 200 mL of 3.0 M HCl and washed with CH_2Cl_2 (3 × 100 mL), then basified with 150 mL of 10.0 M NaOH, causing **4** to precipitate out of solution. The suspension was then extracted with CH_2Cl_2 (5 × 100 mL), and the extracts combined, dried using anhydrous $MgSO_4$, filtered and evaporated to provide pure **4** (14.3 g, 68% over 2 steps) as a white solid, mp. 125-127°C. **^{1}H NMR** (500 MHz, $CDCl_3$) δ 5.92-5.70 (bs, 1H), 2.71-2.64 (m, 1H), 2.30-2.23 (m, 1H), 2.16-2.09 (m, 1H), 2.00-1.75 (bs, 2H), 1.67-1.60 (m, 1H), 1.36-1.29 (m, 1H), 1.28 (s, 3H), 1.24 (s, 3H), 1.15 (s, 3H), 1.12 (s, 3H); **^{13}C NMR** (125 MHz, $CDCl_3$) δ 178.9, 54.6, 49.9, 46.4, 45.4, 38.4, 31.6, 30.6, 30.3, 29.0; **HRMS** (ESI): m/z calcd. for $C_{10}H_{21}N_2O$ ($M+H^+$) 185.1648, found 185.1651.

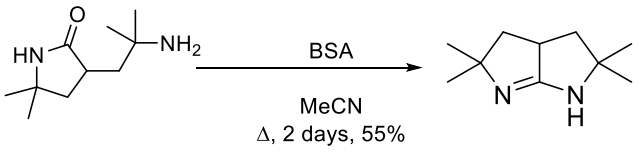

4 **1**

2,2,5,5-tetramethyl-1,2,3,3a,4,5-hexahydropyrrolo[2,3-b]pyrrole 1. **4** (15 g, 81.4 mmol) was suspended in 200 mL of MeCN. Upon addition of *N*,*O*-bis(trimethylsilyl)acetamide, (BSA, 33.5 g, 160.0 mmol) over 3 hours, all solids quickly dissolved. The solution was refluxed for 2 days, during which the progress of the reaction was monitored by NMR. (Note: if the reaction does not go to completion, more BSA can

be added slowly to the reaction mixture as required.) Once the reaction was complete, the reaction mixture was concentrated under reduced pressure. The remaining oil was dissolved in 200 mL of 3.0 M HCl and washed with CH_2Cl_2 (3 × 100 mL), then ice was added, and the solution basified with 125 mL of 10.0 M NaOH, causing **1** to precipitate out of solution. The suspension was then extracted with CH_2Cl_2 (4 × 100 mL), and the extracts combined, dried using anhydrous $MgSO_4$, filtered and evaporated to provide crude **1** as a pale-yellow waxy solid. Oily impurities were collected by sublimation at 45 °C at 50 mTorr for 2 hours and discarded. Further sublimation of the remaining solid overnight at 70 °C at 50mTorr gave pure, anhydrous **1** (7.4 g, 55%) as a white solid suitable for the synthesis of metal-containing ALD precursors, mp. 182-183 °C. **^{1}H NMR** (500 MHz, C_6D_6) δ 9.20-8.45 (bs, 1H), 3.22-3.14 (m, 1H), 1.73-1.66 (m, 2H), 1.33 (s, 6H), 1.29-1.23 (m, 2H), 1.17 (s, 6H); **^{13}C NMR** (125 MHz, C_6D_6) δ 174.9, 69.8, 46.2, 45.3, 31.5, 29.1; **HRMS** (ESI): m/z calcd. for $C_{10}H_{19}N_2$ ($M+H^+$) 167.1543, found 167.1547.

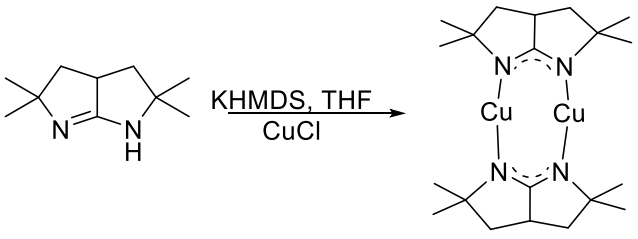

Copper (I) 2,2,5,5-tetramethyl-1,2,3,3a,4,5-hexahydropyrrolo[2,3-b]pyrrolide 5.

(100.0 mg, 0.601 mmol) was suspended in 5mL of anhydrous THF. Potassium bis(trimethylsilyl)amide (126.3 mg, 0.633 mmol) was added, at which all solids quickly dissolved. After stirring for 1 hour, copper (I) chloride (65.5 mg, 0.662 mmol) was added as a solid and the reaction allowed to continue overnight. The reaction was filtered through a Celite pad and evaporated to give an off-white solid that was thoroughly stirred with 80 mL of pentane and filtered again through Celite. Evaporation of the filtrate yielded a mixture of diastereomers of **5** (75.7 mg, 55%) as a slightly off-white solid that was recrystallized from anhydrous pentane at −30 °C to give white orthorhombic crystals suitable for single-crystal X-ray diffraction, mp. 306-307°C (sealed capillary). The recrystallized material may be further purified by vacuum sublimation if so desired (150 °C, 40 mTorr). **Elemental Analysis** calcd. for $C_{20}H_{34}Cu_2N_4$: C 52.49%, H 7.49%, N 12.24%; found C 52.18%, H 7.42%, N 12.60%; **^{1}H NMR** (500 MHz, C_6D_6) δ 3.27-3.17 (m, 1H), 1.75-1.68 (m, 2H), 1.35-1.26 (m, 2H), 1.28 (s, 3H), 1.27 (s, 3H), 1.11 (s, 3H), 1.10 (s, 3H); **^{13}C NMR** (125 MHz, C_6D_6) δ 187.5, 187.2, 70.43, 70.42, 47.3, 47.2, 45.4, 45.2, 33.30, 33.25, 29.1, 28.9.

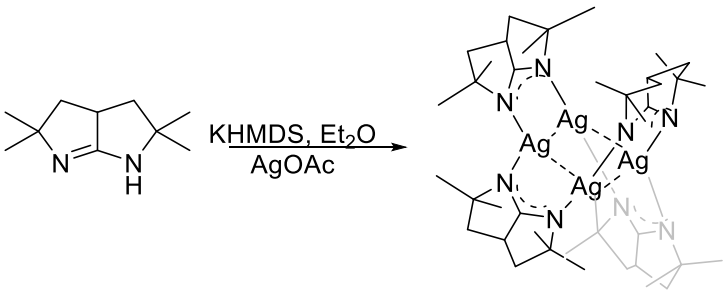

Silver (I) tetramer 6. (100.0 mg, 0.601 mmol) was suspended in 50 mL of anhydrous Et_2O. Potassium bis(trimethylsilyl)amide (126.3 mg, 0.633 mmol) was added, at which all

solids quickly dissolved. After stirring for 1 hour, silver (I) acetate (100.3 mg, 0.662 mmol) was added as a solid and the reaction allowed to continue overnight. The reaction was filtered through a Celite pad and evaporated to give an off-white solid that was thoroughly stirred with 500 mL of pentane and filtered again through Celite. Evaporation of the filtrate yielded crude **6** (147.7 mg, 45 %) as a slightly off-white solid that was recrystallized from hot dichloromethane to give white crystals suitable for single-crystal X-ray diffraction. The recrystallized material may be further purified by vacuum sublimation if so desired (170 °C, 30 mTorr). **Elemental Analysis** calcd. for $C_{40}H_{68}Ag_4N_8$: C 43.98 %, H 6.27 %, N 10.26 %; found C 44.38%, H 6.22%, N 9.95%

Gold (I) 2,2,5,5-tetramethyl-1,2,3,3a,4,5-hexahydropyrrolo[2,3-b]pyrrolide 7. (100.0 mg, 0.601 mmol) was suspended in 100 mL of anhydrous THF. Potassium bis(trimethylsilyl)amide (126.3 mg, 0.633 mmol) was added, at which all solids quickly dissolved. After stirring for 1 hour, Chloro(dimethylsulfide)gold(I) (195.0 mg, 0.662 mmol) was added as a solid and the reaction allowed to continue overnight. The reaction was filtered through a Celite pad and evaporated to give an white solid that was gently washed rapidly with 10 mL of cold 1:1 THF:pentane to afford a mixture of diastereomers of **7** (261.2 mg, 60 %) as a slightly off-white solid that was recrystallized from hot dichloromethane to give white crystals suitable for single-crystal X-ray diffraction. The recrystallized material may be further purified by vacuum sublimation if so desired (180 °C, 30 mTorr). **Elemental Analysis** calcd. for $C_{20}H_{34}Au_2N_4$: C 33.16%, H 4.73 %, N 7.73 %;

found C 33.12%, H 4.56 %, N 7.68%; **^{1}H NMR** (500 MHz, C_6D_6) δ 3.15-3.08 (m, 1H), 1.56-1.53 (m, 2H), 1.35-1.26 (m, 2H), 1.24-1.23 (d, 3H), 1.23-1.19 (m, 2H),1.04-1.02 (d, 3H)

References

1. U.S. Energy Information Administration. *Monthly Energy Review* **April 2016.** URL: www.eia.gov/totalenergy/data/monthly/archive/00351604.pdf Accessed May 1, 2018.

2. International Energy Agency. *Renewables 2017* **2017.** URL: www.iea.org/publications/renewables2017 Accessed May 1, 2018.

3. U.S. Department of Energy. *Grid Energy Storage* **2013**. URL: www.energy.gov/oe/downloads/grid-energy-storage-december-2013 Accessed May 1, 2018.

4. Rugolo, J.; Aziz, M. J., Electricity storage for intermittent renewable sources. *Energy & Environmental Science* **2012,** *5* (5), 7151-7160.

5. How to lose half a trillion euros. *The Economist* **2013**. URL: https://www.economist.com/news/briefing/21587782-europes-electricity-providers-face-existential-threat-how-lose-half-trillion-euros Accessed May 1, 2018.

6. Parsons, B.; Milligan, M.; Zavadil, B.; Brooks, D.; Kirby, B.; Dragoon, K.; Caldwell, J., Grid impacts of wind power: a summary of recent studies in the United States. *Wind Energy* **2004,** *7* (2), 87-108.

7. Dunn, B.; Kamath, H.; Tarascon, J.-M., Electrical Energy Storage for the Grid: A Battery of Choices. *Science* **2011,** *334* (6058), 928-935.

8. Market Driven Distributed Energy Storage Requirements for Load Management Applications. *EPRI Report 1014668* **2007**.

9. Moore, M.; Counce, R.; Watson, J.; Zawodzinski, T., A Comparison of the Capital Costs of a Vanadium Redox-Flow Battery and a Regenerative Hydrogen-Vanadium Fuel Cell. *Journal of Advanced Chemical Engineering* **2015,** *5* (4).

10. U.S. Geological Survey-Vanadium. *Mineral Commodity Summaries* **2014**. URL: minerals.usgs.gov/minerals/pubs/commodity/vanadium/mcs-2014-vanad.pdf Accessed May 1, 2018.

11. Lin, K.; Chen, Q.; Gerhardt, M. R.; Tong, L.; Kim, S. B.; Eisenach, L.; Valle, A.

W.; Hardee, D.; Gordon, R. G.; Aziz, M. J.; Marshak, M. P., Alkaline quinone flow battery. *Science* **2015,** *349* (6255), 1529-32.

12. Huskinson, B.; Marshak, M. P.; Suh, C.; Er, S.; Gerhardt, M. R.; Galvin, C. J.; Chen, X.; Aspuru-Guzik, A.; Gordon, R. G.; Aziz, M. J., A metal-free organic–inorganic aqueous flow battery. *Nature* **2014,** *505*, 195.

13. Janoschka, T.; Martin, N.; Hager, M. D.; Schubert, U. S., An Aqueous Redox-Flow Battery with High Capacity and Power: The TEMPTMA/MV System. *Angew Chem Int Ed Engl* **2016,** *55* (46), 14427-14430.

14. Liu, T.; Wei, X.; Nie, Z.; Sprenkle, V.; Wang, W., A Total Organic Aqueous Redox Flow Battery Employing a Low Cost and Sustainable Methyl Viologen Anolyte and 4-HO-TEMPO Catholyte. *Advanced Energy Materials* **2016,** *6* (3), 1501449-n/a.

15. Beh, E. S.; De Porcellinis, D.; Gracia, R. L.; Xia, K. T.; Gordon, R. G.; Aziz, M. J., A Neutral pH Aqueous Organic–Organometallic Redox Flow Battery with Extremely High Capacity Retention. *ACS Energy Letters* **2017,** *2* (3), 639-644.

16. Lin, K.; Gómez-Bombarelli, R.; Beh, E. S.; Tong, L.; Chen, Q.; Valle, A.; Aspuru-Guzik, A.; Aziz, M. J.; Gordon, R. G., A redox-flow battery with an alloxazine-based organic electrolyte. **2016,** *1*, 16102.

17. Orita, A.; Verde, M. G.; Sakai, M.; Meng, Y. S., A biomimetic redox flow battery based on flavin mononucleotide. *Nat Commun* **2016,** *7*, 13230.

18. Winsberg, J.; Stolze, C.; Muench, S.; Liedl, F.; Hager, M. D.; Schubert, U. S., TEMPO/Phenazine Combi-Molecule: A Redox-Active Material for Symmetric Aqueous Redox-Flow Batteries. *ACS Energy Letters* **2016,** *1* (5), 976-980.

19. Yang, Z.; Tong, L.; Tabor, D. P.; Beh, E. S.; Goulet, M.-A.; De Porcellinis, D.; Aspuru-Guzik, A.; Gordon, R. G.; Aziz, M. J., Alkaline Benzoquinone Aqueous Flow Battery for Large-Scale Storage of Electrical Energy. *Advanced Energy Materials* **2017**, 1702056-n/a.

20. Gerhardt, M. R.; Tong, L.; Gómez-Bombarelli, R.; Chen, Q.; Marshak, M. P.; Galvin, C. J.; Aspuru-Guzik, A.; Gordon, R. G.; Aziz, M. J., Anthraquinone Derivatives in Aqueous Flow Batteries. *Advanced Energy Materials* **2017,** *7* (8), 1601488-n/a.

21. Tikhonov, A. N., The cytochrome b6f complex at the crossroad of photosynthetic electron transport pathways. *Plant Physiology and Biochemistry* **2014,** *81*, 163-183.

22. Quan, M.; Sanchez, D.; Wasylkiw, M. F.; Smith, D. K., Voltammetry of Quinones in Unbuffered Aqueous Solution: Reassessing the Roles of Proton Transfer and

Hydrogen Bonding in the Aqueous Electrochemistry of Quinones. *Journal of the American Chemical Society* **2007,** *129* (42), 12847-12856.

23. Yang, B.; Hoober-Burkhardt, L.; Krishnamoorthy, S.; Murali, A.; Prakash, G. K. S.; Narayanan, S. R., High-Performance Aqueous Organic Flow Battery with Quinone-Based Redox Couples at Both Electrodes. *Journal of The Electrochemical Society* **2016,** *163* (7), A1442-A1449.

24. Er, S.; Suh, C.; Marshak, M. P.; Aspuru-Guzik, A., Computational design of molecules for an all-quinone redox flow battery. *Chemical Science* **2015,** *6* (2), 885-893.

25. Tong, L.; Chen, Q.; Wong, A. A.; Gomez-Bombarelli, R.; Aspuru-Guzik, A.; Gordon, R. G.; Aziz, M. J., UV-Vis spectrophotometry of quinone flow battery electrolyte for in situ monitoring and improved electrochemical modeling of potential and quinhydrone formation. *Physical Chemistry Chemical Physics* **2017,** *19* (47), 31684-31691.

26. Foyer, C. H.; Noctor, G., Redox Regulation in Photosynthetic Organisms: Signaling, Acclimation, and Practical Implications. *Antioxidants & Redox Signaling* **2008,** *11* (4), 861-905.

27. Costentin, C., Electrochemical Approach to the Mechanistic Study of Proton-Coupled Electron Transfer. *Chemical Reviews* **2008,** *108* (7), 2145-2179.

28. Liang, Y.; Jing, Y.; Gheytani, S.; Lee, K.-Y.; Liu, P.; Facchetti, A.; Yao, Y., Universal quinone electrodes for long cycle life aqueous rechargeable batteries. *Nature Materials* **2017,** *16*, 841.

29. Yao, M.; Ando, H.; Kiyobayashi, T., Dialkoxybenzoquinone-type Active Materials for Rechargeable Lithium Batteries: The Effect of the Alkoxy Group Length on the Cycle-stability. *Energy Procedia* **2013,** *34*, 880-887.

30. Huskinson, B.; Rugolo, J.; Mondal, S. K.; Aziz, M. J., A high power density, high efficiency hydrogen-chlorine regenerative fuel cell with a low precious metal content catalyst. *Energy & Environmental Science* **2012,** *5* (9), 8690-8698.

31. Tan, L.; Chen, H.; Pan, D.; Pan, N., Investigation into the gelation and crystallization of polyacrylonitrile. *European Polymer Journal* **2009,** *45* (5), 1617-1624.

32. Ding, Y.; Li, Y.; Yu, G., Exploring Bio-inspired Quinone-Based Organic Redox Flow Batteries: A Combined Experimental and Computational Study. *Chem 1* (5), 790-801.

33. González Moa, M. J.; Mandado, M.; Mosquera, R. A., A Computational Study on the Stacking Interaction in Quinhydrone. *The Journal of Physical Chemistry A* **2007,** *111* (10), 1998-2001.

34. Barone, V.; Cacelli, I.; Crescenzi, O.; d'Ischia, M.; Ferretti, A.; Prampolini, G.; Villani, G., Unraveling the interplay of different contributions to the stability of the quinhydrone dimer. *RSC Advances* **2014,** *4* (2), 876-885.

35. Carney, T. J.; Collins, S. J.; Moore, J. S.; Brushett, F. R., Concentration-Dependent Dimerization of Anthraquinone Disulfonic Acid and Its Impact on Charge Storage. *Chemistry of Materials* **2017,** *29* (11), 4801-4810.

36. Biilmann, E., Studies on the Quinhydrone Electrode. *Ann. Chim.* **1921,** *16*, 321-340.

37. Wong, A. A.; Aziz, M. J.; Rubinstein, S., Direct Visualization of Electrochemical Reactions and Comparison of Commercial Carbon Papers in operando by Fluorescence Microscopy Using a Quinone-Based Flow Cell. *ECS Transactions* **2017,** *77* (11), 153-161.

38. Liu, Z.; Wainright, J. S.; Huang, W.; Savinell, R. F., Positioning the reference electrode in proton exchange membrane fuel cells: calculations of primary and secondary current distribution. *Electrochimica Acta* **2004,** *49* (6), 923-935.

39. Chen, Q.; Gerhardt, M. R.; Aziz, M. J., Dissection of the Voltage Losses of an Acidic Quinone Redox Flow Battery. *Journal of The Electrochemical Society* **2017,** *164* (6), A1126-A1132.

40. Beck, F.; Heydecke, G., On the Mechanism of the Cathodic Reduction of Anthraquinone to Anthrone. *Berichte der Bunsengesellschaft für physikalische Chemie* **1987,** *91* (1), 37-43.

41. Comninellis, C.; Plattner, E., The electrochemical reduction of anthraquinone to anthrone in concentrated H2SO4. *Journal of Applied Electrochemistry* **1985,** *15* (5), 771-773.

42. Shyamasundar, N.; Caluwe, P., Lithium aluminum hydride reduction of peri-alkoxy-9,10-anthraquinones. *The Journal of Organic Chemistry* **1981,** *46* (8), 1552-1557.

43. Huskinson, B.; Marshak, M. P.; Suh, C.; Er, S.; Gerhardt, M. R.; Galvin, C. J.; Chen, X.; Aspuru-Guzik, A.; Gordon, R. G.; Aziz, M. J., A metal-free organic-inorganic aqueous flow battery. *Nature* **2014,** *505* (7482), 195-8.

44. Hu, B.; Debruler, C.; Rhodes, Z.; Liu, T., A Long Cycling Aqueous Organic Redox Flow Battery (AORFB) towards Sustainable and Safe Energy Storage. *J. Am. Chem. Soc.* **2016,** *139* (3), 1207-1214.

45. Lin, K.; Gómez-Bombarelli, R.; Beh, E. S.; Tong, L.; Chen, Q.; Valle, A.; Aspuru-Guzik, A.; Aziz, M. J.; Gordon, R. G., A redox-flow battery with an alloxazine-based organic electrolyte. *Nature Energy* **2016,** *1*, 16102.

46. Yang, B.; Hoober-Burkhardt, L.; Wang, F.; Prakash, G. S.; Narayanan, S., An inexpensive aqueous flow battery for large-scale electrical energy storage based on water-soluble organic redox couples. *J. Electrochem. Soc.* **2014,** *161* (9), A1371-A1380.

47. Yang, B.; Hoober-Burkhardt, L.; Krishnamoorthy, S.; Murali, A.; Prakash, G. S.; Narayanan, S., High-Performance Aqueous Organic Flow Battery with Quinone-Based Redox Couples at Both Electrodes. *J. Electrochem. Soc.* **2016,** *163* (7), A1442-A1449.

48. Hoober-Burkhardt, L.; Krishnamoorthy, S.; Yang, B.; Murali, A.; Nirmalchandar, A.; Prakash, G. K. S.; Narayanan, S. R., A New Michael-Reaction-Resistant Benzoquinone for Aqueous Organic Redox Flow Batteries. *J. Electrochem. Soc.* **2017,** *164* (4), A600-A607.

49. Hosoya, T.; French, A.; Rosenau, T., Chemistry of 2,5-dihydroxy-[1,4]-benzoquinone, a Key Chromophore in Aged Cellulosics. *Mini-Rev. Org. Chem.* **2013,** *10* (3), 309-315.

50. Janoschka, T.; Martin, N.; Martin, U.; Friebe, C.; Morgenstern, S.; Hiller, H.; Hager, M. D.; Schubert, U. S., An aqueous, polymer-based redox-flow battery using non-corrosive, safe, and low-cost materials. *Nature* **2015,** *527* (7576), 78-81.

51. Yamamura, T.; Watanabe, N.; Yano, T.; Shiokawa, Y., Electron-Transfer Kinetics of Np[sup 3+]/Np[sup 4+], NpO[sub 2][sup +]/NpO[sub 2][sup 2+], V[sup 2+]/V[sup 3+], and VO[sup 2+]/VO[sub 2][sup +] at Carbon Electrodes. *J. Electrochem. Soc.* **2005,** *152* (4), A830.

52. Sum, E.; Skyllas-Kazacos, M., A study of the V(II)/V(III) redox couple for redox flow cell applications. *J. Power Sources* **1985,** *15* (2-3), 179-190.

53. Sum, E.; Rychcik, M.; Skyllas-kazacos, M., Investigation of the V(V)/V(IV) system for use in the positive half-cell of a redox battery. *J. Power Sources* **1985,** *16* (2), 85-95.

54. Misiolek, A. W.; Ichimura, A. S.; Gentner, R. A.; Huang, R. H.; McCaffrey, V. P.; Jackson, J. E., Building Blocks for Molecule-Based Magnets: Radical Anions and

Dianions of Substituted 3,6-Dimethylenecyclohexane-1,2,4,5-tetrones as Paramagnetic Bridging Ligands. *Inorg. Chem.* **2009,** *48* (18), 9005-9017.

55. Gan, X.; Jiang, W.; Wang, W.; Hu, L., An Approach to 3,6-Disubstituted 2,5-Dioxybenzoquinones via Two Sequential Suzuki Couplings. Three-Step Synthesis of Leucomelone. *Organic Letters* **2009,** *11* (3), 589-592.

56. Nakao, H.; Arakawa, M.; Nakamura, T.; Fukushima, M., Antileukemic Agents. II. New 2, 5-Bis (1-aziridinyl)-p-benzoquinone Derivatives. *CHEMICAL & PHARMACEUTICAL BULLETIN* **1972,** *20* (9), 1968-1979.

57. Kusai, A.; Tanaka, S.; Ueda, S., The Stability of Carboquone in Aqueous Solution. II. Kinetics and Mechanisms of Degradation of 2, 5-Bis (1-aziridinyl)-3, 6-dimethyl-1, 4-benzoquinone and 2, 5-Bis-(1-aziridinyl)-3, 6-diisopropyl-1, 4-benzoquinone in Aqueous Solution. *CHEMICAL & PHARMACEUTICAL BULLETIN* **1982,** *30* (7), 2534-2543.

58. Barrès, A.-L.; Geng , J.; Bonnard, G.; Renault , S.; Gottis , S.; Mentré, O.; Frayret, C.; Dolhem, F.; Poizot, P., High-Potential Reversible Li Deintercalation in a Substituted Tetrahydroxy-p-benzoquinone Dilithium Salt: An Experimental and Theoretical Study. *Chemistry – A European Journal* **2012,** *18* (28), 8800-8812.

59. Le Gall, T.; Reiman, K. H.; Grossel, M. C.; Owen, J. R., Poly(2,5-dihydroxy-1,4-benzoquinone-3,6-methylene): a new organic polymer as positive electrode material for rechargeable lithium batteries. *J. Power Sources* **2003,** *119-121*, 316-320.

60. Sadykh-Zade, S. I.; Ragimov, A. V.; Suleimanova, S. S.; Liogon'kii, V. I., The polymerization of quinones in an alkaline medium and the structure of the resulting polymers. *Polymer Science U.S.S.R.* **1972,** *14* (6), 1395-1403.

61. Song, Z.; Qian, Y.; Liu, X.; Zhang, T.; Zhu, Y.; Yu, H.; Otani, M.; Zhou, H., A quinone-based oligomeric lithium salt for superior Li-organic batteries. *Energy & Environmental Science* **2014,** *7* (12), 4077-4086.

62. Liu, K.; Zheng, J.; Zhong, G.; Yang, Y., Poly(2,5-dihydroxy-1,4-benzoquinonyl sulfide) (PDBS) as a cathode material for lithium ion batteries. *Journal of Materials Chemistry* **2011,** *21* (12), 4125-4131.

63. Mark, M.; Robert, C.; Jack, W.; Thomas, Z., A Comparison of the Capital Costs of a Vanadium Redox-Flow Battery and. **2015,** *5* (4).

64. Winsberg, J.; Stolze, C.; Schwenke, A.; Muench, S.; Hager, M. D.; Schubert, U. S., Aqueous 2,2,6,6-Tetramethylpiperidine-N-oxyl Catholytes for a High-Capacity and

High Current Density Oxygen-Insensitive Hybrid-Flow Battery. *ACS Energy Letters* **2017,** *2* (2), 411-416.

65. Wu, Y.; Zeng, R.; Nan, J.; Shu, D.; Qiu, Y.; Chou, S.-L., Quinone Electrode Materials for Rechargeable Lithium/Sodium Ion Batteries. *Advanced Energy Materials* **2017,** *7* (24), 1700278-n/a.

66. J. Bingham, S.; H. P. Tyman, J., The synthesis of kermesic acid and isokermesic acid derivatives and of related dihydroxyanthraquinones. *Journal of the Chemical Society, Perkin Transactions 1* **1997,** (24), 3637-3642.

67. Yamamoto, N.; Kubozono, T.; Kinoshita, Y., Mechanism for Oxidative Decomposition of Anthraquinone Dye with Hydrogen Peroxide. *Journal of Oleo Science* **2001,** *50* (6), 507-513.

68. Beh, E. S.; Tong, L.; Gordon, R. G., Synthesis of 5,5-Bicyclic Amidines as Ligands for Thermally Stable Vapor Deposition Precursors. *Organometallics* **2017,** *36* (8), 1453-1456.

69. Fischer, R. A., *Precursor Chemistry of Advanced Materials: CVD, ALD and Nanoparticles*. Springer-Verlag Berlin: Heidelberg, 1976; Vol. 9.

70. Jones, A. C.; Hitchman, M. L., *Chemical Vapour Deposition: Precursors, Processes and Applications* RSC Publishing: Cambridge, 2009.

71. George, S. M., Atomic Layer Deposition: An Overview. *Chem. Rev.* **2010,** *110* (1), 111-131.

72. Gordon, R. G., ALD Precursors and Reaction Mechanisms. In *Atomic Layer Deposition for Semiconductors*, Hwang, C. S.; Yoo, C. Y., Eds. Springer US: New York, 2014; pp 15-46.

73. Johnson, R. W.; Hultqvist, A.; Bent, S. F., A brief review of atomic layer deposition: from fundamentals to applications. *Mater. Today* **2014,** *17* (5), 236-246.

74. Putkonen, M.; Niinistö, L., Organometallic Precursors for Atomic Layer Deposition. In *Precursor Chemistry of Advanced Materials*, Fischer, R. A., Ed. Springer Berlin Heidelberg: Berlin, Heidelberg, 2005; pp 125-145.

75. Oren, M.; Choudhury, A. N. M. M., Interconnect Metallization Technique for GaAs Digital IC's. *Journal of The Electrochemical Society* **1987,** *134* (3), 750-752.

76. Baum, T. H.; Comita, P. B., Laser-induced chemical vapor deposition of metals for microelectronics technology. *Thin Solid Films* **1992,** *218* (1), 80-94.

77. Ekin, J. W.; Larson, T. M.; Bergren, N. F.; Nelson, A. J.; Swartzlander, A. B.; Kazmerski, L. L.; Panson, A. J.; Blankenship, B. A., High Tc superconductor/noble-metal contacts with surface resistivities in the 10−10 Ω cm2 range. *Applied Physics Letters* **1988,** *52* (21), 1819-1821.

78. Wenzel, T. J.; Williams, E. J.; Haltiwanger, R. C.; Sievers, R. E., Studies of metal chelates with the novel ligand 2,2,7-trimethyl-3,5-octanedione. *Polyhedron* **1985,** *4* (3), 369-378.

79. Maårtensson, P.; Carlsson, J. O., Atomic Layer Epitaxy of Copper: Growth and Selectivity in the Cu(II)-2,2,6,6-tetramethyl-3,5-heptanedionate/ Process. *Journal of The Electrochemical Society* **1998,** *145* (8), 2926-2931.

80. Park, K.-H.; Marshall, W. J., Remarkably Volatile Copper(II) Complexes of N,N‘-Unsymmetrically Substituted 1,3-Diketimines as Precursors for Cu Metal Deposition via CVD or ALD. *Journal of the American Chemical Society* **2005,** *127* (26), 9330-9331.

81. Li, Z.; Barry, S. T.; Gordon, R. G., Synthesis and Characterization of Copper(I) Amidinates as Precursors for Atomic Layer Deposition (ALD) of Copper Metal. *Inorganic Chemistry* **2005,** *44* (6), 1728-1735.

82. Lim, B. S.; Rahtu, A.; Park, J.-S.; Gordon, R. G., Synthesis and Characterization of Volatile, Thermally Stable, Reactive Transition Metal Amidinates. *Inorganic Chemistry* **2003,** *42* (24), 7951-7958.

83. Coyle, J. P.; Monillas, W. H.; Yap, G. P. A.; Barry, S. T., Synthesis and Thermal Chemistry of Copper (I) Guanidinates. *Inorganic Chemistry* **2008,** *47* (2), 683-689.

84. Park, J. W.; Jang, H. S.; Kim, M.; Sung, K.; Lee, S. S.; Chung, T.-M.; Koo, S.; Kim, C. G.; Kim, Y., Synthesis of Cu(II) aminoalkoxide complexes and their unusual thermolysis to Cu(0). *Inorganic Chemistry Communications* **2004,** *7* (4), 463-466.

85. Grushin, V. V.; Marshall, W. J., Water as an Ideal Solvent for the Synthesis of Easily Hydrolyzable Compounds: High-Yield Preparation of 2-Pyrrolecarbaldimines and their CVD/ALD-Relevant Cu(II) Derivatives in H2O. *Advanced Synthesis & Catalysis* **2004,** *346* (12), 1457-1460.

86. Lim, B. S.; Rahtu, A.; Gordon, R. G., Atomic layer deposition of transition metals. *Nat Mater* **2003,** *2* (11), 749-754.

87. de Rouffignac, P.; Park, J.-S.; Gordon, R. G., Atomic Layer Deposition of Y2O3 Thin Films from Yttrium Tris(N,N‘-diisopropylacetamidinate) and Water. *Chem. Mater.*

2005, *17* (19), 4808-4814.

88. Li, H.; Farmer, D. B.; Gordon, R. G.; Lin, Y.; Vlassak, J., Vapor Deposition of Ruthenium from an Amidinate Precursor. *J. Electrochem. Soc.* **2007,** *154* (12), D642.

89. Li, Z.; Lee, D. K.; Coulter, M.; Rodriguez, L. N.; Gordon, R. G., Synthesis and characterization of volatile liquid cobalt amidinates. *Dalton Trans* **2008,** (19), 2592-7.

90. Wu, J.; Li, J.; Zhou, C.; Lei, X.; Gaffney, T.; Norman, J. A. T.; Li, Z.; Gordon, R.; Cheng, H., Computational Study on the Relative Reactivities of Cobalt and Nickel Amidinates via β-H Migration. *Organometallics* **2007,** *26* (11), 2803-2805.

91. Li, J.; Wu, J.; Zhou, C.; Han, B.; Lei, X.; Gordon, R.; Cheng, H., On the relative stability of cobalt- and nickel-based amidinate complexes against β-migration. *International Journal of Quantum Chemistry* **2009,** *109* (4), 756-763.

92. Coyle, J. P.; Kurek, A.; Pallister, P. J.; Sirianni, E. R.; Yap, G. P. A.; Barry, S. T., Preventing thermolysis: precursor design for volatile copper compounds. *Chem. Commun.* **2012,** *48* (84), 10440-10442.

93. Löfås, S.; Ahlberg, P., Spiro- and bicyclic azalactams by hydrolysis of α-chlorinated bicyclic amidines. *J. Heterocycl. Chem.* **1984,** *21* (2), 583-586.

94. Wan, Z.-K.; Wacharasindhu, S.; Levins, C. G.; Lin, M.; Tabei, K.; Mansour, T. S., The Scope and Mechanism of Phosphonium-Mediated SNAr Reactions in Heterocyclic Amides and Ureas. *The Journal of Organic Chemistry* **2007,** *72* (26), 10194-10210.

95. Higashi, K.; Sato, M.; Furukawa, M., A Convenient Method for the Preparation of Cyclic Amidines Using Bis(trimethylsilyl)acetamide(Organic,Chemical). *Chemical & pharmaceutical bulletin* **1986,** *34* (12), 4927-4932.

96. Brandys, M.-C.; Jennings, M. C.; Puddephatt, R. J., Luminescent gold(I) macrocycles with diphosphine and 4,4[prime or minute]-bipyridyl ligands. *Journal of the Chemical Society, Dalton Transactions* **2000,** (24), 4601-4606.

97. Schmidbaur, H.; Raubenheimer, H. G.; Dobrzanska, L., The gold-hydrogen bond, Au-H, and the hydrogen bond to gold, Au[three dots, centered]H-X. *Chemical Society Reviews* **2014,** *43* (1), 345-380.

98. Coyle, J. P.; Gordon, P. G.; Wells, A. P.; Mandia, D. J.; Sirianni, E. R.; Yap, G. P. A.; Barry, S. T., Thermally Robust Gold and Silver Iminopyrrolidinates for Chemical Vapor Deposition of Metal Films. *Chemistry of Materials* **2013,** *25* (22), 4566-4573.

99. Hitchcock, P. B.; Lappert, M. F.; Pierssens, L. J. M., Synthesis and X-ray molecular structures of the silver(I) amides [{Ag[[small micro]-N(SiMe3)2]}4] and [{Ag[[small micro]-NCMe2(CH2)3CMe2]}4]. *Chemical Communications* **1996,** (10), 1189-1190.